

学位論文

Accurate muographic imaging of volcanoes by
background noise reduction with nuclear emulsions

(原子核乾板の背景ノイズ低減による火山
の高精度ミュオグラフィの実現)

平成 26 年 12 月博士(理学)申請

東京大学理学系研究科

地球惑星科学専攻

西山 竜一

Abstract

Muon radiography (muography) is a powerful technique for probing internal density profiles of volcanoes with higher spatial resolutions than other geophysical methods. For this purpose, several types of detectors have been used, such as scintillation detectors, gas chambers and nuclear emulsions. Particularly, the nuclear emulsion is suitable for imaging small and complex structures near the summit, because it has high angular resolutions (a few mrad), weighs light and does not require electricity for operation.

A requirement for muographic observation is to count precisely the number of signal muons which penetrate and emerge from the target mountain. One technical problem with nuclear emulsions, however, is an existence of background noise caused by non-signal particles. These noise particles mimic the muon signals, because the emulsion film is sensitive to all the charged particles passing through it. Although several prior works have tried to subtract the effect of the background noise with empirical models, it is still difficult to reduce the systematic uncertainty in density estimation. To reduce the uncertainty and improve accuracy of muography, it is necessary to understand the characteristics of the background particles and to develop emulsion detectors which can reduce them.

The candidates of the background noise particles are low-energy charged particles induced from secondary cosmic rays. To reduce these low-energy particles, this work proposes the use of the Emulsion Cloud Chamber (ECC).

ECC detector is a repeated structure of emulsion films and passive metal plates. This detector makes it possible to reject the low-energy particles, because they are deflected with larger angles in metal plates than penetrating muons. Thus, high-resolution microscopic analysis of the tracks enables us to distinguish signal tracks from noise tracks.

The performance of the background reduction is demonstrated by a test experiment with a prototype of ECC at Showa-Shinzan Lava Dome, Usu, Japan. The prototype is made of twenty OPERA films and nine 1-mm-thick lead plates. It was exposed to cosmic rays at the foot of the dome for 168 days. To analyze the tracks recorded in the detector, I have developed a method for track selection and efficiency estimation. As a result, the particle flux measured by ECC detector is lowered to be half to one-eighth of the flux measured by conventional emulsion detectors. Consequently, the density values derived from ECC detector are consistent with the typical bulk density of volcanic regions.

There are three pieces of evidence to support the validity of the use of ECC detector. First, the muographic results of ECC detector are consistent with the bulk density of Showa-Shinzan lava. Second, a three-dimensional density model estimated from the ECC results and gravity anomaly data agrees well with other geophysical observations in the shape of the lava. Lastly, my numerical simulation suggests that the energy threshold of ECC detector is feasible to reject background particles, consisting mainly of protons, muons and electrons produced by the hadronic interactions and elec-

trons from electromagnetic showers.

In conclusion, I have established a standard method for accurate muography with nuclear emulsions. To be concrete, I have specified the origin of background noise to the low-energy (< 1 GeV) charged particles. Thus, I have developed an analysis method to reduce these noise particles with ECC detector. Subsequently, I have demonstrated the performance of ECC detector by a test experiment at an actual geoscientific target. The method I have established will be useful for designing future muography detectors and inspecting other geoscientific targets.

Contents

§ 1 Introduction	8
§ 1.1 History of Muography Research	8
§ 1.2 Muography with Nuclear Emulsions	10
§ 1.3 Accuracy of Muography	12
§ 1.4 Candidates for Background Noise	14
§ 1.4.1 Environmental Radioactivity	14
§ 1.4.2 Electromagnetic Components	15
§ 1.4.3 Hadronic Components	16
§ 1.5 Emulsion Cloud Chamber	16
§ 1.6 Overview	18
§ 2 Background Reduction and Efficiency Correction	19
§ 2.1 Overview	19
§ 2.2 Experimental Setup	20
§ 2.3 Scanning and Reconstruction	26
§ 2.3.1 Development	26
§ 2.3.2 Scanning	27
§ 2.3.3 Reconstruction	28
§ 2.4 Track Selection	32
§ 2.4.1 χ^2 of deflection angles	32
§ 2.4.2 Grain density	35
§ 2.4.3 Number of Hits Selection	38

TABLE CONTENTS

§ 2.5 Efficiency Study	39
§ 2.5.1 Quartet Detector	39
§ 2.5.2 ECC Detector	41
§ 2.6 Results	44
§ 2.6.1 Particle Flux	44
§ 2.6.2 Results of Muography	47
§ 2.7 Summary	48
§ 3 Supporting Evidence	53
§ 3.1 Evidence 1: Comparison with Rock Sample	53
§ 3.2 Evidence 2: Comparison with Gravity Data	54
§ 3.3 Evidence 3: Comparison with Numerical Simulation	57
§ 3.4 Summary	61
§ 4 Discussion	62
§ 4.1 Background Noise	62
§ 4.2 Geoscientific Implications	65
§ 4.3 Future Prospects	67
§ 5 Conclusion	69
Appendices	
A Volcanological Backgrounds of Showa-Shinzan	71
B Principle of Muography	72
B.1 Energy Spectrum of Cosmic-ray Muons	72

TABLE CONTENTS

B.2	Muon Range in Rock	73
B.3	Integrated Muon Flux	75
B.4	Systematic Uncertainty in Density Estimation	76
B.4.1	Muon Energy Spectrum	76
B.4.2	Composition of Rock	79
B.4.3	Remaining Uncertainties	79
C	Joint Inversion of Muography and Gravity Data	81
C.1	Methods	81
C.1.1	Forward Modeling	82
C.1.2	Inverse Problem	83
C.2	Data Sets	86
C.2.1	Muography Data	86
C.2.2	Gravity Data	86
C.2.3	Topography Data	87
C.3	Target Region	90
C.4	Results	91
C.5	Resolution Study	92
D	Monte Carlo Simulation of Background Noise	100
D.1	Methods	100
D.2	COSMOS Simulation	100
D.2.1	Simulation Setup	101
D.2.2	Results	102

TABLE CONTENTS

D.3 GEANT4 Simulation	104
D.4 Results	105
Acknowledgements	107

§ 1 Introduction

This section provides readers with backgrounds of this thesis. Firstly, history of muography research is briefly introduced in § 1.1. In this work, nuclear emulsions are employed as a muography detector. The characteristics of nuclear emulsions are introduced in § 1.2. One big problem with current muography is poor accuracy of density estimation. This is because of the existence of background noise. This problem is discussed in § 1.3 and § 1.4. To overcome this problem, I propose the use of Emulsion Cloud Chamber in § 1.5. An overview of this thesis is given in § 1.6. To avoid redundant descriptions, the principle of muography is given in Appendix B.

§ 1.1 History of Muography Research

The history of the cosmic-ray muon radiography can date back to the experiment by Alvarez et al. (1970). Alvarez and his colleagues installed a spark chamber detector in a chamber inside the Second Pyramid of Giza, Egypt. They measured the flux of cosmic muons which penetrated the pyramid and detected "anomalies" of muon intensity caused by the four ridges of the pyramid. Although they could not find a hidden chamber inside the pyramid, this experiment demonstrated the feasibility of radiography based on measurement of muon absorption (muon absorption method). Subsequently, the use of this new method spread into various purposes, such as non-invasive inspection of the castles (Minato, 1986), blast furnaces (Nagamine et al., 2005),

volcanoes (Nagamine et al., 1995; Tanaka et al., 2007a,b, 2009; Lesparre et al., 2012; Cârloganu et al., 2013), seismic faults (Tanaka et al., 2011), caves (Barnaföldi et al., 2012) , and so on. In this thesis, the muon absorption method is called as "muography" to avoid confusion. As a reason for that, another radiographic method was recently invented, which utilizes scattering angles of cosmic muons (muon scattering method). This method requires two muon detectors enclosing the target to measure muon's deflection before and after passing through the target. Muons deflected with large angles can be used to infer the position of high Z material in the target. The scattering method is studied for nuclear safety (Borozdin et al., 2003) and non-destructive inspection of nuclear reactors, including Fukushima-Daiichi Nuclear Plant (Sugita et al., 2014; Morris et al., 2014).

The greatest advantage of the muography is its high spatial resolutions compared with other geophysical exploration methods, such as seismic surveys and gravity explorations. To be concrete, the resolutions of seismic surveys are limited to wave lengths of seismic waves, typically 1 km. Interpretation of gravity data has been suffering from non-uniqueness of solution. The spatial resolution of muography is ideally

$$\Delta x = L \times \Delta\theta, \tag{1}$$

where L is the distance of the muon detector and the target, and $\Delta\theta$ is the angular resolution of the detector. Considering typical configurations ($L \sim 1$ km, $\Delta\theta \sim 30$ mrad), the spatial resolution becomes $\Delta x \sim 30$ m.

Other geophysical methods cannot attain such high spatial resolutions.

Nagamine et al. (1995) did a pioneering work on muography of geophysical targets. They installed a muon telescope consisting of plastic scintillators and photo-multiplier tubes (PMTs) at the foot of Mt. Tsukuba, and succeeded in density estimation inside the mountain. Subsequent measurements were performed at Mt. Asama (Tanaka et al., 2003) and Mt. Iwate (Tanaka et al., 2005) in Japan, with some improvements on detectors. In addition, nuclear emulsions were used as a muography detector in Mt. Asama (Tanaka et al., 2007a), and Showa-Shinzan lava dome of Usu volcanic region (Tanaka et al., 2007b). These measurements visualized vivid two-dimensional images of the internal density of the volcanoes. With the advent of these works, the muography has gained in popularity and spread worldwide.

The muography has been applied to various geophysical targets. Major prior works are as follows: Mt. Asama (Japan) (Tanaka et al., 2003, 2007a, 2010); Mt. Usu (Japan) (Tanaka et al., 2007b); Mt. Satsuma-Iwojima (Japan) (Tanaka et al., 2009, 2014); La Soufriere of Guadeloupe (France) (Lesparre et al., 2012); Mt. Etna (Italy) (Carbone et al., 2014); Puy de Dome (France) (Cârloganu et al., 2013).

§ 1.2 Muography with Nuclear Emulsions

For muography, several types of detectors have been used, such as scintillation detectors (Tanaka et al., 2009; Lesparre et al., 2010, 2012; Tanaka et al., 2014; Ambrosi et al., 2011), gas chamber detectors (Barnaföldi et al.,

2012; Cârloganu et al., 2013) and nuclear emulsions (Tanaka et al., 2007a,b; Dedenko et al., 2014). The present work focuses on the nuclear emulsions. There are two advantages of this type of detector. First, the nuclear emulsion has high angular resolutions in determining the direction of incident particles (typically 5 mrad). This leads to high angular resolutions (small $\Delta\theta$ in Eq. (1)) in muography analysis. Second, the nuclear emulsion is suitable for observations at remote places because it weighs light and does not require electricity for operation. This feature enables us to perform observation close to the summit (small L in Eq. (1)). On the other hand, the scintillation detectors require electricity and the gas chamber detectors require continuous gas circulation during operation. In the cases of these detectors, L have to be large because the detector site is limited to the place where the infrastructure is organized well. From the above discussion, the nuclear emulsion is superior to the other types of detectors in terms of the spatial resolutions (small Δx in Eq. (1)).

One disadvantage of the nuclear emulsion is that it does not provide information on arrival time of particles. Thus, we cannot follow the time variation of the muon intensity or density structure. Meanwhile, the scintillation detectors and gas chamber detectors have a potential for monitoring the time variation. For instance, Tanaka et al. (2014) has succeeded in time sequential imaging of Mt. Satsuma-Iwojima with a scintillation detector. Recently, a research group of gamma-ray astronomy has invented a mechanism of time stamping by using multiple moving stages mounted on emulsions (Rokujo et

al., 2013). However, this mechanism was not employed in the present work.

The emulsion film consists of plastic base and nuclear emulsion gel covering the both sides of the base. The main components of the gels are basically the same as ordinary photographic films, AgBr crystals and gelatin. When a charged particle passes through the gel, AgBr crystals nearby particle trajectories create latent image centers. After chemical development, the latent image centers are grown to visible silver grains and the trajectories of the charged particles become three-dimensional lines of the silver grains. A typical size of the grain is about $0.6 \mu\text{m}$. These lines of silver grains are identified by automated microscope readout systems (eg. Arrabito et al., 2006; Morishima and Nakano, 2010).

Pioneering works on muography with nuclear emulsions were done by Tanaka et al. (2007a) at Mt. Asama and Tanaka et al. (2007b) at Mt. Showa-Shinzan. In the case of Mt. Showa-Shinzan, emulsion detectors with an effective area of 6000 cm^2 were placed at 500 m south of the summit and were exposed to cosmic rays for 3 months. The emulsion detectors consisted of a stack of four emulsion films. As a result, they visualized the shape of the massive lava which is narrowing downwards.

§ 1.3 Accuracy of Muography

Although Tanaka et al. (2007b) has succeeded in muography observation at Showa-Shinzan with nuclear emulsions, there are still remaining problems with accuracy. Firstly, the muographic density of the lava ($2.71 - 2.91 \text{ g/cm}^3$,

the error at each data point is 0.17 g/cm^3) does not agree with the bulk density measured from rock samples (2.32 g/cm^3 by Nemoto et al., 1957). Secondly, this muography observation may suffer from contamination of background noise.

In the following two paragraphs, the problem of background noise is introduced. Some prior muography works on scintillation detectors address an existence of background noise (Okubo and Tanaka, 2012; Carbone et al., 2014). For instance, Carbone et al. (2014) has observed a remarkable difference between observed particle flux and expected muon flux. The observed flux is up to 10 times of the expected muon flux. They attributed this excess to the effect of background noise caused by low-energy particles, such as electrons and positrons.

If the background noise exceeds the weak flux of muons penetrating the mountain, muography may significantly underestimate density of the target mountain. To avoid the underestimation, the prior works propose background subtraction from observed particle flux. For example, Okubo and Tanaka (2012) estimates the noise levels from the flux of nearly horizontal directions and subtract them from the observed fluxes in other directions. Carbone et al. (2014) made a model of the angular dependence of the noise flux by a linear regression analysis and subtract the noise flux from the observed flux. Contrary to the numerous efforts on background subtraction, it should be noted that these subtraction methods are based on artificial assumptions and significant systematic uncertainty still remains in estimated

density. This fact is acknowledged by the Carbone et al. (2014). They admit that the muon flux derived from the subtraction method cannot be used for precise quantitative analysis.

To improve accuracy of muography with nuclear emulsions, it is necessary to understand the characteristics of the background particles and to develop emulsion detectors which can reject them.

§ 1.4 Candidates for Background Noise

The origin of background noise in muography has not been understood yet. This subsection discusses candidates for sources of background noise. The candidates are environmental radioactivity, electromagnetic components of cosmic rays and hadronic components of cosmic rays.

§ 1.4.1 Environmental Radioactivity

The first candidate is environmental radioactivity. In conclusion, it does not matter to ordinary muographic detectors. Environmental α and β rays are definitely absorbed in cabinets of detectors. For instance, Tanaka et al. (2007a) succeeded in reducing β rays from ^{40}K by covering emulsion detectors with 3-mm-thick iron plates on both sides. Although some of the environmental γ rays can penetrate the detector cabinets, the converged electrons are not so energetic ($<$ a few MeVs) that ordinary muographic detectors cannot trace them.

§ 1.4.2 Electromagnetic Components

The second candidate is the electromagnetic component of cosmic rays (electrons, positrons and photons) mainly from electromagnetic cascades. The cascade is initiated by the decay of neutral and charged mesons. They can be the source of the background noise, because they are scattered into the detector from random directions. Particularly, the contamination of low-energy electrons are crucial.

Electrons and positrons are most numerous near the critical energy, at which the radiative energy loss exceeds the ionization energy loss (81 MeV in air). The total vertical intensity of electrons plus positrons is roughly, 30, 6 and $0.2 \text{ m}^{-2}\text{sec}^{-1}\text{sr}^{-1}$ above 10, 100, and 1000 MeV, respectively (Beringer et al., 2012). A dedicated study shows that the ratio of electrons plus positrons to muons is $\sim 1\%$ at 1 GeV, and it increases drastically to $\sim 20\%$ at 300 MeV (Golden et al., 1995). This implies that the electromagnetic component dominates the ionizing particles at low energy region below the critical energy (81 MeV). These low-energy electrons (positrons) are deflected with large angles in the air. Thus, they could hit the detector from unexpected paths and cause background noises.

In prior works (Tanaka et al., 2007a,b), 3-mm-thick iron plates (2.3 g/cm^2) were used to block the environmental radioactive particles. These plates, however, cannot stop electrons with kinetic energy $>\sim 10 \text{ MeV}$.

§ 1.4.3 Hadronic Components

The last candidate is the hadronic components of cosmic rays, mainly protons and neutrons. The discussion on hadronic components has not been sufficient in the context of muography. Hadronic components can be the source of the background noise, because nuclear emulsions are sensitive to protons and because hadronic components would produce charged particles near the detector by hadronic interaction with nuclei of the atmosphere and material near the detector.

The hadronic components are more abundant than electromagnetic particles at sea level above 1 GeV. The integral intensity of vertical protons above 1 GeV/c at sea level is $\sim 0.9 \text{ m}^{-2}\text{s}^{-1}\text{sr}^{-1}$ (Grieder, 2001). The ratio of vertical protons to vertical muons is $\sim 1\%$ at 2 GeV and it increases to $\sim 5\%$ at 0.25 GeV (Brooke and Wolfendale, 1964). Thus, the contamination of low-energy protons should be concerned in the same way as electromagnetic components.

§ 1.5 Emulsion Cloud Chamber

As seen in the previous sections, the background noise mimics the penetrating muons which are used for density estimation with muography. Although some prior works have proposed methods for estimation of background levels and subtraction, significant systematic errors still remain. It is therefore necessary to reject these noise particles with some improvements on emulsion

detectors. The origins of the background noise has not been understood yet. However, there are two candidates for that: the electromagnetic components and the hadronic components of cosmic rays. As described in the previous subsection, the two components are abundant at low energy. The low energy particles are deflected with large angles in the atmosphere and they could hit the detector from unexpected paths. Thus, I present a hypothesis that the background noise are caused by low-energy charged particles.

To reduce the low-energy charged particles, this work proposes the use of the Emulsion Cloud Chamber (ECC). ECC is made of a repeated structure of emulsion films and passive metal plates. This detector makes it possible to reject low-energy particles, because low-energy particles are deflected with larger angles in the metal plates than signal muons. Thus, high-resolution microscopic analysis of the tracks enables us to distinguish signal tracks from noise tracks.

Emulsion Cloud Chamber (ECC) was originally invented for a study of multiple production of mesons by high-energy cosmic rays. ECC played an important role in the early age of high-energy and cosmic-ray physics. For instance, Niu et al. (1971) found a decay in flight of unexpected particle (X-particle) in ECC. This particle is what we call charm quark in the context of the standard model. Nishimura et al. (1980) measured a precise energy spectrum of primary cosmic-ray electrons in TeV region. Recently, ECC is used for a verification of neutrino oscillation ($\nu_\mu \rightarrow \nu_\tau$) in the OPERA (Oscillation Project with Emulsion-tRacking Apparatus) experiment. In this experiment,

150 thousands of ECC modules each of which consists of 57 emulsion films (300-micron-thick) and 56 lead plates (1-mm-thick) were exposed to the neutrino beams from CERN. Until now, four candidates of ν_τ events have been observed (Agafonova et al., 2014).

§ 1.6 Overview

In §2 the performance of background noise reduction is demonstrated by a test experiment with a prototype of ECC detector. The experiment was taken place in Mt. Showa-Shinzan. Volcanological backgrounds on this volcano is given in Appendix A. In §3 three pieces of evidence are presented to support the performance of background reduction with ECC detector. Firstly, muographic density derived from ECC detector is compared with the density of sampled rocks. Secondly, the ECC result is combinedly used with gravity data for 3-D density analysis. Thirdly, the ECC result is compared with Monte Carlo simulation of background noise. Overall discussion and conclusions are given in §4 and §5. To avoid redundant description, details of technical developments on joint inversion and Monte Carlo simulation are explained in Appendix C and Appendix D.

§ 2 Background Reduction and Efficiency Correction

This section focuses on the improvement of emulsion detectors. Specifically, the performance of the background reduction is demonstrated via a test experiment with a prototype of ECC. The prototype is made of twenty OPERA films^{*1} and nine 1-mm-thick lead plates. For comparison, a conventional emulsion detector which is just a stack of four OPERA films, was prepared. It is called quartet detector. In this test experiment, these two detectors were installed at the foot of Showa-Shinzan Lava Dome and were exposed to cosmic rays. The experimental setup is given in § 2.2. Some of the contents in this section has already been published in Nishiyama et al. (2014a).

§ 2.1 Overview

Fig.1 shows the procedure of the whole analysis. The films after the exposure are chemically developed and read by the automated microscope (§ 2.3). The track reading and the reconstruction have already been established by prior works (Arrabito et al., 2006; Tioukov et al., 2006). The important processes in muography are the track selection and efficiency estimation. The track selection is important because the reconstructed tracks contain the noise

^{*1}OPERA films were developed by F-lab of Nagoya University and FUJIFILM Co. for the OPERA (Oscillation Project with Emulsion-tRacking Apparatus) experiment. See Nakamura et al. (2006) for details.

tracks. The efficiency estimation is essential to get the absolute flux of the selected particles. These topics are described in § 2.4 and § 2.5. After that the particle flux is estimated by efficiency correction and is converted into average density along muons trajectories (§ 2.6).

§ 2.2 Experimental Setup

In this experiment, OPERA films (Nakamura et al., 2006) are used as muography detector. The dimensions of the OPERA film are given in Table 1. Two types of detectors were built using OPERA films. One is a stack of four films (quartet detector). The films are packed in twos in light-shielding envelopes. Thus, the quartet detector comprises two envelopes. The other is a stack of 20 emulsion films and nine lead plates (ECC detector). The ECC detector comprises ten envelopes. The nine lead plates are inserted between each pair of the envelopes. The thickness of the lead plates is determined to be 1 mm so as to deflect charged particles below 1 GeV with larger angles than resolutions of microscopic analysis. The two detectors were covered with two 3-mm-thick iron plates on the both sides to protect them from environmental radioactivity (Tanaka et al., 2007a). Fig.2 represents the schematic views of the detectors. The objective of this experiment is to perform a comparison between two detectors with different energy thresholds. As discussed in § 2.4.1, typical values of the energy thresholds of quartet and ECC detector are 50 MeV and 1 GeV, respectively.

The two detectors were installed 500 m west of the summit of Mt. Showa-Shinzan in Usu volcanic region (see Appendix A for geological backgrounds). One week before the installation, all the films were refreshed in a high temperature and humidity place. The detectors were fabricated just before the installation to reduce the chance coincidence of the tracks which are recorded during transportation. The exposure time was 168 days (21 November 2011 - 7 May 2012). The maximum and minimum temperature during exposure was $+15.9^{\circ}\text{C}$ and -8.8°C , respectively.

The position of the detector is represented in Fig.3. The thickness of rock along the radial directions of the detector is shown in Fig.4. The coordinate system employed in this study is represented in Fig.5. The z axis of the coordinate system is taken perpendicular to the detector plane. The track orientation is then represented by $\tan \theta_x$ and $\tan \theta_y$, where θ_x and θ_y are the angles with respect to the film's normal projections on the xz and yz planes, respectively. The inclination of a track is defined as the angle between the track and the detector normal:

$$\tan \theta = \sqrt{\tan^2 \theta_x + \tan^2 \theta_y}. \quad (2)$$

The inclination is an important parameter, because the angular resolutions and the film efficiency depend on θ . In this coordinate system, tracks with $\tan \theta_y > 0$ are particles coming from the front (Mt. Showa-Shinzan side), $\tan \theta_y < 0$ from the rear (Mt. Usu side), and $\tan \theta_y = 0$ horizontal particles. Note that this classification is valid for downward-going particles. The sign

becomes opposite for upward-going particles.

width \times height	12.3 cm \times 9.8 cm
depth of emulsion layer	44 μm \times 2
depth of plastic base	210 μm

Table 1: Dimensions of OPERA films.

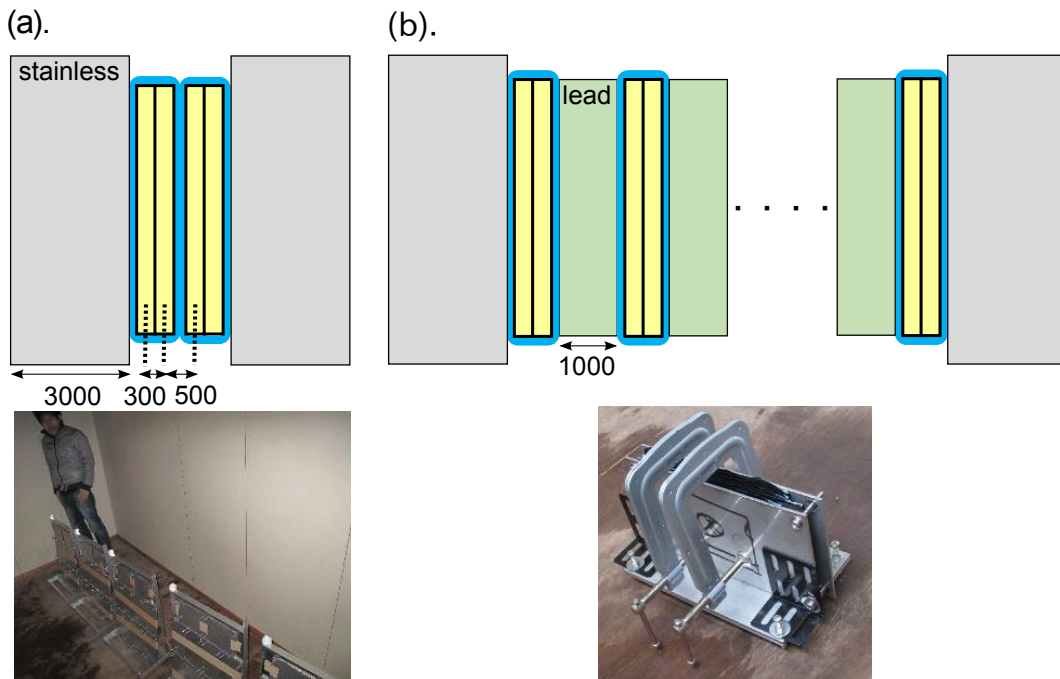


Figure 2: Schematic side views of two types of emulsion detectors with dimensions given in microns. (a) Quartet detector: emulsion films, packed in twos in light-shielding envelopes stacked between 3-mm-thick stainless plates to ensure planarity. (b) ECC detector: ten envelopes and nine 1-mm-thick lead plates, covered with two 3-mm-thick stainless plates.

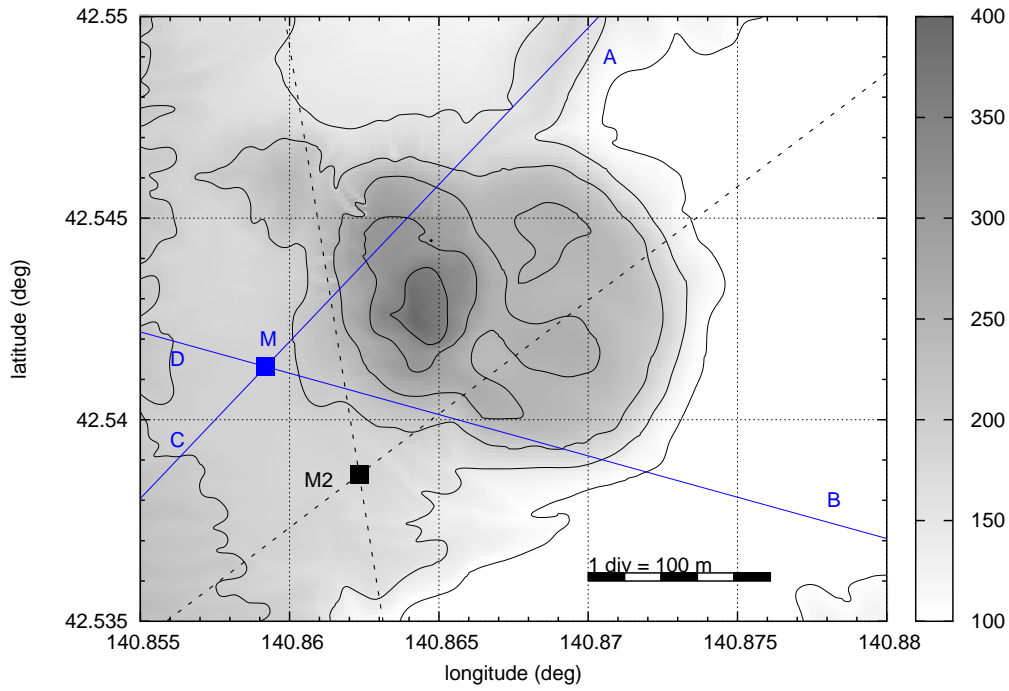


Figure 3: Topographic map of Mt. Showa-Shinzan with “M“ showing the position of the quartet and ECC detectors. The viewing angle of the detectors is given by $\angle AMB$ (forward) and $\angle CMD$ (backward). M2 denotes the position of the detector of the prior work by Tanaka et al. (2007b).

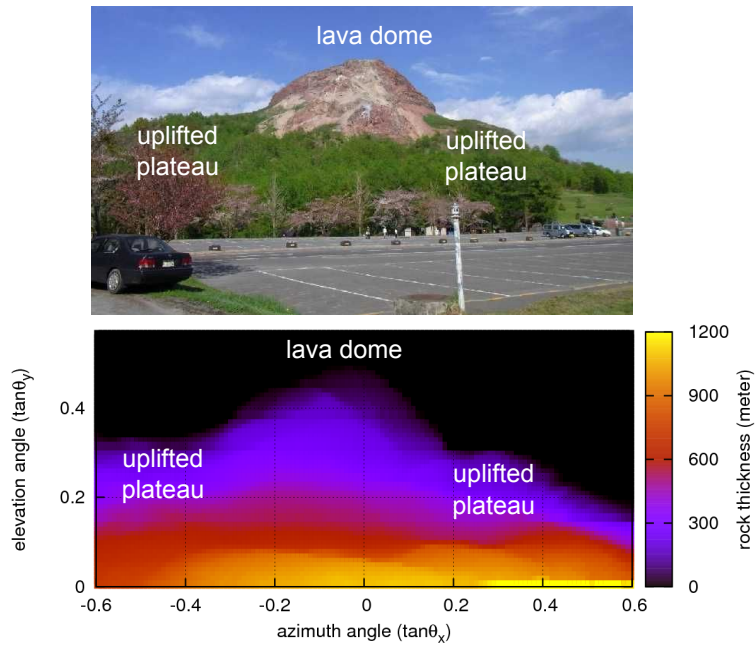


Figure 4: Thickness of rock along the radial directions from the detector site. The picture is taken from near the detector site.

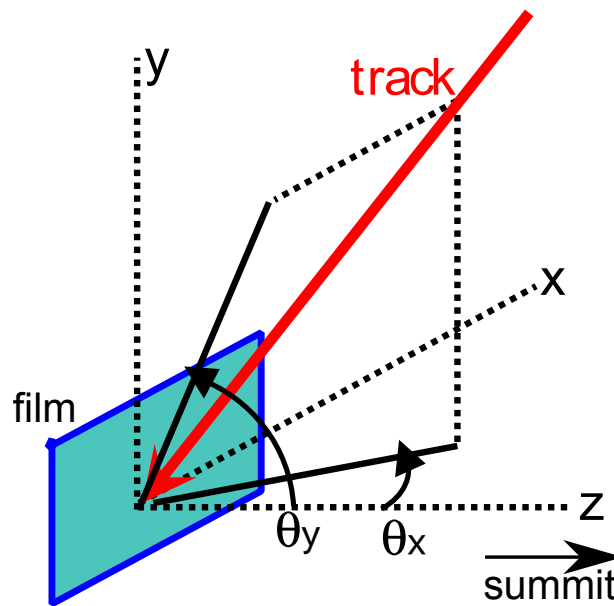


Figure 5: Emulsion coordinate system for identifying the position and direction of incident particles.

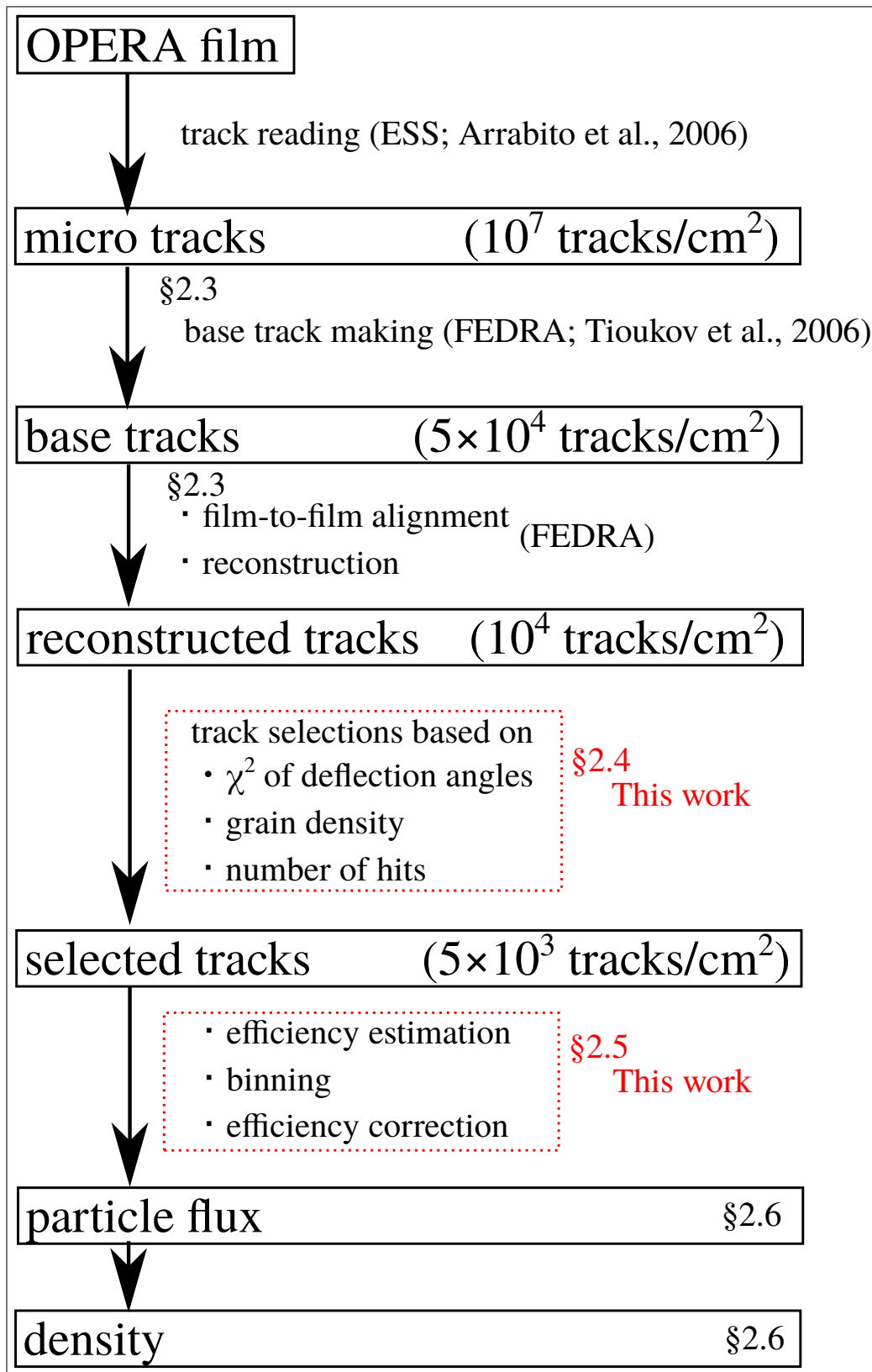


Figure 1: Data flow of the analysis.

§ 2.3 Scanning and Reconstruction

§ 2.3.1 Development

The exposure was finished on 7 May 2012. All the emulsion films were scrambled and sent to the development facility in F-lab, Nagoya University. The films were developed on 9 May 2012. The procedure was as follows (see Nakamura (2005) for details).

Development

The films are soaked in XAA developer for 25 minutes. In this process, the latent image centers in the emulsion layers are grown to be visible grains.

Stop

The films are transferred into an acetic acid solution to stop the development process.

Fixing

This process dissolves the AgBr crystals which could not become silver grains into fixer solution.

Washing

The films were put in running water to wash the chemicals.

Swelling

After the processes above, the thickness of the film becomes only half

of the original thickness. The films are swelled to the original thickness in a glycerol solution.

Drying

The films are dried in a clean room.

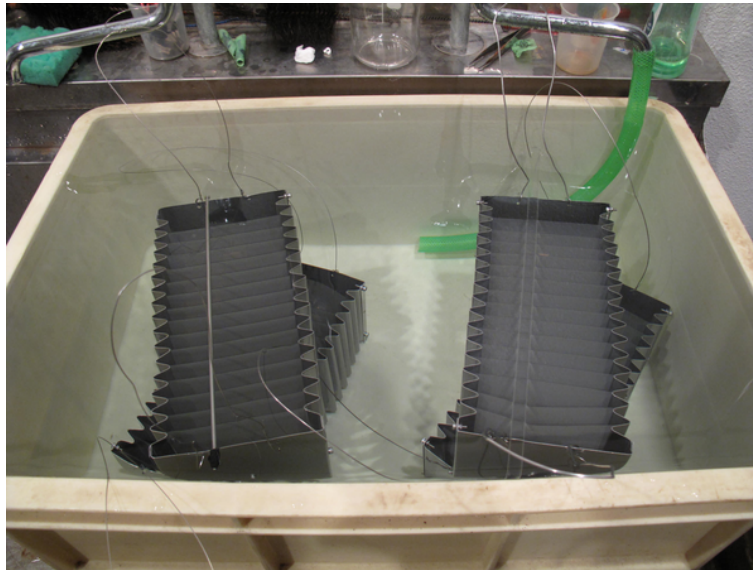


Figure 6: OPERA films after development and in the washing process.

§ 2.3.2 Scanning

After the films were developed, the tracks recorded in the emulsion films were read using ESS (European Scanning System, Fig.7) (Arrabito et al., 2006). The main components of the system are (i) a motor driven scanning stage for horizontal motion; (ii) a motor driven stage vertically mounted on the rigid frame; (iii) optics and digital camera mounted on the vertical stage; (iv) an illumination system located below the horizontal stage. The vertical stage plays a role of focusing. The horizontal stage shifts the field of view

($\sim 350 \mu\text{m} \times 350 \mu\text{m}$). The scanning system outputs the position, direction and linear density of the silver grains. The information were then converted to ROOT ^{*2} Tree formats for convenience of post-processing.

In the present work, 24 films were scanned (4 films from quartet detector and 20 films from ECC detectors). The scanning area was a rectangle region of $11.2 \text{ cm} \times 9.3 \text{ cm}$ for each film. The scanning speed was approximately $7.5 \text{ cm}^2/\text{hour}$. It took four months (25 May 2012 - 29 August 2012) for scanning including dead time for plate changing, machine troubles and trial & error.

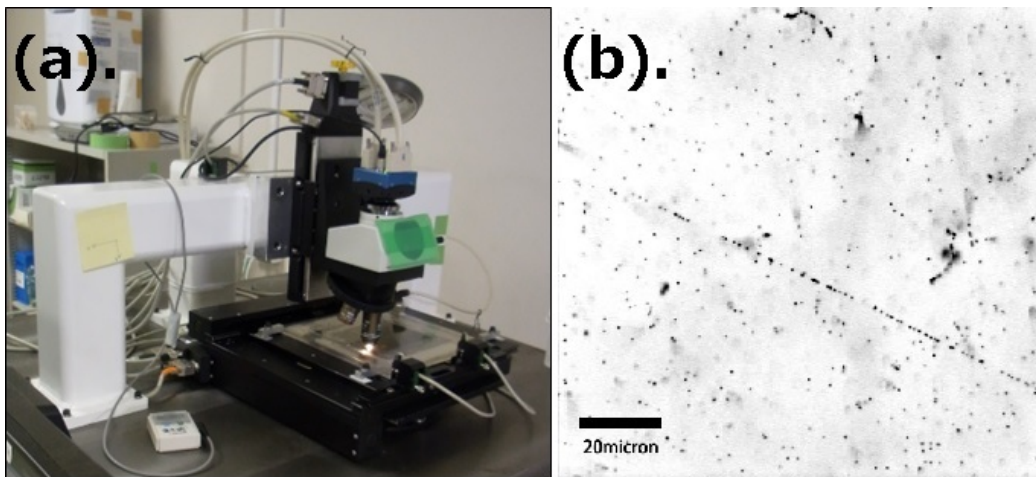


Figure 7: (a) European Scanning System (ESS) installed at Earthquake Research Institute, the University of Tokyo. (b) Microscopic image of a nuclear emulsion after development.

§ 2.3.3 Reconstruction

The post-processing was performed using FEDRA (Framework for Emulsion Data Reconstruction and Analysis) (Tioukov et al., 2006). The procedures

^{*2}ROOT (<https://root.cern.ch/>) is a package for data analysis widely used by researchers in high energy physics. I/O of the FEDRA system is based on ROOT.

are as follows: (i) base track making; (ii) film-to-film alignment; (iii) track reconstruction.

Base track making

The tracks recorded on two sides of the emulsion layers are linked and evaluated in this process. Fig.8 shows the distribution of grain linear density (GD) and straightness of tracks (χ_{BT}^2) of the resultant base tracks. Fig.8 shows two peaks: (1) the peak of true signals and (2) the peak of accidental coincidence of random fogs and fragments of environmental radioactive particles. Since the two peaks are clearly separated, low GD and high χ_{BT}^2 tracks were eliminated.

Film-to-film alignment

The film-to-film alignment is necessary for track reconstruction because alignment between films is unknown beforehand. The alignment of two films is defined by the affine parameters ($\Delta x, \Delta y, a, b, c, d$) and the gap (Δz). The base track found at (x_i, y_i, z_i) in the local coordinate system on the i th film can be transformed into the coordinate system on the $(i + 1)$ th film as

$$\begin{pmatrix} x_{i+1} \\ y_{i+1} \\ z_{i+1} \end{pmatrix} = \begin{pmatrix} a & b & 0 \\ c & d & 0 \\ 0 & 0 & 1 \end{pmatrix} \begin{pmatrix} x_i \\ y_i \\ z_i \end{pmatrix} + \begin{pmatrix} \Delta x \\ \Delta y \\ \Delta z \end{pmatrix}. \quad (3)$$

First, these seven parameters were estimated using relatively straight base tracks. Some of the resultant parameters are shown in Table 2.

Second, the entire film is divided into small parts and local correction was performed for each subdivided view.

Track reconstruction

The tracks recorded in several films were linked in this process. The process began from the tracks in the first film of the detector and seek subsequent films for tracks that can be connected. The local correction of alignment and the track reconstruction were repeated many times until the resultant alignment parameters are converged (Fig.9).

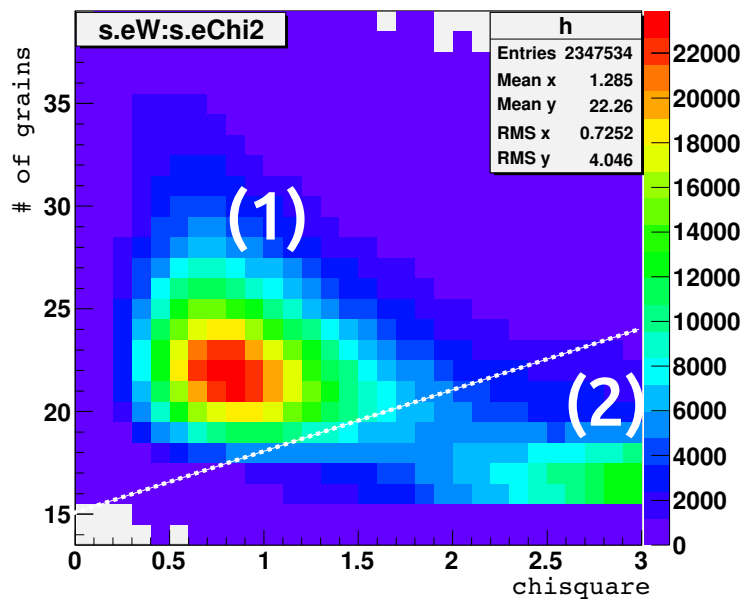


Figure 8: Distribution of grain number and χ_{BT}^2 of the base tracks in the first film of the quartet detector. The two peaks of (1) true signals and (2) accidental coincidence of random fogs and fragments of environmental radioactive particles are clearly separated. The white dotted line is the threshold for separation.

	(a) no lead	(b) beyond lead
Δz (microns)	294.9	1593.4
a	0.9997	1.0007
b	-0.0012	0.0008
c	0.0013	-0.0010
d	0.9998	1.0009
Δx (microns)	-582.5	1711.3
Δy (microns)	-129.3	-810.0

Table 2: Alignment parameters between (a) 1st and 2nd film in ECC detectors and (b) 2nd and 3rd film in ECC detectors.

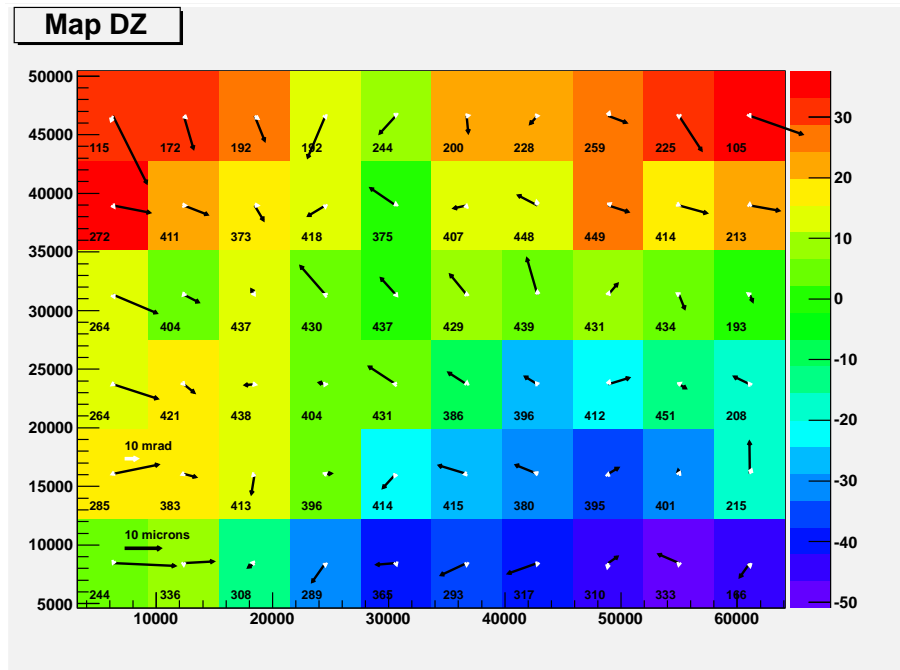


Figure 9: Results of local correction in alignment between 1st and 2nd film in ECC detector. The entire film is divided into small views with local deviation on Δz (color) and Δx & Δy (black arrow), and angular correction (white arrow) estimated for each view. The values in the views indicate the number of tracks used in the local correction.

§ 2.4 Track Selection

Since the reconstructed tracks contain noise tracks, an original selection was applied to the reconstructed tracks. The selection was based on (i) χ^2 of deflection angles, (ii) grain density, and (iii) number of hits.

§ 2.4.1 χ^2 of deflection angles

In order to select tracks with straight trajectories in the detector, the straightness of the track is evaluated by focusing on deflection angles. The deflection angles are measured in a radial and transverse coordinate system. A scheme of the coordinate system is illustrated in Fig.10. The deflection angle is defined as a vector between two base tracks. The vector can be decomposed into the radial component along the base track and its transverse component. As shown in Fig.11, the angular error in the radial and transverse components have different dependency on inclination (Agafonova et al., 2012), owing to the optics of the microscope. Here, we can introduce an index of straightness χ^2 of reconstructed tracks, which is defined as

$$\chi^2 = \sum_i^{n-1} \left(\frac{\Delta\theta_{R,i}^2}{\sigma_R^2} + \frac{\Delta\theta_{T,i}^2}{\sigma_T^2} \right), \quad (4)$$

where n is the number of the films in which base tracks are found, $\Delta\theta_{R,i}$ and $\Delta\theta_{T,i}$ are the deflection angles between i -th pair of the segments in radial and transverse coordinate system, and σ_R and σ_T are the angular measurement errors in the radial and transverse components. The χ^2 values were computed for all the reconstructed tracks. If a track is completely

straight, the resultant χ^2 values should follow χ^2 -distribution. Thus, tracks with p-values > 0.01 (1%) were selected.

The surviving rate of this selection is estimated for the quartet and ECC detectors by using GEANT4 (Agostinelli et al., 2003). The deflection angles in each detector ($\Delta\theta_{R,i}$ and $\Delta\theta_{T,i}$) are calculated for muons, protons and electrons with kinetic energy of 10 MeV to 100 GeV. For each particle and energy, the probability where the resultant χ^2 meets the criterion (p-value $> 1\%$) is taken as a surviving rate. Fig.12 shows the surviving rate as a function of kinetic energy for the quartet and ECC detectors. For convenience, the energy threshold is defined as the energy at which the surviving rate exceeds 50%. The energy thresholds estimated from this study are tabulated in Table 3.

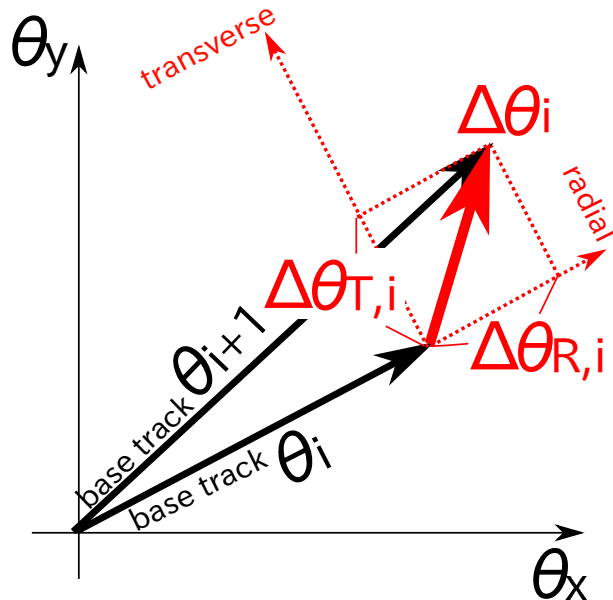


Figure 10: A schematic view of the radial and transverse coordinate system. The deflection angle $\Delta\theta$ is defined as a vector between slopes of the two base tracks. The deflection angle can be decomposed into radial components along the original base track direction and its transverse component.

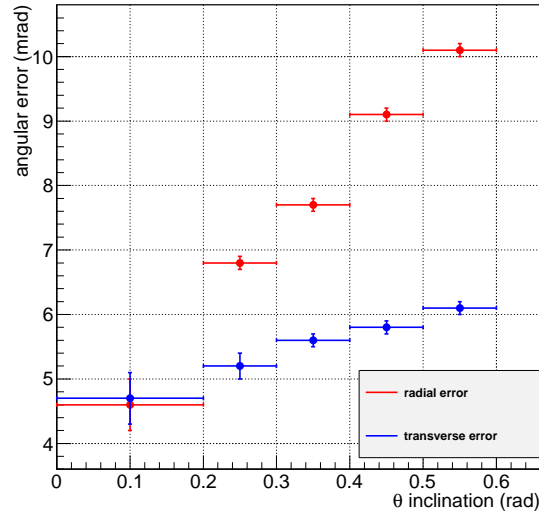


Figure 11: Angular resolutions in the radial (red) and transverse (blue) coordinates. The horizontal axis represents the inclination, the angle between a track and the normal of the film.

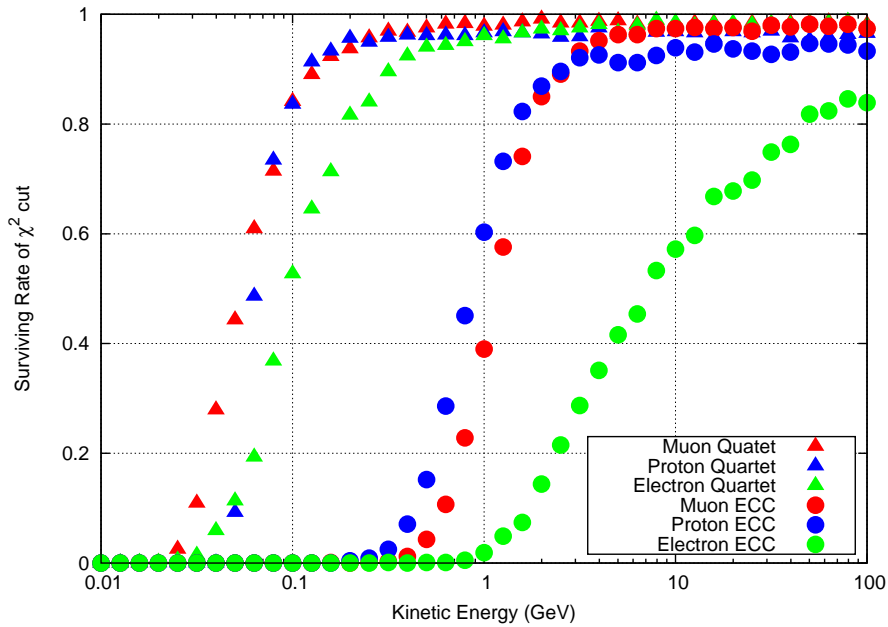


Figure 12: The surviving probability of χ^2 -cut for muons (red), protons (blue) and electrons (green), calculated using GEANT4. The circles represent the surviving probability of ECC detector, and the triangles represent the surviving probability of quartet detector.

	muons	protons	electrons
Quartet	50 MeV	60 MeV	100 MeV
ECC	1.2 GeV	1 GeV	8 GeV

Table 3: The energy thresholds at which the surviving rate exceeds 50%.

§ 2.4.2 Grain density

The grain density (GD) refers to the number density of silver grains along a track. It positively correlates with the ionizing power of incident particles. This feature has been used for particle identification. For instance, Toshito et al. (2004) has succeeded in discriminating tracks of 1.2 GeV/c pions and 1.2 GeV/c protons using ECC.

Fig.14 is a GD distribution of the nearly perpendicular tracks in the quartet detector. The distribution shows clear two peaks. Considering the ionization energy loss of the major cosmic particles at near the energy threshold (~ 0.1 GeV) shown in Fig.13, the first peak is a contribution of relativistic particles (muons and electrons above ~ 0.1 GeV and protons above 1 GeV). The second peak is a contribution of non-relativistic particles (protons below 1 GeV). This distribution can be approximated by a sum of the two Gaussian distributions ($\chi^2 = 2.7$, $\text{ndf} = 5$). Since signal muons are in the peak (i), the tracks with GD of less than $+2\sigma$ point of the first Gaussian distribution were selected. In the case of the ECC detector (Fig.15), the GD distribution yields a single peak of (i), because low-energy protons (< 1 GeV) were rejected by

χ^2 -cut. The distribution was approximated by a single Gaussian distribution ($\chi^2 = 14.1$, $\text{ndf} = 8$). The tracks with GD of less than $+2\sigma$ point were selected.

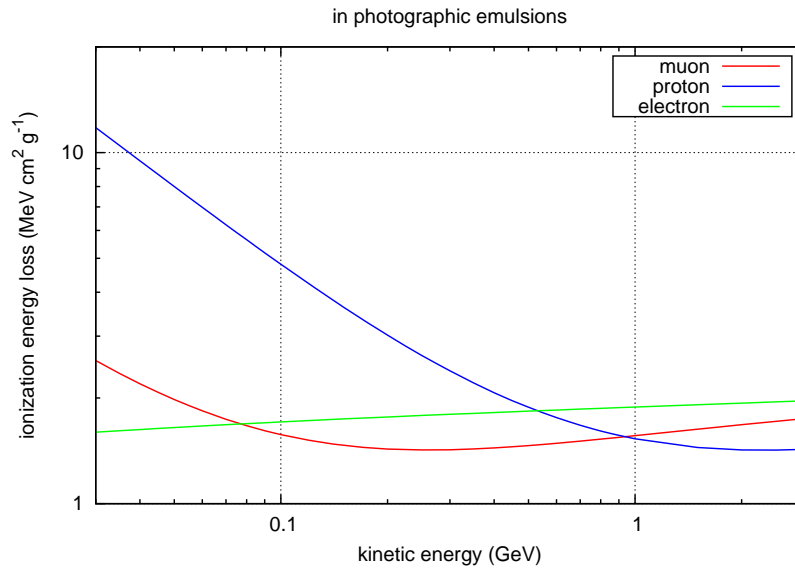


Figure 13: The energy loss by ionization process for muons, protons and electrons in photographic emulsions. Data are taken from Groom et al. (2001) and NIST Standard Reference Database 124. The ionization power of the proton is apparently higher than those of the muon and electron at low energy (~ 0.1 GeV) and they become comparable above 1 GeV.

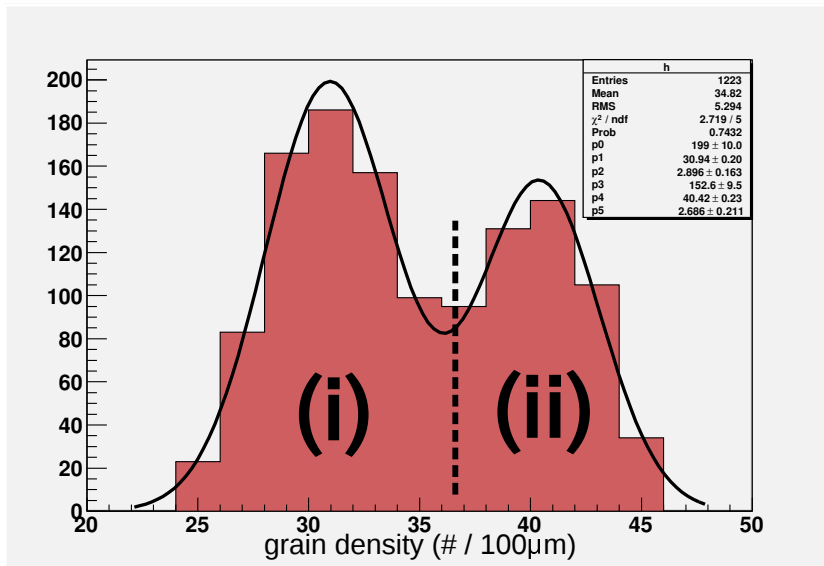


Figure 14: Distribution of grain density (GD) for nearly perpendicular tracks ($\theta < 0.1$) in quartet detector. The tracks with GD $< +2\sigma$ point of the first peak (dashed line) are selected.

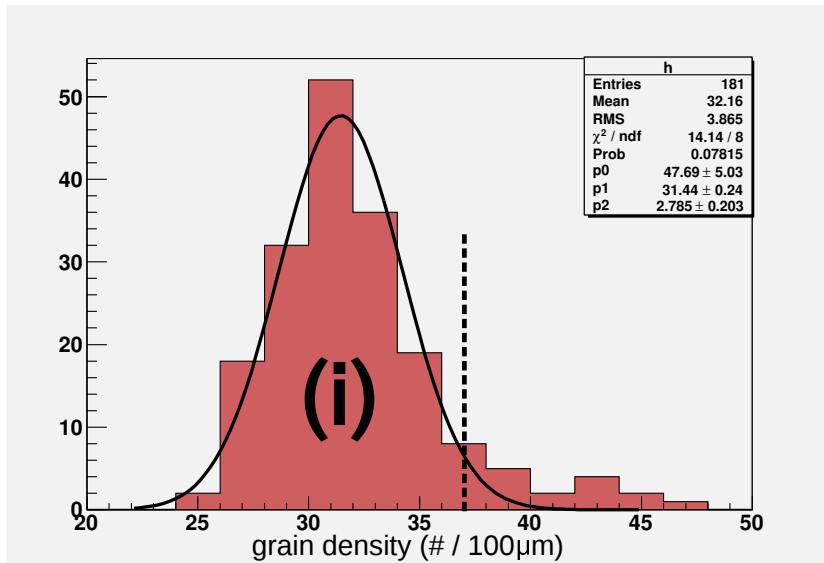


Figure 15: Distribution of grain density (GD) for nearly perpendicular tracks ($\theta < 0.2$) in ECC detector. The tracks with GD $< +2\sigma$ point of the peak (dashed line) are selected.

§ 2.4.3 Number of Hits Selection

In order to eliminate chance coincidence of the tracks recorded during transportation of the films, a selection based on the number of hits was applied. The number hits (n) refers to the number of the films where segments of the tracks were found among the total number of the films ($N_Q = 4$ and $N_{ECC} = 10$). Fig.16 shows an example of n distributions for the selected tracks of the quartet and ECC detectors. Along with the n distribution, the probability that the tracks recorded during transportation are mistakenly identified as signals by giving a misalignment of $500 \mu\text{m}$ in x and y directions between adjacent films (blue histograms in Fig.16). To exclude these fake coincidence signals, the tracks whose segments were found at least in three films were selected ($n \geq 3$).

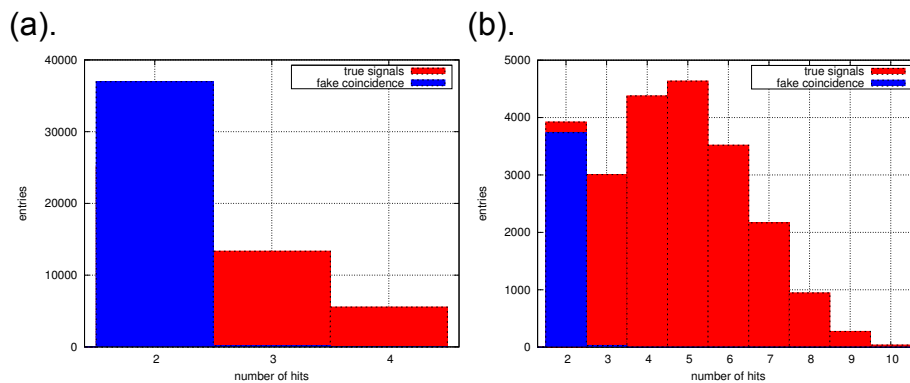


Figure 16: (a) Number-of-hits (n) distribution among the four films in the quartet detector for tracks with inclination of $0.2 \leq \theta < 0.3$. The blue histogram represents the probability of misreconstruction of the tracks recorded in transportation (fake tracks). (b) Number-of-hits distribution among the ten films in the ECC detector for tracks with inclination of $0.2 \leq \theta < 0.4$.

§ 2.5 Efficiency Study

This subsection describes the method which I have developed for efficiency correction. The efficiency correction is necessary for converting the number of signal particles into the particle flux. Some prior works in the OPERA experiment report that the efficiency of the OPERA film depends strongly on the inclination angle θ (eg. Arrabito et al., 2007). However, the early muographic observations with nuclear emulsions (Tanaka et al., 2007a,b) have not considered this effect. In the present work, I determined the efficiency of the quartet detector and its θ dependence by improving a pre-existing method (Arrabito et al., 2007) (§ 2.5.1). Whereas, this method cannot be applied in the case of ECC detector, because the previous method does not take into account the loss of efficiency in reconstruction. Unfortunately, the previous method overestimates the efficiency of ECC detector. Thus, I developed a method for precise determination of total efficiency including the loss arising from the reconstruction and the selection for ECC detector (§ 2.5.2).

§ 2.5.1 Quartet Detector

The film efficiency is defined as the probability of detecting a track in a film when a particle passes through it. Given the efficiency values of the quartet films, $\epsilon_1, \epsilon_2, \epsilon_3$, and ϵ_4 , the probability that tracks are found in at least three films among the total of four films can then be expressed as

$$\epsilon_{\text{tot}}^Q = \epsilon_1 \epsilon_2 \epsilon_3 \epsilon_4 + (1 - \epsilon_1) \epsilon_2 \epsilon_3 \epsilon_4 + \epsilon_1 (1 - \epsilon_2) \epsilon_3 \epsilon_4 + \epsilon_1 \epsilon_2 (1 - \epsilon_3) \epsilon_4 + \epsilon_1 \epsilon_2 \epsilon_3 (1 - \epsilon_4). \quad (5)$$

The film efficiency values are estimated for fifty inclination ranges from the ratio of triplet-hit signals and quartet-hit signals:

$$\epsilon_i[\theta_{\min}^Q : \theta_{\max}^Q] = \frac{N_4[\theta_{\min}^Q : \theta_{\max}^Q]}{N_{3,i}[\theta_{\min}^Q : \theta_{\max}^Q] + N_4[\theta_{\min}^Q : \theta_{\max}^Q]}, \quad (6)$$

where $N_4[\theta_{\min}^Q : \theta_{\max}^Q]$ is the number of the quartet-hit tracks with inclination within $\theta_{\min}^Q \leq \theta^Q < \theta_{\max}^Q$, and $N_{3,i}$ is the number of the tracks found in three films and not found in the i th film. Fig.17 represents the total efficiency. The total efficiency is $\sim 80\%$ at $\theta = 0$ and decreases rapidly to $\sim 40\%$ at $\theta = 0.3$. The efficiency for each film is $\sim 80\%$ at $\theta = 0$ and decreases to $\sim 60\%$ at $\theta = 0.3$. Unfortunately, the efficiency of the OPERA film is not desirable. This is probably because of aged deterioration of the film after production.

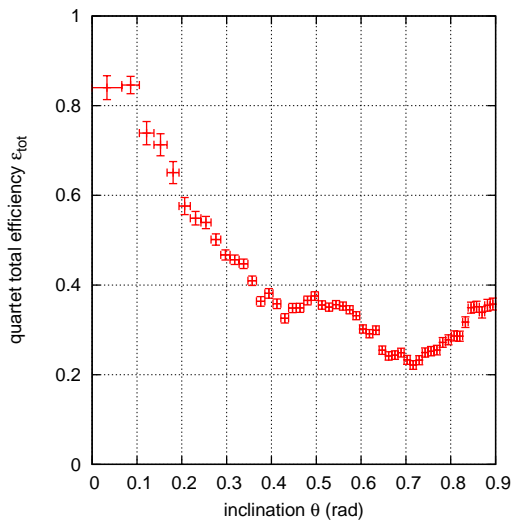


Figure 17: Total efficiency of the quartet detector as a function of track inclination θ .

§ 2.5.2 ECC Detector

The method used in the quartet detector is not applicable to the ECC detector. As a reason for that, let us suppose the efficiency of the film is $\epsilon = 60\%$. Then the total efficiency should be the probability that tracks are found at least three films out of twenty films, thus it becomes almost 100%. However, the actual efficiency is much lower because we lose efficiency during the track reconstruction and the track selection. For ECC detector, an alternative method for efficiency estimation was required.

I have established "odd & even method" for precise efficiency analysis of ECC. The scheme of the new method is illustrated in Fig.18. To be concrete, the twenty films constituting the ECC detector were divided into odd group (1, 3, \dots , 17, 19-th films) and even group (2, 4, \dots , 18, 20-th films). The reconstruction and selections were performed independently for the odd and even groups. Then, the resultant tracks the two groups were compared. The efficiency of the odd/even detector is expressed as,

$$\epsilon_{\text{ODD}} = \frac{N\{\text{ODD} \cap \text{EVEN}\}}{N\{\text{EVEN}\}}, \quad (7)$$

and

$$\epsilon_{\text{EVEN}} = \frac{N\{\text{ODD} \cap \text{EVEN}\}}{N\{\text{ODD}\}}, \quad (8)$$

where $N\{\text{ODD}\}$ and $N\{\text{EVEN}\}$ are the numbers of the resultant tracks in the odd and even groups, and $N\{\text{ODD} \cap \text{EVEN}\}$ is the number of the tracks commonly found in the odd and even groups. A degree of matching between the odd and even groups is evaluated by distance (< 20 microns) and angle

(< 20 mrad) of the two tracks (Fig.19). The total efficiency is the probability that tracks are found either in the odd group or in the even group:

$$\epsilon_{\text{tot}} = 1 - (1 - \epsilon_{\text{ODD}})(1 - \epsilon_{\text{EVEN}}). \quad (9)$$

The estimated total efficiency is represented in Fig.20.

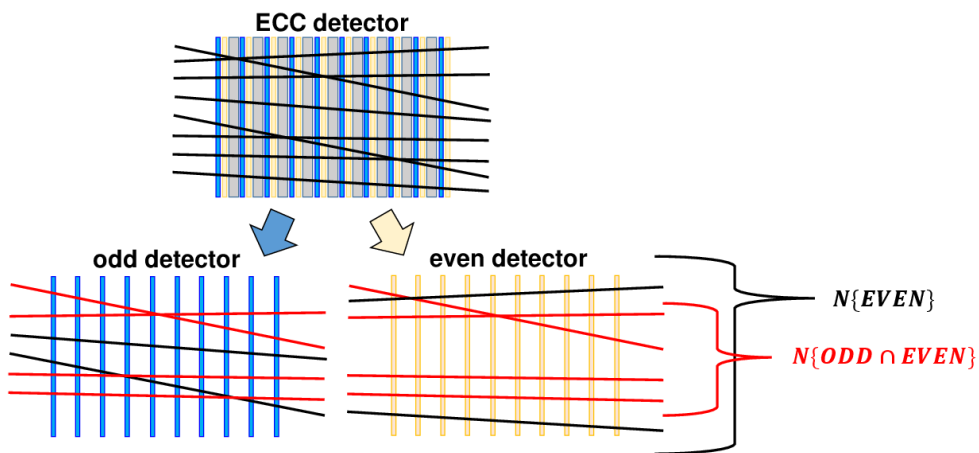


Figure 18: Schematic illustration of "odd & even" method. The twenty films constituting the ECC detector are divided into odd and even groups. The efficiency estimation is performed by focusing on the number of tracks ($N\{EVEN\}$) and the number of tracks which are commonly found in the odd and even groups $N\{ODD \cap EVEN\}$. For example, the efficiency of the odd detector is given by $N\{ODD \cap EVEN\}/N\{EVEN\}$, and vice versa.

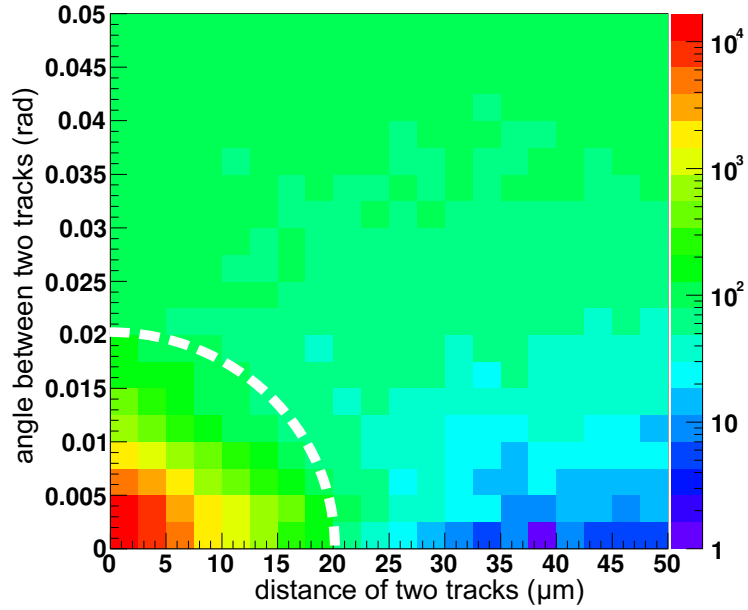


Figure 19: Distance and angle of two tracks in the odd and even groups. The tracks inside the dashed arc are judged to be the common tracks.

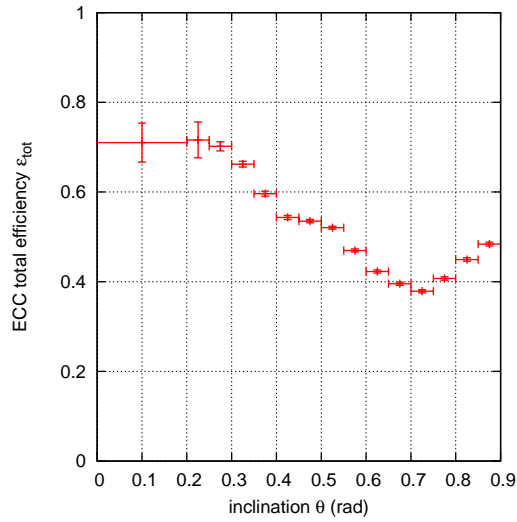


Figure 20: Total efficiency of the ECC detector as a function of track inclination θ .

§ 2.6 Results

§ 2.6.1 Particle Flux

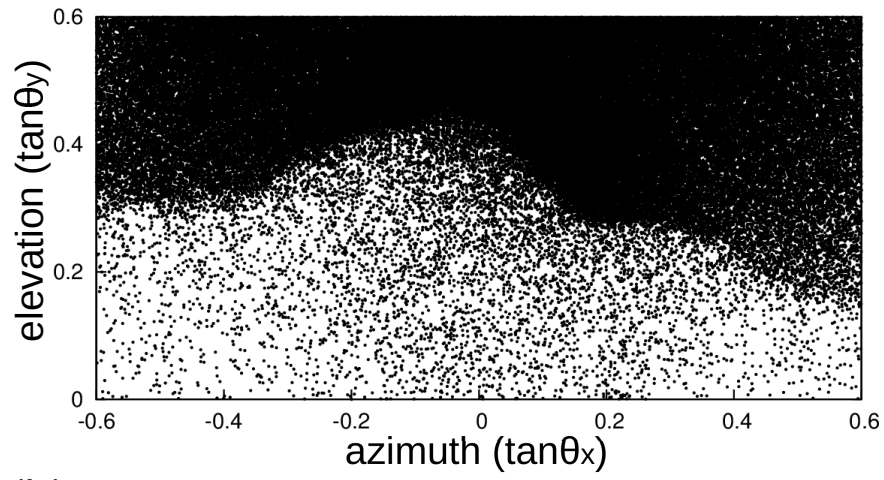
The angular distributions of the selected tracks are shown in Fig.21. Particle flux from a solid angle spanned by D [$\tan \theta_{x,\min} : \tan \theta_{x,\max}, \tan \theta_{y,\min} : \tan \theta_{y,\max}$] is derived from the number of selected tracks and the total efficiency values:

$$F = \frac{1}{\int_D S \cos \theta T d\Omega} \left(\sum_i \frac{N[\theta_{i,\min} : \theta_{i,\max}]}{\epsilon_{\text{tot}}[\theta_{i,\min} : \theta_{i,\max}]} \right), \quad (10)$$

where $N[\theta_{i,\min} : \theta_{i,\max}]$ denotes the number of selected tracks in the i th inclination range, S the area of the film in analysis, Ω the solid angle, and T the exposure time ($S = 104 \text{ cm}^2$ and $T = 168 \text{ days} = 1.45 \times 10^7 \text{ sec}$ in this study).

The particle flux derived from the quartet and ECC detectors is represented in Fig.22. The ratio of the quartet flux to the ECC flux (F_Q/F_{ECC}) is shown in Fig.23. While the quartet flux is almost same with the ECC flux in the open sky, the quartet flux significantly exceeds the ECC flux in the mountain region. Specifically, the ratio of the quartet flux to the ECC flux is close to 1 in the sky region and it increases to 2 to 8 in the mountain region. Considering the different energy thresholds of the two detectors, the excess of the flux arises from the low-energy charged particles with $50 \text{ MeV} < E < 1 \text{ GeV}$. It will be confirmed in the next subsection that this excess is due to the background noise.

(a).



(b).

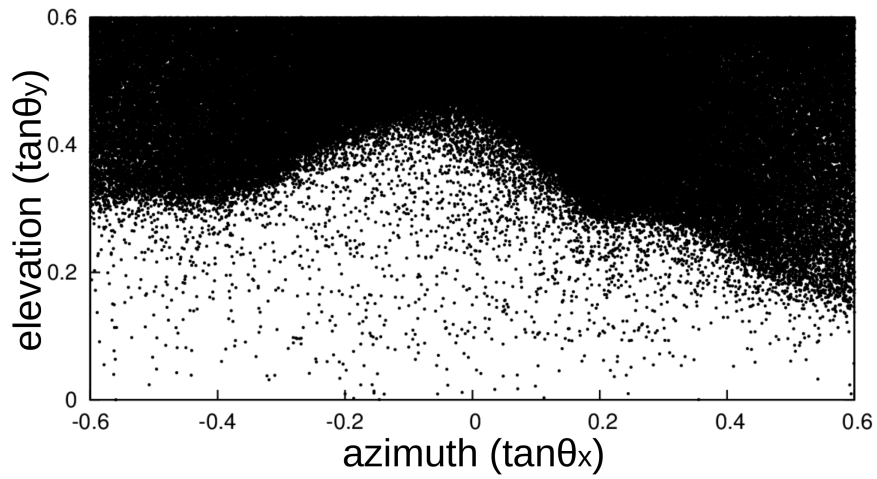


Figure 21: Angular distributions of the tracks after the selection for (a) quartet detector and (b) ECC detector.

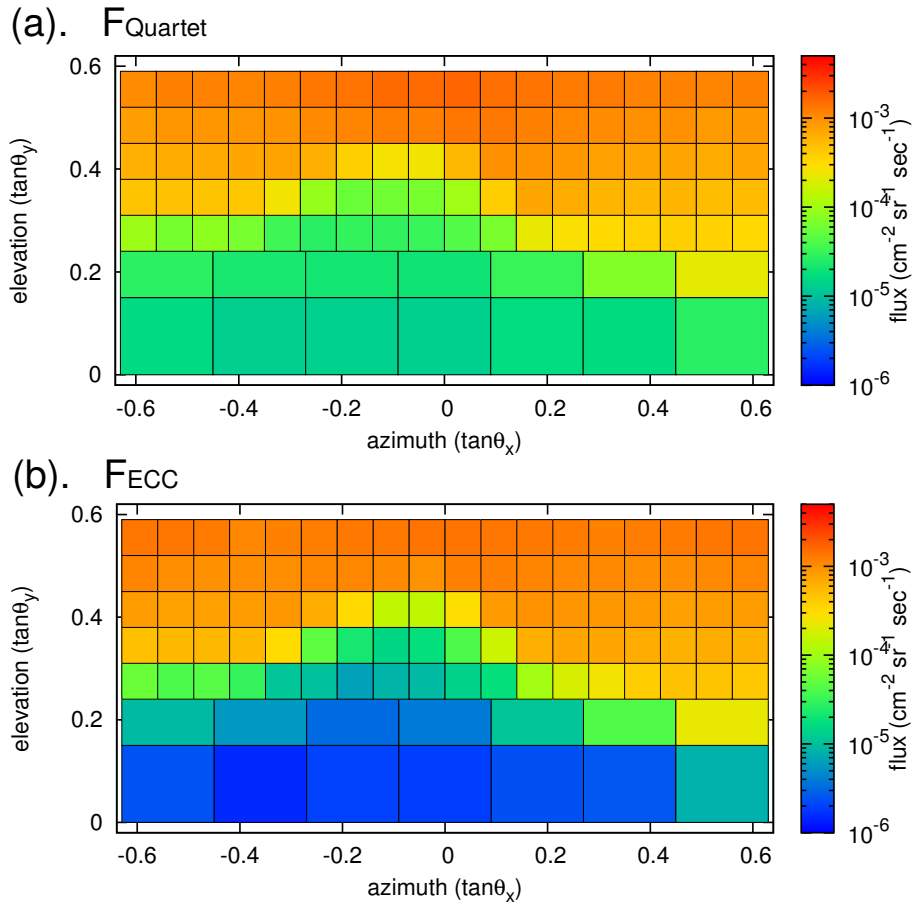


Figure 22: Particle flux derived from (a) quartet detector and (b) ECC detector.

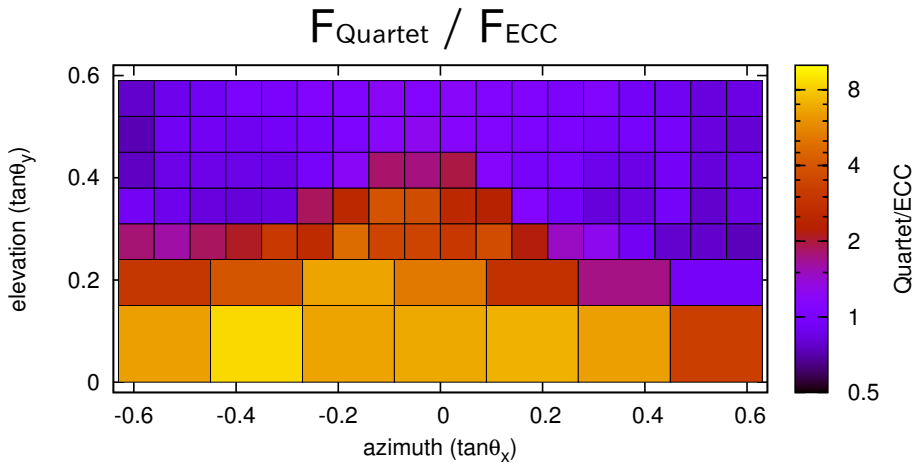


Figure 23: The ratio of the quartet particle flux to the ECC particle flux.

§ 2.6.2 Results of Muography

The observed particle flux is converted into average density by assuming that all the observed particles are penetrating muons. The conversion has taken place in the two steps. First, the theoretical values of the muon flux are calculated for a variety of topographic density ρ_{sim} . The calculation is performed by subdividing the view into small views with intervals of $[\Delta \tan \theta_x, \Delta \tan \theta_y] = [0.01, 0.01]$ and summing the integrated theoretical muon energy spectrum above the cutoff energies:

$$F^{\text{sim}} = \frac{1}{\sum_{x,y} S \cos \theta_{x,y} T \Delta \Omega_{x,y}} \left\{ \sum_{x,y} S \cos \theta_{x,y} T \Delta \Omega_{x,y} \int_{E_{\text{cut}}(X_{x,y})}^{\infty} f_{\mu}(\vartheta_{x,y}, E) dE \right\}, \quad (11)$$

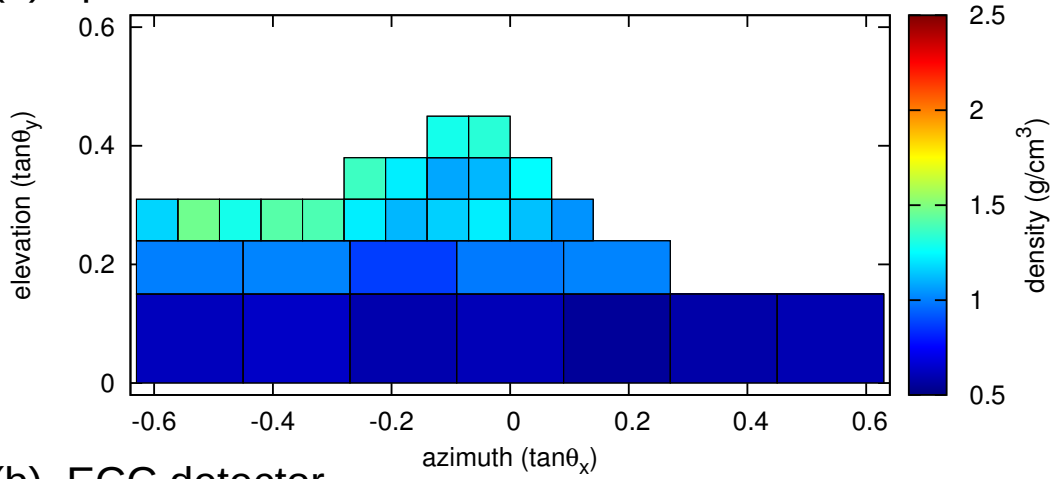
where $\Delta \Omega_{x,y}$ and $\vartheta_{x,y}$ are the solid angle and the zenith angle for the subdivided view, $X_{x,y}$ is the density-length of the rock along the radial direction in the subdivided view which is given by $X_{x,y} = \rho_{\text{sim}} \times L$ (L : thickness of rock). The L-distribution is shown in Fig. 4. The energy-cutoff E_{cut} for a given density-length is taken from Groom et al. (2001). Second, the density values along the radial directions are determined by comparing the observed flux with simulated flux (Table 4 and Table 5). The estimated density is represented in Fig.24. The density error (1σ) is represented in Fig.25. In this error, the statistical fluctuations in the number of particles and the error of efficiency are taken into account. The systematic error in density arising from the uncertainty in the muon energy spectrum is within 8 % and is almost comparable to the statistic error in the whole view (see Appendix B).

While the density values determined from the ECC detector are consistent with the density of typical volcanic rocks, the density values determined from the quartet detector are significantly lower. This fact suggests that while ECC detects only the signal muons (muons emerged from the mountain), quartet detector is affected by contamination from low-energy (< 1 GeV) charge particles other than penetrating muons.

§ 2.7 **Summary**

This experiment confirms that the source of background noise in muography is charged particles with kinetic energy of < 1 GeV. It is also demonstrated that ECC detector reduces the background noise to negligible levels and make it possible to estimate density values which agree with the typical bulk density of volcanic region. In the next section, three pieces of evidence will be presented which strongly suggest the validity of the use of ECC detector.

(a). quartet detector



(b). ECC detector

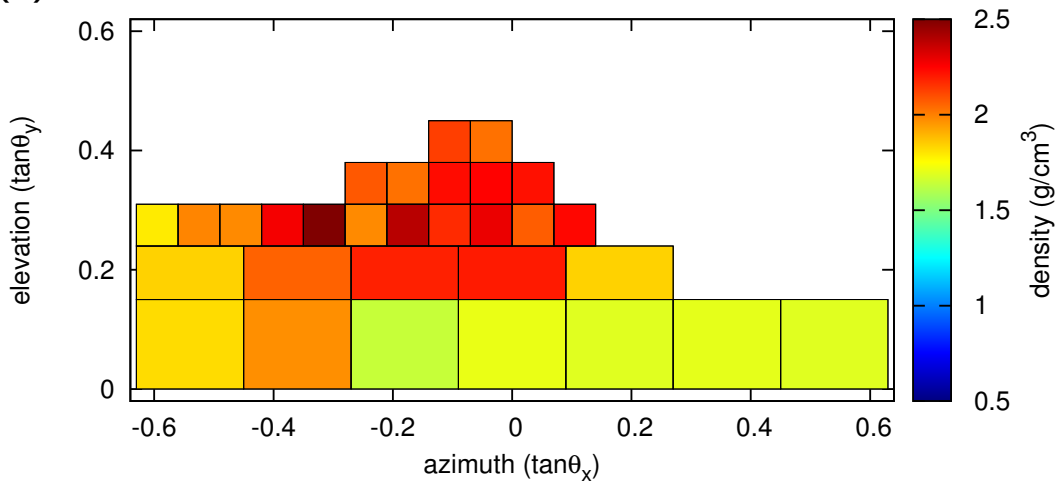
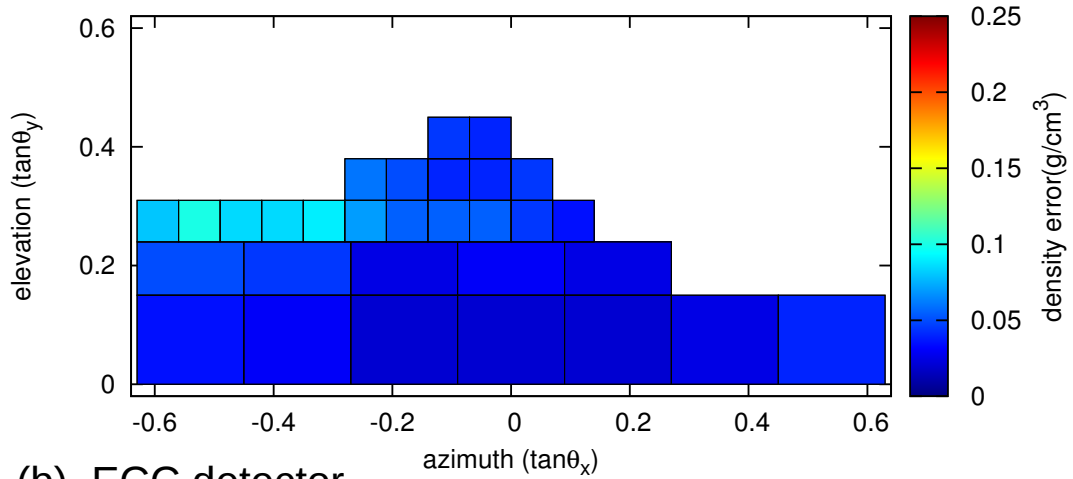


Figure 24: Average density estimated from the particle flux of (a) quartet detector and (b) ECC detector.

(a). quartet detector



(b). ECC detector

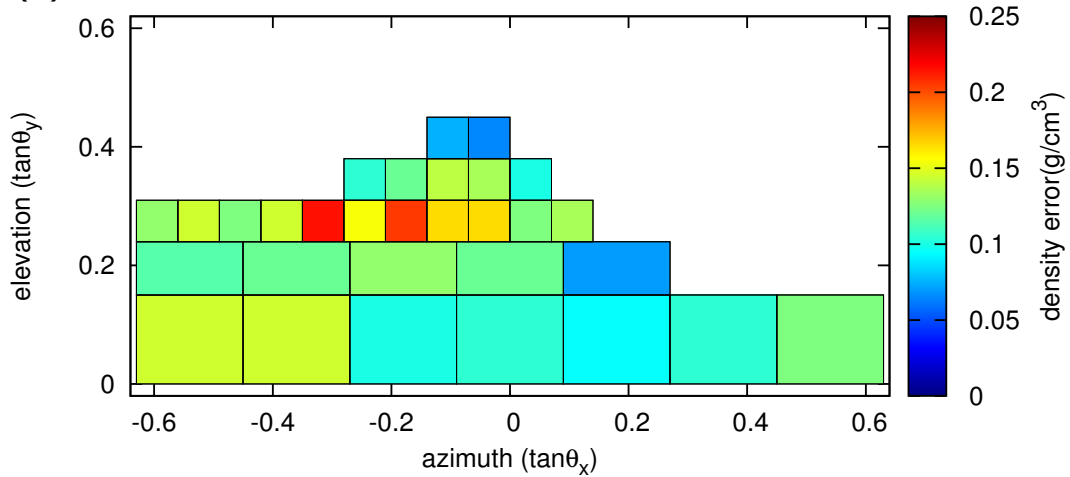


Figure 25: Error (1σ) associated with the average density of (a) quartet detector and (b) ECC detector.

$\tan \theta_x$		$\tan \theta_y$		statistics	flux ($\text{cm}^{-2}\text{s}^{-1}\text{sr}^{-1}$)		density (g/cm^3)		
min.	max.	min.	max.		flux	error (1σ)	-1σ	best	$+1\sigma$
-0.63	-0.45	0.00	0.15	132	1.60×10^{-5}	0.14×10^{-5}	0.59	0.62	0.66
-0.45	-0.27	0.00	0.15	163	1.31×10^{-5}	0.10×10^{-5}	0.61	0.64	0.67
-0.27	-0.09	0.00	0.15	310	1.35×10^{-5}	0.08×10^{-5}	0.57	0.59	0.61
-0.09	0.09	0.00	0.15	417	1.33×10^{-5}	0.07×10^{-5}	0.59	0.61	0.63
0.09	0.27	0.00	0.15	377	1.69×10^{-5}	0.09×10^{-5}	0.53	0.55	0.57
0.27	0.45	0.00	0.15	207	1.64×10^{-5}	0.12×10^{-5}	0.56	0.58	0.61
0.45	0.63	0.00	0.15	215	2.66×10^{-5}	0.18×10^{-5}	0.57	0.60	0.65
-0.63	-0.45	0.15	0.24	132	2.77×10^{-5}	0.24×10^{-5}	0.95	1.00	1.05
-0.45	-0.27	0.15	0.24	161	2.24×10^{-5}	0.18×10^{-5}	0.97	1.01	1.06
-0.27	-0.09	0.15	0.24	292	2.13×10^{-5}	0.13×10^{-5}	0.85	0.87	0.90
-0.09	0.09	0.15	0.24	377	2.00×10^{-5}	0.11×10^{-5}	0.96	0.99	1.02
0.09	0.27	0.15	0.24	423	3.15×10^{-5}	0.16×10^{-5}	0.99	1.01	1.04
-0.63	-0.56	0.24	0.31	114	9.76×10^{-5}	0.92×10^{-5}	1.10	1.17	1.26
-0.56	-0.49	0.24	0.31	93	6.39×10^{-5}	0.67×10^{-5}	1.38	1.47	1.58
-0.49	-0.42	0.24	0.31	129	8.26×10^{-5}	0.74×10^{-5}	1.21	1.29	1.38
-0.42	-0.35	0.24	0.31	116	6.40×10^{-5}	0.60×10^{-5}	1.34	1.42	1.51
-0.35	-0.28	0.24	0.31	81	3.41×10^{-5}	0.38×10^{-5}	1.32	1.40	1.50
*-0.28	-0.21	0.24	0.31	80	2.68×10^{-5}	0.30×10^{-5}	1.15	1.22	1.29
*-0.21	-0.14	0.24	0.31	107	3.01×10^{-5}	0.30×10^{-5}	1.06	1.11	1.17
*-0.14	-0.07	0.24	0.31	129	2.94×10^{-5}	0.27×10^{-5}	1.11	1.16	1.22
*-0.07	0.00	0.24	0.31	152	3.14×10^{-5}	0.26×10^{-5}	1.17	1.22	1.28
*0.00	0.07	0.24	0.31	206	4.27×10^{-5}	0.31×10^{-5}	1.09	1.13	1.18
*0.07	0.14	0.24	0.31	285	6.58×10^{-5}	0.42×10^{-5}	1.01	1.04	1.08
*-0.28	-0.21	0.31	0.38	226	9.03×10^{-5}	0.61×10^{-5}	1.31	1.37	1.43
*-0.21	-0.14	0.31	0.38	165	5.48×10^{-5}	0.43×10^{-5}	1.17	1.22	1.27
*-0.14	-0.07	0.31	0.38	205	5.99×10^{-5}	0.44×10^{-5}	1.04	1.08	1.12
*-0.07	0.00	0.31	0.38	246	6.52×10^{-5}	0.44×10^{-5}	1.07	1.11	1.15
*0.00	0.07	0.31	0.38	378	1.02×10^{-4}	0.06×10^{-4}	1.21	1.25	1.30
*-0.14	-0.07	0.38	0.45	693	2.60×10^{-4}	0.11×10^{-4}	1.24	1.29	1.33
*-0.07	0.00	0.38	0.45	711	2.48×10^{-4}	0.10×10^{-4}	1.29	1.33	1.37

Table 4: Results of muography with quartet detector. The rows with asterisks correspond to the regions where the lava dome is exposed on the surface.

$\tan \theta_x$		$\tan \theta_y$		statistics	flux ($\text{cm}^{-2}\text{s}^{-1}\text{sr}^{-1}$)		density (g/cm^3)		
min.	max.	min.	max.		flux	error (1σ)	-1σ	best	$+1\sigma$
-0.63	-0.45	0.00	0.15	29	2.46×10^{-6}	0.46×10^{-6}	1.69	1.82	1.98
-0.45	-0.27	0.00	0.15	29	1.52×10^{-6}	0.29×10^{-6}	1.84	1.97	2.13
-0.27	-0.09	0.00	0.15	54	2.04×10^{-6}	0.29×10^{-6}	1.55	1.64	1.75
-0.09	0.09	0.00	0.15	55	1.95×10^{-6}	0.29×10^{-6}	1.62	1.71	1.83
0.09	0.27	0.00	0.15	63	2.38×10^{-6}	0.31×10^{-6}	1.60	1.69	1.79
0.27	0.45	0.00	0.15	48	2.53×10^{-6}	0.37×10^{-6}	1.61	1.70	1.82
0.45	0.63	0.00	0.15	91	8.09×10^{-6}	0.85×10^{-6}	1.57	1.69	1.82
-0.63	-0.45	0.15	0.24	60	9.21×10^{-6}	1.20×10^{-6}	1.73	1.84	1.96
-0.45	-0.27	0.15	0.24	56	5.61×10^{-6}	0.75×10^{-6}	1.95	2.06	2.19
-0.27	-0.09	0.15	0.24	47	3.21×10^{-6}	0.47×10^{-6}	2.07	2.19	2.33
-0.09	0.09	0.15	0.24	62	3.88×10^{-6}	0.52×10^{-6}	2.09	2.20	2.33
0.09	0.27	0.15	0.24	160	1.10×10^{-5}	0.08×10^{-5}	1.77	1.84	1.91
-0.63	-0.56	0.24	0.31	79	5.45×10^{-5}	0.62×10^{-5}	1.67	1.79	1.93
-0.56	-0.49	0.24	0.31	72	4.00×10^{-5}	0.47×10^{-5}	1.86	1.99	2.15
-0.49	-0.42	0.24	0.31	100	4.43×10^{-5}	0.44×10^{-5}	1.86	1.98	2.11
-0.42	-0.35	0.24	0.31	80	3.06×10^{-5}	0.34×10^{-5}	2.14	2.27	2.43
-0.35	-0.28	0.24	0.31	32	1.11×10^{-5}	0.20×10^{-5}	2.35	2.54	2.78
*-0.28	-0.21	0.24	0.31	35	1.02×10^{-5}	0.17×10^{-5}	1.85	1.98	2.16
*-0.21	-0.14	0.24	0.31	25	6.36×10^{-6}	1.27×10^{-6}	2.21	2.39	2.62
*-0.14	-0.07	0.24	0.31	36	8.53×10^{-6}	1.42×10^{-6}	2.02	2.17	2.35
*-0.07	0.00	0.24	0.31	40	9.14×10^{-6}	1.45×10^{-6}	2.14	2.29	2.47
*0.00	0.07	0.24	0.31	62	1.41×10^{-5}	0.18×10^{-5}	1.96	2.07	2.21
*0.07	0.14	0.24	0.31	75	1.78×10^{-5}	0.21×10^{-5}	2.12	2.24	2.39
*-0.28	-0.21	0.31	0.38	138	4.82×10^{-5}	0.41×10^{-5}	1.98	2.08	2.19
*-0.21	-0.14	0.31	0.38	68	2.16×10^{-5}	0.26×10^{-5}	1.92	2.03	2.16
*-0.14	-0.07	0.31	0.38	54	1.53×10^{-5}	0.21×10^{-5}	2.11	2.23	2.39
*-0.07	0.00	0.31	0.38	64	1.77×10^{-5}	0.22×10^{-5}	2.13	2.25	2.40
*0.00	0.07	0.31	0.38	146	4.03×10^{-5}	0.34×10^{-5}	2.13	2.22	2.33
*-0.14	-0.07	0.38	0.45	405	1.43×10^{-4}	0.07×10^{-4}	2.06	2.13	2.21
*0.07	0.00	0.38	0.45	417	1.42×10^{-4}	0.07×10^{-4}	1.97	2.03	2.10

Table 5: Results of muography with ECC detector. The rows with asterisks correspond to the regions where the lava dome is exposed on the surface.

§ 3 Supporting Evidence

In the previous section, it is demonstrated that ECC detector reduces background noise to negligible levels and succeeded in density estimation without underestimation which was seen in quartet detector. This section proposes supporting evidence for that. Three pieces of evidence are presented. First, the muography results of ECC detector are consistent with the density of sampled rocks (§ 3.1). Second, the muography results of ECC detector are consistent with other geophysical observations. To be concrete, I determined the three-dimensional density profile of Showa-Shinzan by inverting the ECC muography results and gravity anomaly data. The reconstructed density profile agrees with geomagnetic and resistivity models by prior works in terms of the shape of the lava. Third, the particle fluxes derived from quartet and ECC detectors are compared with the numerical simulation in § 3.3.

§ 3.1 Evidence 1: Comparison with Rock Sample

ECC detector measures the bulk density of Showa-Shinzan (SS) lava to range between 1.98–2.39 g/cm³. The density error at each point is 0.07–0.23 g/cm³ (see Table 5). By contrast, the prior muography work at the same site by Tanaka et al. (2007b) yields 2.71 – 2.91 g/cm³ with the density error of 0.17 g/cm³ at each data point.

SS lava is classified to dacite from SiO₂ content of rock samples (69.74 wt%; Nemoto et al., 1957). According to this work, the bulk density of

SS lava is 2.32 g/cm^3 . The prior muography work exceeds significantly the sampled density. On the other hand, ECC densities agree well with the sample bulk density. This supports improved accuracy of ECC muography compared with the prior work.

§ 3.2 Evidence 2: Comparison with Gravity Data

The muography results of ECC detector and the prior work (Tanaka et al., 2007b) are compared with gravity data at thirty stations on/around the lava dome. To be concrete, muography data and gravity data are combinedly used to solve 3-D density profile of the lava dome. The details of the method and data processing are given in Appendix C. The results using the prior muography work and gravity data have already been published in Nishiyama et al. (2014b).

Fig.26 represents horizontal sectional views of the 3-D density model determined from (a) ECC muography + gravity data (Model A) and (b) prior muography work + gravity data (Model B). The two models agree in the general characteristics of this mountain. To be concrete, the western part of the mountain, where the dome exists, has a higher density ($> 2.0 \text{ g/cm}^3$) than the eastern part of the mountain ($< 2.0 \text{ g/cm}^3$), where the uplifted plateau exists.

However, there are significant difference in detail of the density structures inside the lava dome. Fig.27 represents vertical sectional views of the two models. Model A presents an existence of a cylindrical block of massive

lava (AH; $2.0 < \rho < 2.4 \text{ g/cm}^3$) with diameter of 300 m in the center of the dome. On the other hand, Model B suggests that high density is localized in two regions. One is in the north of the mountain at 220 m asl (BH1; $2.4 < \rho < 2.6 \text{ g/cm}^3$) and the other is in the south of the mountain at 300 – 340 m asl (BH2; $2.6 < \rho < 3.0 \text{ g/cm}^3$). The density values of BH2 region are apparently inconsistent with the sampled density of SS lava, as discussed in § 3.1. This excess is caused by too high average density estimated from the prior work with conventional emulsion methods.

Other geophysical observations also support Model A. For instance, a magnetism model derived from the geomagnetic observation (Nishida and Miyajima, 1984) suggests vertical extension of lava. This prior work concludes that the root of the lava dome has almost the same diameter as that of the dome exposed on the surface (I would suggest 300 m). An electrical resistivity model derived from the magnetotelluric survey (Goto and Johmori, 2014) suggests subspherical shape of dacite intrusion beneath the dome, whose diameter is ~ 400 m. Model A agrees with these geophysical models in terms of the shape of lava. On the other hand, Model B suggests that horizontal migration of lava might occur at around 300 m asl. This feature is difficult to explain by other geological or geophysical evidence.

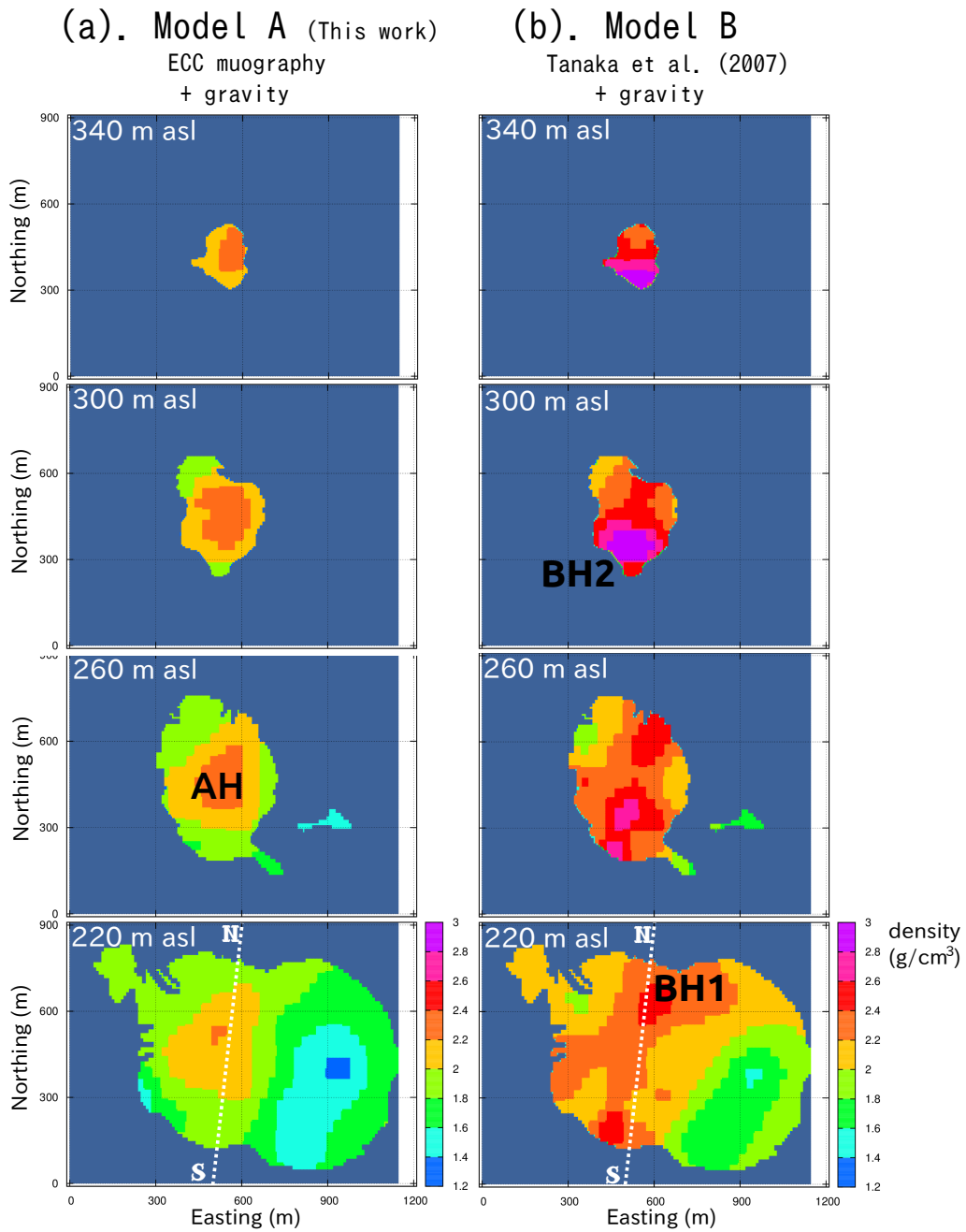


Figure 26: (a) Horizontal sectional views of 3-D density model determined from a joint inversion of the result of ECC muography and the gravity data (Model A in the text). (b) 3-D density model determined from a joint inversion of the prior muography work and the gravity data (Model B).

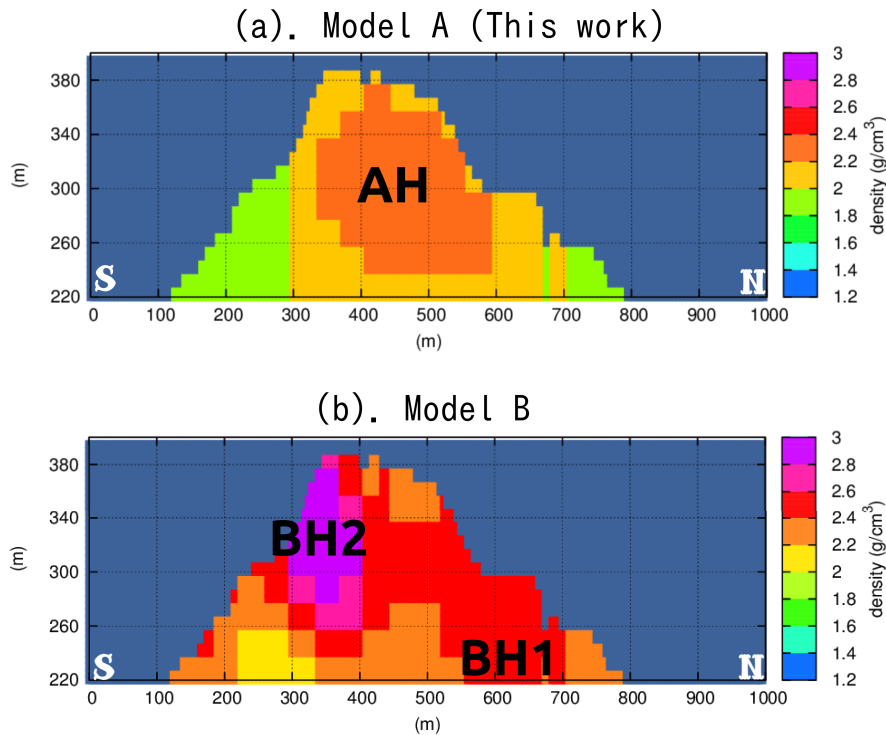


Figure 27: Vertical sectional views of Model A and Model B along the line SN in Fig.26.

§ 3.3 Evidence 3: Comparison with Numerical Simulation

In § 2.6, the particle fluxes are obtained independently from quartet detector and ECC detector. The two detectors have different energy thresholds as shown in Table 3. The quartet flux almost agrees with the ECC flux in the open sky. However, the quartet flux exceeds the ECC flux by a factor of 2 to 8 in the mountain region. As a result, quartet detector suffer from underestimation of density when inverting the flux into the density. This difference of flux can be explained by numerical simulation. This subsection

provides the results of the numerical simulation. The details of the simulation are given in Appendix D.

This paragraph describes an overview of the simulation. In this simulation, a rotational-symmetric shape of mountain is constructed in a computational region (Fig.28a). The shape of the mountain imitates the topography of Showa-Shinzan. A virtual detector is placed at 500 m away from the summit. A large spheroidal hemisphere enclosing the mountain and the detector is constructed. From the hemisphere, 2 billion muons, 0.5 billion electromagnetic particles (electrons, positrons and photons), and 0.5 billion hadronic particles (protons and neutrons) are injected. These numbers correspond to the numbers of particles falling down onto the hemisphere in 15 secs. To get better statistics, the size of the virtual detector is set to $3 \times 10^4 \text{ m}^2$. Since the size of the ECC detector is 0.01 m^2 , the equivalent exposure time of this simulation is $4.5 \times 10^7 (= 1.5 \text{ yr})$.

Fig.28b represents the angular distribution of charged particles arriving at the virtual detector. These particles can be classified into four components: (i) signal muons; (ii) protons; (iii) muons and electrons produced from the hadronic interaction; (iv) electrons from electromagnetic showers. For quantitative discussion, two angular domains are defined: domain A (sky) [$0.45 \leq \cos \theta < 0.52$]; domain B (mountain) [$0 \leq \cos \theta < 0.18$]. Fig.29 represents the integrated energy spectrum for each domain.

In the domain A, signal muons are dominant for all the energy thresholds. The integrated intensity of signal muons is almost flat below $\sim 1 \text{ GeV}$, This

result explains why there is no significant difference in quartet and ECC flux of the sky region. On the other hand, in the domain B, the intensity of non-signal components (ii,iii,iv) exceed the flux of signal muons at low energy threshold. These non-signal components become negligible above 1 GeV. This result clearly explains the excess of particle flux derived from the quartet detector in the mountain region.

This paragraph provides the calculated intensity of non-signal components above 50 MeV in the domain B. The proton flux is $9 \times 10^{-2} [\text{m}^{-2}\text{sec}^{-1}\text{sr}^{-1}]$. 40% of the flux is the flux of protons which travel upward from the rear of the detector (upward-going particles). The flux of muons and electrons produced by hadrons is $5 \times 10^{-2} [\text{m}^{-2}\text{sec}^{-1}\text{sr}^{-1}]$. 30% of this value is the flux of upward-going particles. The flux of electrons from electromagnetic shower is $2 \times 10^{-2} [\text{m}^{-2}\text{sec}^{-1}\text{sr}^{-1}]$. 90% of the value is the flux of upward-going electrons.

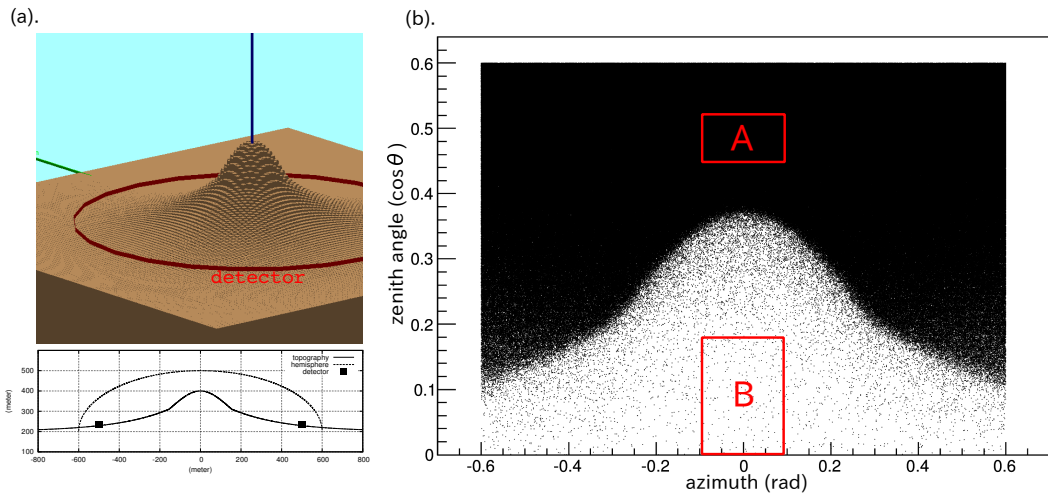


Figure 28: (a) Virtual mountain and detector constructed in a computational region of GEANT4 toolkit with dimensions given in the lower figure. (b) Angular distribution of particles arriving at the virtual detector with domains A and B indicated with red rectangles.

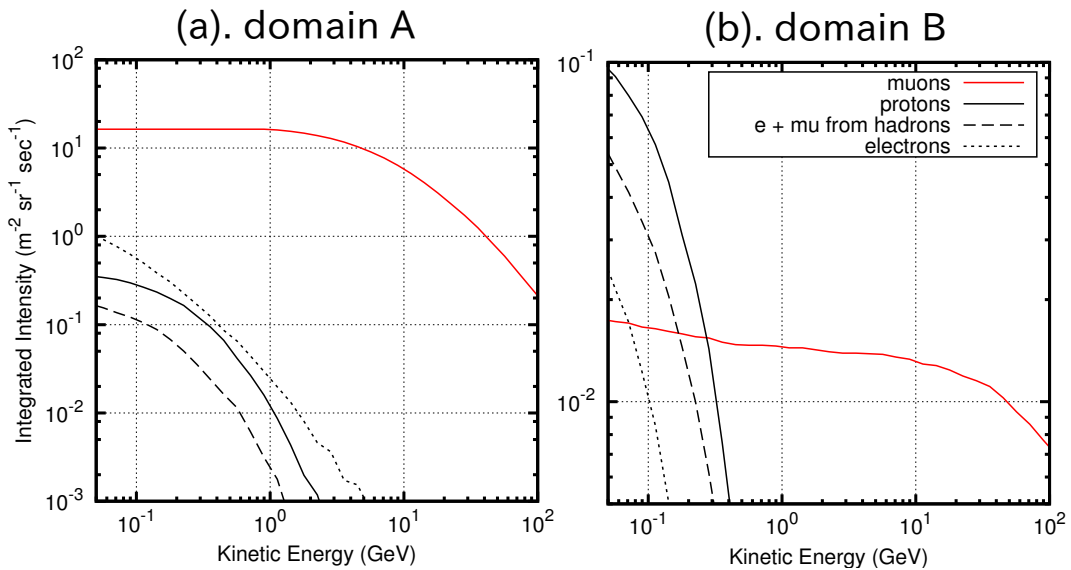


Figure 29: Calculated energy spectra of particles in domain A and B. The vertical axis is the integrated intensity above the energy threshold given in the horizontal axis.

§ 3.4 Summary

This study proposes the use of the ECC detector to reduce the background noise and to achieve accurate muographic density estimation. In this section, three pieces of evidence are presented to support the performance of ECC detector.

Firstly, the density derived from ECC detector agrees with the density measured from rock samples. On the other hand, the prior work with conventional methods does not agree with the density of rock samples.

Secondly, the 3-D density model derived from ECC muographic results and gravity data (Model A) agrees with the density of sampled rocks and other geophysical models. Yet in the 3-D density model derived from the prior muographic results and gravity data (Model B), the lava density is determined to be too high and the shape of the massive lava does not agree with other geophysical models.

The last evidence is given by the numerical simulation. The results of the simulation suggest that detectors having low energy thresholds suffer from the contamination of low-energy background particles such as protons, muons and electrons produced from hadrons, and electrons from EM-shower. Only detectors having high energy thresholds (> 1 GeV) can measure the precise flux of muons which penetrated the target. This result strongly supports the validity of the use of ECC detector.

§ 4 Discussion

§ 4.1 Background Noise

In this work, the excess of the particle flux in the quartet detector is explained by the results of the numerical simulation (see § 3.3). The amount of the excess is

$$\begin{aligned}
 &1.1 \times 10^{-5} \text{ cm}^{-2} \text{ sec}^{-1} \text{ sr}^{-1} (0 < \tan \theta_y < 0.15), \\
 &1.6 \times 10^{-5} \text{ cm}^{-2} \text{ sec}^{-1} \text{ sr}^{-1} (0.15 < \tan \theta_y < 0.24), \\
 &1.7 \times 10^{-5} \text{ cm}^{-2} \text{ sec}^{-1} \text{ sr}^{-1} (0.24 < \tan \theta_y < 0.31).
 \end{aligned} \tag{12}$$

On the other hand, the flux of true muon signals observed by ECC detector is

$$\begin{aligned}
 &1.9 \times 10^{-6} \text{ cm}^{-2} \text{ sec}^{-1} \text{ sr}^{-1} (0 < \tan \theta_y < 0.15), \\
 &3.9 \times 10^{-6} \text{ cm}^{-2} \text{ sec}^{-1} \text{ sr}^{-1} (0.15 < \tan \theta_y < 0.24), \\
 &1.4 \times 10^{-5} \text{ cm}^{-2} \text{ sec}^{-1} \text{ sr}^{-1} (0.24 < \tan \theta_y < 0.31).
 \end{aligned} \tag{13}$$

From the numerical simulation, it is concluded that the origin of these excesses is due to protons, muons and electrons produced by hadronic interaction, and electrons from EM shower. These backgrounds include particles traveling upward from the rear of the detector. Later herein, this conclusion is discussed with other prior works.

Tanaka et al. (2007b) has performed a muography observation at the same target (Showa-Shinzan) with emulsion detectors. Since the detector used in

this observation consists of a stack of four emulsion films. the performance of the background reduction must be almost the same with that of the quartet detector. Thus, this observation suffered from background noise caused by low-energy charged particles. To avoid underestimation of density, this prior work performed background subtraction from observed particle flux as in the same way of Okubo and Tanaka (2012). To be concrete, the noise level was estimated from the flux of nearly horizontal directions and it was subtracted from the observed fluxes in other directions. However, it should be noted that the background level depends on direction of incident particles as seen in Eq. (12). Thus the assumption that the flux of the background particles is isotropic is invalid.

I have to mention that this prior work overestimates the bulk density of Showa-Shinzan as discussed in §3.1. This is inconsistent with the above discussion. The subtraction of the uniform background level should have yielded still lower density than the actual bulk density. The reason of the overestimation must be attributed to the fact that the angular dependence of the efficiency has not been considered properly. In the prior work, the efficiency of the detector was assumed to be uniform in the view. However, the actual efficiency should have depended strongly on the inclination θ (see Fig.17). If we take the values of the quartet detector, it has high efficiency in the center of the view ($\epsilon \sim 80\%$ at $\theta = 0$) and it decreases to $\epsilon \sim 40\%$ at $\theta = 0.3$, where the too high lava density ($> 2.7 \text{ g/cm}^3$) was found. If we mistakenly believe that the efficiency is constant to be $\sim 80\%$ in the whole

view, we underestimate the particle flux of the region of the lava by a factor of 2 and thus overestimates density of the lava. Thus I conclude that the overestimation of density in the prior work is due to the invalid assumptions on the uniform background level and the uniform efficiency. Contrary to the drawbacks of the prior work, the greatest advantage of the use of ECC detector is that it can measure the precise flux of signal muons without artificial assumptions with the aid of background reduction and precise efficiency correction.

Carbone et al. (2014) has observed an excess of the particle flux by a factor of 2 to 10 from the mountain region. This measurement was performed at Mt. Etna (~ 3000 masl) by using a scintillation detector. Although the type of the detector and the altitude are different, the ratio of noise to signal is consistent with my study. To avoid underestimation of density, Carbone et al. (2014) made a model of the angular distributions of noise flux by a linear regression analysis and subtracted the model flux from the observed flux. They admit that it is not feasible to use the flux after subtraction for quantitative density estimation. It should be again emphasized that the use of ECC detector does not require background model or subtraction which cause systematic uncertainty in density estimation.

Jourde et al. (2013) has proposed a pioneering discussion on the source of background noise. They detected upward-going particles by a dedicated time-of-flight (TOF) analysis with scintillation detectors. The upward-going particles enter the back side of the detector with trajectories identical to

those of muons emerging from the target. This prior work suggests that upward-going particles cause significant density error on muography and that the upward-going particles are likely to be muons and high-energy electrons produced in the atmosphere volume located below the telescope level. The results of my simulation agree with this prior work in the existence of upward-going particles. The integrated intensities of upward-going particles above 50 MeV are $3.4 \times 10^{-2} \text{ m}^{-2}\text{sec}^{-1}\text{sr}^{-1}$ for protons, $1 \times 10^{-2} \text{ m}^{-2}\text{sec}^{-1}\text{sr}^{-1}$ for muons produced from hadrons, $5 \times 10^{-3} \text{ m}^{-2}\text{sec}^{-1}\text{sr}^{-1}$ for electrons produced from hadrons, and $1.9 \times 10^{-2} \text{ m}^{-2}\text{sec}^{-1}\text{sr}^{-1}$ for electrons from EM-showers. My simulation suggests the major component of the upward-going particles are protons and electrons from EM-showers. However, the upward-going particles cannot explain the excess of the quartet flux alone. It should be noted that the noise particles come not only from the back side of the detector but also from the front side, according to my simulation.

§ 4.2 Geoscientific Implications

This subsection discusses geoscientific implication of Showa-Shinzan (SS) from the 3-D density model derived from ECC muographic results and gravity data (Model A in Fig.26). The model presents the two features of Showa-Shinzan. Firstly, SS dome consists of cylindrical shape of massive lava ($2.0 < \rho < 2.4 \text{ g/cm}^3$) with a diameter of 300 m. Secondly, there is no dacite intrusion beneath the uplifted plateau. In the following two paragraphs, these features are discussed compared with other prior works.

Nemoto et al. (1957) has performed gravity measurements on/around the lava dome. They have detected 1 mGal positive Bouguer anomaly at the top of the dome due to the massive lava. However, they could not interpret it into the shape of the lava because of the non-uniqueness in gravity interpretation (see Zidarov, 1990). My study succeeded in three-dimensional interpretation by combining muographic measurements. The shape of the dacite intrusion derived from my study agrees very well with a magnetic model proposed by Nishida and Miyajima (1984) and an electrical resistivity model proposed by Goto and Johmori (2014).

It has been controversial whether there is a dacite intrusion beneath the uplifted plateau (so called Yaneyama in Japanese). Nakamura and Mori (1949) has proposed the existence of the intrusive lava beneath the plateau from laboratory experiments. Nemoto et al. (1957) reports the existence of a small positive Bouguer anomaly probably caused by intrusive lava on the east of the plateau. On the other hand, the resistivity model (Goto and Johmori, 2014) proposes an absence of the intrusion below the plateau, because below the plateau is characterized by low resistivity. They proposed that the plateau is formed by uplift and lateral migration of pre-existing rocks and sediments. In my 3-D density model, the uplifted plateau is characterized by low density ($1.3 < \rho < 1.7 \text{ g/cm}^3$). There is no significant high density part found in the plateau within our target region ($> 200 \text{ masl}$). In this sense, our 3-D density model supports the theory of Goto and Johmori (2014). To discuss deeper parts of the plateau, additional muographic observations are

required.

§ 4.3 Future Prospects

As this work has demonstrated, the use of ECC detector is essential for accurate muographic imaging. Nowadays, the use of ECC detector spreads to other muography groups. For instance, ECC detector was adopted in the project for detection of landslide faults at La Palma, Canary Islands, Spain.

This work has established a standard method for muography analysis with nuclear emulsions. The remaining task is to establish a large scale detector ($> 10 \text{ m}^2$). The large scale exposure will enable faster muography of Showa-Shinzan size volcanoes ($\sim 1 \text{ km}$). For instance, in this work it took 5 months to take a muographic image of Showa-Shinzan with 0.01 m^2 detector. If 10 m^2 detectors become available, the exposure will finish in less than a day. Moreover, large detectors will enable muography of geophysical targets larger than Showa-Shinzan.

For large scale exposure, the production of nuclear emulsions are underway by F-lab, Nagoya University (Morishima et al., 2014). The production of fresh emulsions will also help us reduce the number of emulsion films used in the ECC detector. As discussed in § 2.5, the efficiency of the OPERA film is now lowered to be $60 \sim 80 \%$ because of aged deterioration. Thus twenty films were necessary for ECC detector to get enough statistics of deflection angles. If the efficiency of the new emulsions is nearly 100% , the number of the films can be reduced to 10. This will reduce the time for scanning and

post-processing and will enable faster muographic analysis.

The development of faster readout modules are necessary for large scale exposure. A group of Salerno University has upgraded the optics and the image processing of the ESS and succeeded in six times faster scanning (Quick Scanning System, 120 cm²/h, Bozza et al., 2013). Researchers in F-lab of Nagoya University are developing a much faster scanning system with a large objective lens and GPGPU based image processing (Hyper Track Selector, Yoshimoto et al., 2014). The maximum scanning speed of HTS will be 9000 cm²/h.

§ 5 Conclusion

To conclude I have established a standard method for accurate muographic imaging of volcanoes with Emulsion Cloud Chamber (ECC). I performed a test experiment at Showa-Shinzan Lava Dome, Usu, Japan, with a prototype of ECC detector. I have developed a method of track selection and efficiency correction for ECC detector. As a result, the particle flux measured by ECC detector was lowered to be half to one-eighth of the flux measured by conventional emulsion detectors. Consequently, the densities measured by ECC detector agree well with the bulk density of the sampled rocks at Showa-Shinzan.

The muographic results of ECC detector were combinedly used with gravity anomaly data to determine the three-dimensional density profiles of Showa-Shinzan. As a result, it was found that that Showa-Shinzan consists of the high-density dome ($\rho > 2.0 \text{ g/cm}^3$) and the low-density uplifted plateau ($\rho < 2.0 \text{ g/cm}^3$) and that the dome is made of a cylindrical shape of massive lava ($2.0 < \rho < 2.4 \text{ g/cm}^3$) with a diameter of 300 m. The 3-D density model agrees well with other geophysical models in the shape of the lava.

I have performed a numerical simulation to understand the origin of the background noise in muography. I have confirmed that the excess of the particle flux observed by conventional emulsion detectors is due to low-energy charged particles ($< 1 \text{ GeV}$) which consist mainly of protons, muons and

electrons produced by the hadronic interaction and electrons from electromagnetic showers. These noise particles contain upward-going particles.

Appendices

A Volcanological Backgrounds of Showa-Shinzan

Showa-Shinzan Lava Dome was extruded as a parasitic cone of Usu Volcano in a wheat field. The eruption activity commenced with volcanic earthquakes at the eastern foot of Usu in December 1943, which was followed by upheaval of the ground at approximately 1 km south of the present dome. The center of the uplifted area shifted 1 km northward in April 1944, and a plateau was formed. In October 1944, paroxysmal explosions occurred at seven craters which newly opened on the plateau. Finally, lava extruded from below the plateau to form the dome in November 1944 and significant uplifted ended in October 1945 (Minakami et al., 1951). The morphological growth of the dome was recorded by Mimatsu (1962).

Showa-Shinzan lava dome is classified as a dacite cryptodome, where the dacite lava is thickly covered by overlying sediments. The new lava forming the dome is not visible except for some eroded parts (Goto et al., 2004). Thus, little has been known on the overall shape of the lava from visual inspection. After the eruption, a number of scientists have looked for evidence of intrusive lava below the dome by gravity (Nemoto et al., 1957), seismic (Nemoto et al., 1957; Miyauchi et al., 1987), geomagnetic (Nemoto et al., 1957; Nishida and Miyajima, 1984) and electrical resistivity (Goto and Johmori, 2014) surveys.

B Principle of Muography

Muography is based on measurements of absorption of cosmic-ray muons inside target material. Since energy spectrum of cosmic-ray muons and energy dependence of muon range have been intensively investigated, the attenuation of muon flux can be used to derive the amount of matter present along muon trajectories. This section describes details of these topics.

B.1 Energy Spectrum of Cosmic-ray Muons

The muon is a leptonic elementary particle. It is similar to electrons, and the mass of the muon is 206.5 times of that of electron: $m_\mu = 105.6 \text{ MeV}/c^2$ and $m_e = 0.511 \text{ MeV}/c^2$. The muons were discovered and identified in tracks of cosmic rays inside a cloud chamber by Anderson in 1932. The cosmic-ray muons are plausible to be used as a source of radiographic inspection of gigantic objects, because they have extremely high penetration power compared with other charged particles.

Cosmic-ray muons are the most numerous charged particles at sea level. They are produced high in the atmosphere (typically 15 km) by the decay of charged meson (pions and kaons). The energy and angular distribution of muons reflect a convolution of their production spectrum, energy loss in the atmosphere and decay (Beringer et al., 2012). The intensity of vertical muons above 1 GeV at sea level is $\sim 70 \text{ m}^{-2}\text{s}^{-1}\text{sr}^{-1}$. The energy spectra of nearly horizontal muons were intensively studied, for instance, by the DEIS

(Allkofer et al., 1985) experiments in 1980s. In this study, the energy spectra of muons calculated by Honda et al. (2011) is used (Fig.30).

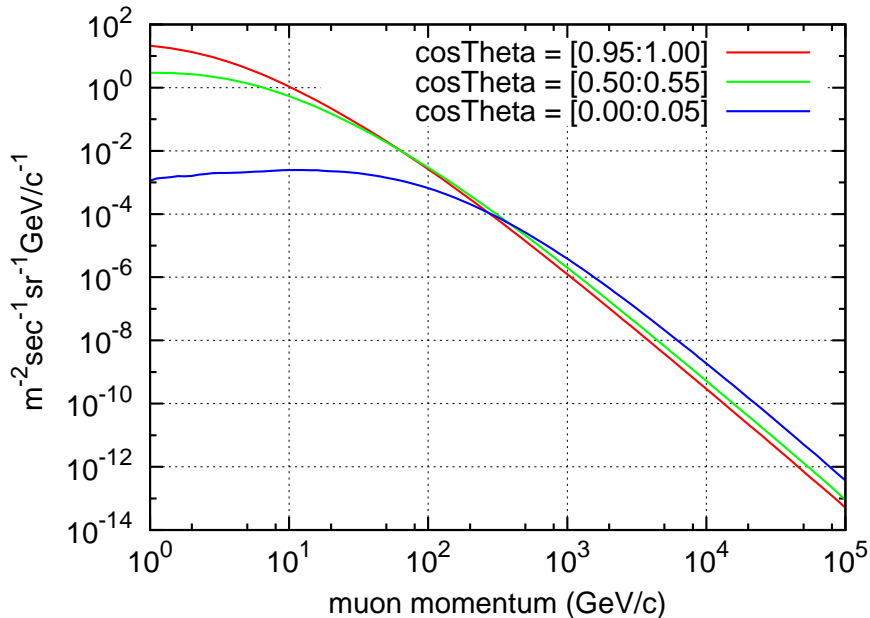


Figure 30: Differential muon spectra of three zenith angle ranges, calculated by M. Honda (Honda et al., 2011).

B.2 Muon Range in Rock

Muons lose energy by ionization and radiative processes: bremsstrahlung, direct production of e^+e^- pairs, and photonuclear interactions. The total muon energy loss is given as a function of the amount of matter traversed as

$$-\frac{dE_\mu}{dX} = a + bE_\mu, \quad (14)$$

where a is the ionization loss and b is the fractional energy loss by the three radiative processes (Beringer et al., 2012). a and b are slowly varying as a function of energy. The quantity $\epsilon = a/b$ (~ 693 GeV in standard rock) defines a critical energy above which radiative process becomes more dominant

than ionization loss. The values of a and b and their energy dependence for various materials are tabulated in Groom et al. (2001).

Integration of Eq. (14) gives the range which muons can penetrate inside rock as

$$R(E) = \int_{E_0}^E [a(E') + b(E')E']^{-1} dE', \quad (15)$$

where E_0 is sufficiently small that the result is insensitive to its exact value. This range is called as continuous-slowing-down-approximation (CSDA) range and is tabulated in Groom et al. (2001). Fig.31 shows the muon CSDA range for standard rock. The range is almost proportional to energy below critical energy (693 GeV), because muon energy loss is continuous in this energy range. It becomes gradually flat above the critical energy above which radiative process becomes dominant.

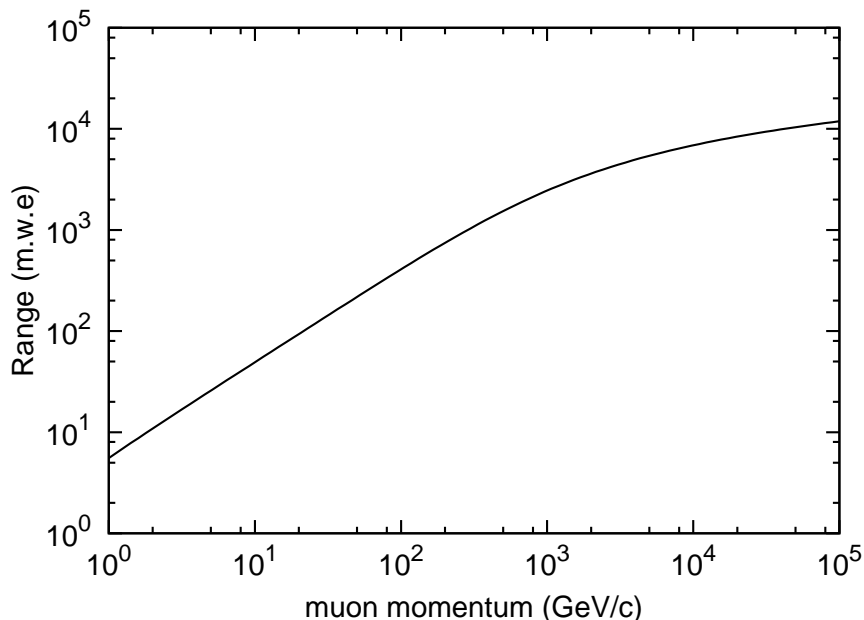


Figure 31: Muon range as a function of momentum in standard rock, interpolated from the data reported in Groom et al. (2001).

B.3 Integrated Muon Flux

The flux of muons after passing through a certain amount of rock is given by integrating the muon energy spectra above the corresponding energy:

$$I(R) = \int_{E(R)}^{\infty} f(E')dE', \quad (16)$$

where $E(R)$ is an inverse function of Eq. (15) and $f(E')$ is the differential energy spectrum. Fig.32 shows the integrated flux as a function of the amount of matter for vertical (red), $\theta \sim 60^\circ$ (green), and quasi-horizontal muons (blue). While the vertical muons are dominant at small thickness, the quasi-horizontal flux exceed the vertical flux at $R > 1000$ m.w.e. (meter water equivalent). This is because horizontal muons are generally energetic than vertical ones.

A muographic measurement gives the number of muons (N_{obs}) arriving at a detector during certain exposure time. The muon intensity is obtained after efficiency correction and normalization with detection area S , solid angle Ω and exposure duration T :

$$I_{\text{obs}} = \frac{\epsilon^{-1}N_{\text{obs}}}{S\Omega T}, \quad (17)$$

where ϵ is a detection efficiency. Once I_{obs} is obtained, the range (R) is then estimated by inverting Eq. (16). In this thesis, the range R is called as density-length and is represented by X . In other literatures (eg. Lesparre et al., 2010) it is called as opacity. The average density along the muon trajectory is obtained by dividing the density-length by the path length of muons.

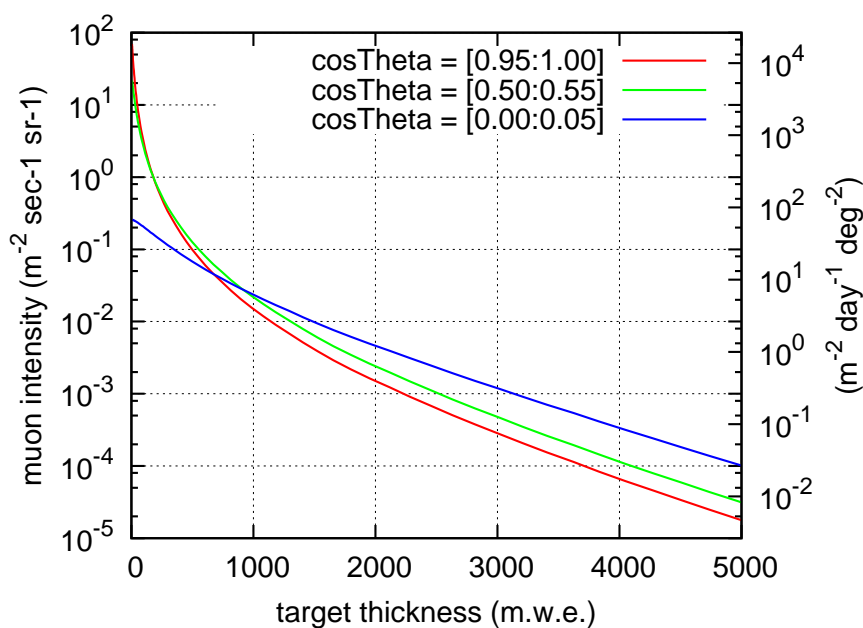


Figure 32: Integrated intensity of muons as a function of thickness for three zenith angle ranges.

B.4 Systematic Uncertainty in Density Estimation

This subsection discusses the systematic uncertainty in density estimation of muography which arises from the systematic uncertainty in the muon energy spectrum and the composition of rock.

B.4.1 Muon Energy Spectrum

Fig.33 represents the comparison between the theoretical energy spectrum used in the present study and the energy spectrum observed by the DEIS experiment. Although the two spectra seem to agree very well, there is a non-negligible discrepancy between them. The values of the discrepancy can be used as estimates of the systematic uncertainty in the energy spectrum.

Fig.34 represents the relative deviation of observation to theory. It is within

10 % below 400 GeV and it exceeds 10 % at some data points above 400 GeV because of large statistic fluctuations in observation. These values of the deviation can be converted into the systematic uncertainty in estimated density (Fig.35). The results show that the magnitude of systematic error is within 8 % when the thickness of rock is < 2000 m.w.e. This error is almost within the statistic error in the emulsion observation of the present work (see Table 5). However, further investigations on the energy spectrum are required to improve the accuracy of muography.

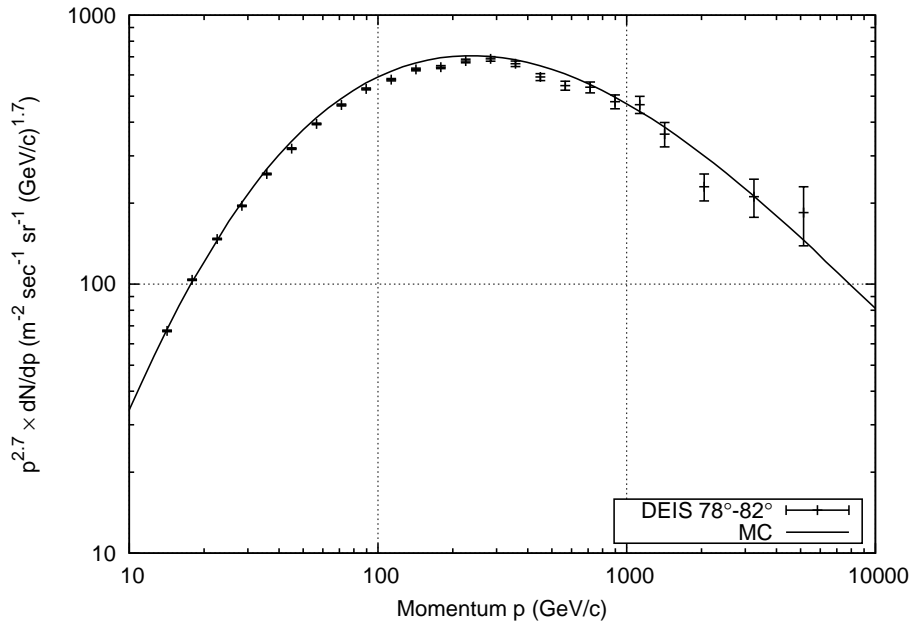


Figure 33: Muon energy spectrum for zenith angle $78^\circ - 82^\circ$ by the DEIS experiment with theoretical muon energy spectrum (solid line) used in this study.

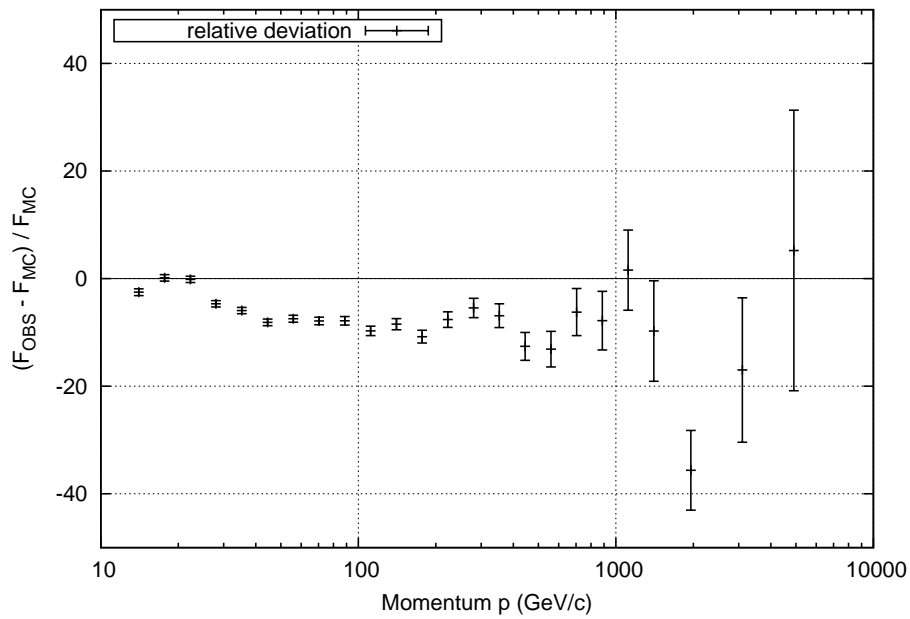


Figure 34: Relative deviation to theoretical energy spectrum for zenith angle $78^\circ - 82^\circ$

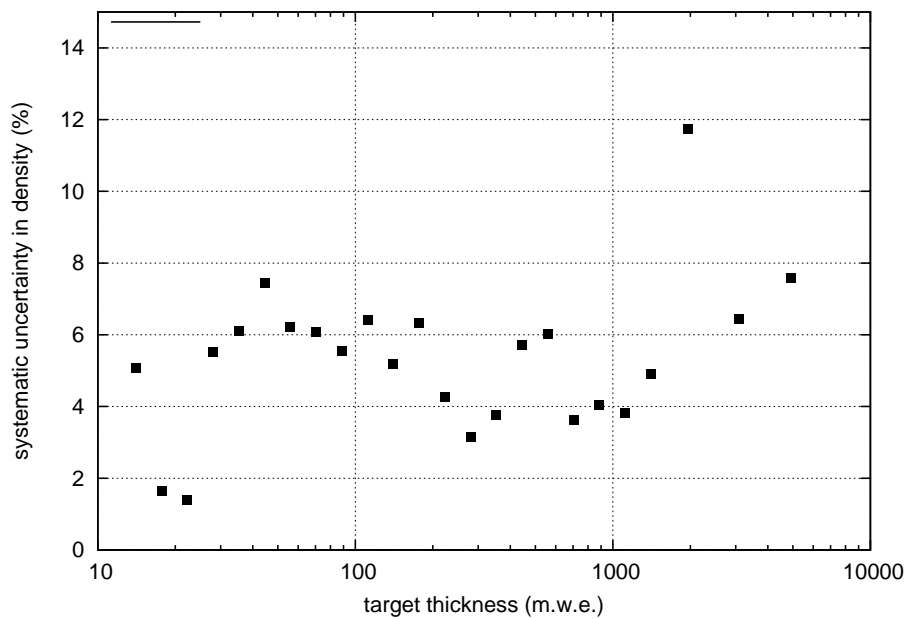


Figure 35: Systematic uncertainty in density estimation of muography as a function of target thickness (m.w.e.), converted from the relative deviation of the observed energy spectrum to theory.

B.4.2 Composition of Rock

The muon energy loss in the rock depends slightly on the composition. To be concrete, the ionization loss is proportional to the ratio of the atomic number (Z) to the atomic mass (A in g mol^{-1}) of the target. Table 6 represents the abundance of elements in the Earth's crust with their Z/A values. This shows that an average value $\langle Z/A \rangle$ can be affected mostly by the contents of Al and Fe in the rock. Considering 5 % fluctuations of FeO contents, the fluctuation in $\langle Z/A \rangle$ is $\delta\langle Z/A \rangle \sim 0.002$. The resultant error of muon range (i.e. density) can be roughly estimated to $\delta\langle Z/A \rangle / \langle Z/A \rangle \sim 0.4$ %. Thus the error arising from the uncertainty in composition is smaller than that from the muon energy spectrum.

element	abundance (wt.%)	Z	A (gmol^{-1})	Z/A
O	46	8	15.99	0.500
Si	27	14	28.08	0.499
Al	8.2	13	26.98	0.482
Fe	6.3	26	55.84	0.466
Ca	5.0	20	40.08	0.499
Na	2.3	11	22.98	0.479
K	1.5	19	39.09	0.486
Mg	2.9	12	24.30	0.494
Ti	0.66	22	47.87	0.460
H	0.15	1	1.007	0.993
Mg	0.10	12	24.3	0.493
total	100			0.496

Table 6: Abundance of elements in the Earth's crust with values of Z/A .

B.4.3 Remaining Uncertainties

There are several remaining uncertainties which have to be the subjects of future study. First, azimuthal dependence of the muon energy spectrum has

not been considered so far. The muon energy spectrum depends on azimuth angle at low energy region (probably $<$ a few tens of GeV) because of the geomagnetic field and the curvature of the Earth (see for example Lipari (2000)). Second, the dependence on the latitude and altitude of the detector site has to be understood. In the present work (Showa-Shinzan, h 200 masl.), the sea-level data were available. However, this is not the case for other volcanoes. Third, the multiple coulomb scattering of muons in the mountain has not been considered. Muons after passing through certain thickness of rock lose information on their original orientation (typically 10 mrad, reported by Borriello et al., 2010). The effect on the resultant density estimation has to be understood by a full Monte Carlo simulation ^{*3}. Accordingly, the effect of the electromagnetic shower induced from muon bremsstrahlung in the mountain has not been considered. The probability that these shower particles emerge from the mountain and hit the detector has to be quantified. If this effect is not negligible, it could cause a severe systematic uncertainty in muography.

^{*3}My MC simulation (Appendix D) is feasible to extract the effect of multiple scattering in the mountain. However I did not have time to discuss it.

C Joint Inversion of Muography and Gravity

Data

This section is an appendix of §3.2. This section describes the inversion of ECC muography results and gravity anomaly data observed at Mt. Showa-Shinzan. In C.1, the idea of the joint inversion is formulated. In C.2 and C.3, the data set used in this analysis is described. The results of 3-D density analysis are represented in C.4. The resolution of the inversion is confirmed by a checkerboard reconstruction test in C.5.

C.1 Methods

A number of gravity studies have been performed to infer subsurface density structures of volcanoes. However, these studies suffer from the well-known problem of non-uniqueness. Specifically, it is inherently impossible to uniquely determine the mass distribution from the external gravity potential alone (Zidarov, 1990).

In order to circumvent this problem, previous studies introduced additional constraints given by seismic explorations (eg. Lees and VanDecar, 1991; Coutant et al., 2012) or by borehole mining data (eg. Snyder and Carr, 1984). These extra constraints are helpful in solving the problem by reducing the number of unknown model parameters. However, it is still difficult to detect complex structures inside volcanoes such as vents and spines because the spatial resolution of seismological/gravimetric imaging is lim-

ited to the wavelength of seismic waves (> 1 km) and because spatially dense borehole drilling is practically impossible.

As described in §2, the muography exhibits extremely high spatial resolutions. Since muography and gravity survey are both sensitive to density, combining the two methods is expected to provide density profiles with higher spatial resolutions than conventional gravity inversion alone. Moreover, the combination will enable 3-D analysis, which is not possible by single-point muography. This subsection provides a formulation for joint inversion analysis of muography and gravity data.

C.1.1 Forward Modeling

Suppose the region of interest is subdivided into n voxels with density ρ_j ($j = 1, 2, \dots, n$) (Fig.36). The vertical component of gravity anomaly at the i th gravity station is then given as

$$\Delta g_i = \Delta g(x_i, y_i, z_i) = \sum_j^n G_{ij} \rho_j, \quad (18)$$

where G_{ij} is the gravity contribution of the j th voxel to the i th gravity station for unit density. Given a geometry of a voxel $D\{(x, y, z) | x_j^{\min} \leq x \leq x_j^{\max}, y_j^{\min} \leq y \leq y_j^{\max}, z_j^{\min} \leq z \leq z_j^{\max}\}$, G_{ij} can be written as

$$G_{ij} = \int_{x_j^{\min}}^{x_j^{\max}} \int_{y_j^{\min}}^{y_j^{\max}} \int_{z_j^{\min}}^{z_j^{\max}} \frac{\mathcal{G} \times (z_i - z)}{\sqrt{(x_i - x)^2 + (y_i - y)^2 + (z_i - z)^2}^3} dx dy dz, \quad (19)$$

where $\mathcal{G} = 6.674 \times 10^{-11}$ N m² kg⁻² is the universal gravitational constant.

An analytical integration of Eq. (19) was given by Nagy (1966). Here,

density-length X_i derived from muography is also expressed as,

$$X_i = \sum_j^n L_{ij} \rho_j, \quad (20)$$

where L_{ij} is the length of the i th muon path crossing the j th voxel. In this work, the data vector \mathbf{d} and the design matrix \mathbf{A} are defined as,

$$\mathbf{d} = \begin{pmatrix} \mathbf{X} \\ \Delta \mathbf{g} \end{pmatrix} \text{ and } \mathbf{A} = \begin{pmatrix} \mathbf{L} \\ \mathbf{G} \end{pmatrix}. \quad (21)$$

Eqs. (18) and (20) show that both gravity and muography data can be written as linear combinations of the voxel densities $\boldsymbol{\rho}$:

$$\mathbf{d} = \mathbf{A}\boldsymbol{\rho}. \quad (22)$$

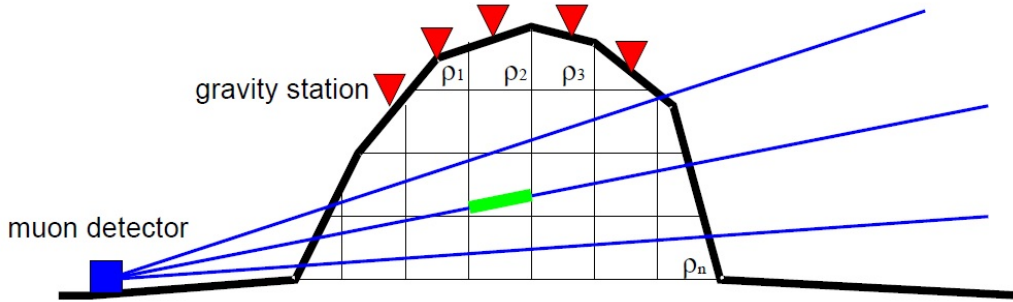


Figure 36: Schematic view of joint inversion of muography and gravity anomaly data.

C.1.2 Inverse Problem

Solving Eq. (22) for $\boldsymbol{\rho}$ is a linear inverse problem. Since this kind of problem is hugely under-determined, a Bayesian approach which was proposed by Tarantola and Valette (1982) is adopted in order to incorporate *a priori* information. It is assumed that the information we have on the true

value of data \mathbf{d} can be described by a Gaussian probability density function (p.d.f.) with observation \mathbf{d}_{obs} and a covariance matrix $\mathbf{C}_{\mathbf{d}}$. In addition, *a priori* information on model parameters that is also described by a Gaussian p.d.f. with an initial guess $\boldsymbol{\rho}_0 = (\rho_0, \rho_0, \dots, \rho_0)^{\text{T}}$ and a covariance matrix $\mathbf{C}_{\boldsymbol{\rho}}$ are introduced. The peak of posterior Gaussian function minimizes misfit function,

$$\chi^2 = (\mathbf{d}_{\text{obs}} - \mathbf{A}\boldsymbol{\rho})\mathbf{C}_{\mathbf{d}}^{-1}(\mathbf{d}_{\text{obs}} - \mathbf{A}\boldsymbol{\rho}) + (\boldsymbol{\rho} - \boldsymbol{\rho}_0)\mathbf{C}_{\boldsymbol{\rho}}^{-1}(\boldsymbol{\rho} - \boldsymbol{\rho}_0). \quad (23)$$

The model expectation $\boldsymbol{\rho}'$ and its posterior covariance matrix $\mathbf{C}'_{\boldsymbol{\rho}}$ are given as

$$\boldsymbol{\rho}' = \boldsymbol{\rho}_0 + (\mathbf{A}^{\text{T}}\mathbf{C}_{\mathbf{d}}^{-1}\mathbf{A} + \mathbf{C}_{\boldsymbol{\rho}}^{-1})^{-1}\mathbf{A}^{\text{T}}\mathbf{C}_{\mathbf{d}}^{-1}(\mathbf{d}_{\text{obs}} - \mathbf{A}\boldsymbol{\rho}_0), \quad (24)$$

and

$$\mathbf{C}'_{\boldsymbol{\rho}} = (\mathbf{A}^{\text{T}}\mathbf{C}_{\mathbf{d}}^{-1}\mathbf{A} + \mathbf{C}_{\boldsymbol{\rho}}^{-1})^{-1}. \quad (25)$$

Based on Tarantola and Nercessian (1984), we impose a smoothing constraint through an exponential covariance:

$$C_{\rho}(i, j) = \sigma_{\rho}^2 \exp(-d(i, j)/l), \quad (26)$$

where σ_{ρ} is the *a priori* error of the density, l is the correlation length, and $d(i, j)$ is the distance between the i th and j th voxels. When l is large, the inversion becomes an over-determined problem, whereas the problem becomes ill-posed when l is small.

In Eqs. (24) and (25), observation error must be introduced through the data covariance matrix $\mathbf{C}_{\mathbf{d}}$. It is composed of a covariance matrix of muogra-

phy data $\mathbf{C}_d^{\text{muon}}$ and that of gravity data $\mathbf{C}_d^{\text{grav}}$, since these two observations are independent:

$$\mathbf{C}_d = \begin{pmatrix} \mathbf{C}_d^{\text{muon}} & \mathbf{0} \\ \mathbf{0} & \mathbf{C}_d^{\text{grav}} \end{pmatrix}. \quad (27)$$

Components of each matrix are discussed later herein.

The muography covariance matrix is a diagonal matrix

$$\mathbf{C}_d^{\text{muon}} = \text{diag}\{\sigma_{\text{muon},1}^2, \sigma_{\text{muon},2}^2, \dots, \sigma_{\text{muon},p}^2\}, \quad (28)$$

because density-length X is determined independently for each muon path as a function of the number of detected muons (see §2.6.2).

Contrary to simpleness of $\mathbf{C}_d^{\text{muon}}$, $\mathbf{C}_d^{\text{grav}}$ is more complex, since gravity error arises from several error sources: reading error, drift and tidal correction error, leveling error, and terrain correction error. Reading error (σ_{read}) is within $10 \mu\text{gal}$ ($\mu\text{gal} = 10^{-8} \text{ m/s}^2$) in the case of LaCoste & Romberg relative gravimeter. Error in drift and tidal correction (σ_{corr}) can be reduced to the same magnitude of reading error if condition of gravimeter transportation is good. Leveling error affects gravity data, because magnitude of (normal) gravity vector depends on height. The gravity error arising from leveling error is given by using normal gravity gradient:

$$\sigma_{\text{level}} = 308.6 \mu\text{gal}/\text{meter} \times \Delta h, \quad (29)$$

where Δh is the magnitude of leveling error. Terrain correction error results from inaccurate DEM. It is roughly estimated to be

$$\sigma_{\text{DEM}} = 2\pi\rho G\Delta h_{\text{DEM}} = 41.9 \mu\text{gal} \times \left(\frac{\rho}{\text{g/cm}^3}\right) \left(\frac{\Delta h_{\text{DEM}}}{\text{meter}}\right), \quad (30)$$

where ρ is the typical density of rocks and Δh_{DEM} is vertical accuracy of DEM. The total observation error, which have to be assigned to diagonal elements of the gravity covariance matrix, is a root sum squares of the above mentioned error sources:

$$\sigma_{\text{grav}}^2 = \sigma_{\text{read}}^2 + \sigma_{\text{corr}}^2 + \sigma_{\text{level}}^2 + \sigma_{\text{DEM}}^2. \quad (31)$$

In this work, the dominant term in equation (31) is σ_{DEM}^2 , as discussed in C.2.3.

C.2 Data Sets

C.2.1 Muography Data

Muography data used in this analysis is described in § 2.6. The measurement was performed by exposing ECC detector with effective detection area of 104 cm^2 at 500 m west of the dome summit. The duration of exposure was 168 days. The entirety of the muon track data were binned, from which average densities were estimated, as shown in Fig.37a. A total of 30 bins were used in this analysis. The estimated error in each bin was assigned to diagonal elements of muography covariance matrix $\mathbf{C}_{\mathbf{d}}^{\text{muon}}$.

C.2.2 Gravity Data

A relative gravity survey was conducted at 30 stations on/around the lava dome using LaCoste and Romberg relative gravimeter G-875 over three days (12 - 14 April 2011). The positions of the gravity stations are represented

in Fig.37b. The survey started and ended everyday at a base station UVO, which is located 3km northwest of Showa-Shinzan. Absolute gravity was determined in advance with an FG5 absolute gravimeter at the reference station. The drift of the relative gravimeter was estimated from the closure error at the base UVO and at the local reference station GIH-2. The positions of the gravity stations were determined by GPS interferometry between a reference station and moving stations with accuracies of better than a few centimeters and 10 cm in the horizontal and vertical dimensions, respectively. For post-processing of the GPS data, an open source software RTKLIB ^{*4} was used.

After the station coordinates are obtained (Table 7), the free-air gravity anomaly is computed:

$$\Delta g^{\text{free-air}} = g^{\text{obs}} - \gamma(\phi) + \beta H, \quad (32)$$

where g^{obs} is the observed gravity, $\gamma(\phi)$ is the normal gravity at a geographic latitude ϕ (Heiskanen and Moritz, 1967), β is the free-air gravity gradient ($\beta = 3.086 \times 10^{-6} \text{ s}^{-2}$), and H is the station height above the geoid surface. The resultant free-air gravity anomaly value ranges from 68.15 mgal at the reference station GIH-2 to 78.67 mgal at the summit of the dome (Table 7).

C.2.3 Topography Data

The muon path lengths and topographic effects were calculated using the digital elevation model (DEM) published by the Geospatial Information Au-

^{*4}<http://www.rtklib.com/>

thority of Japan (<http://www.gsi.go.jp/>). The data are given for every 0.2'' in both the east-west and north-south directions (4.6 m in the east-west direction and 6.2 m in the north-south direction). The accuracy of the DEM is estimated by comparing the digital elevation with the coordinates measured by GPS at the gravity stations. Height difference between GPS and DEM is represented in Fig.38. Since RMS of the difference is 3.2 m (Fig.38a) and DEM errors do not seem correlated spatially (Fig.38b), it is concluded that DEM error is independent of the position and its amplitude is $\Delta h_{\text{DEM}} = 3.2$ m.

Here, gravity error is revisited. 10 cm of leveling error in our GPS measurement gives $\sigma_{\text{level}} = 30 \mu\text{gal}$. DEM error $\Delta_{\text{DEM}} = 3.2$ m gives $\sigma_{\text{DEM}} = 280 \mu\text{gal}$ by assuming a typical rock density $\rho = 2,100 \text{ kg/m}^3$. Based on equation (31), we give total gravity error $\sigma_{\text{grav}} = 300 \mu\text{gal}$ for diagonal elements of the gravity covariance matrix.

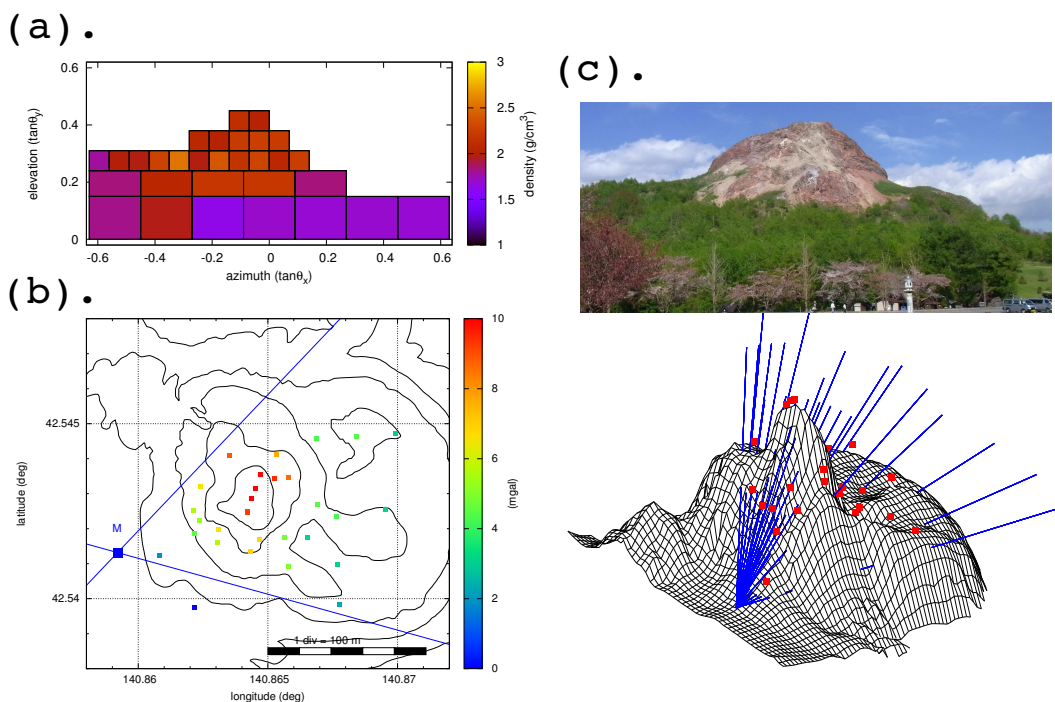


Figure 37: (a) Average density distribution estimated from muography with ECC detector. (b) Gravity stations (squares) with relative values of free-air gravity anomaly. “M” denotes the position of the muography detector. (c) Three-dimensional representation of the mountain, muon paths and gravity stations (vertical scale exaggerated). The picture was taken from near the muography detector.

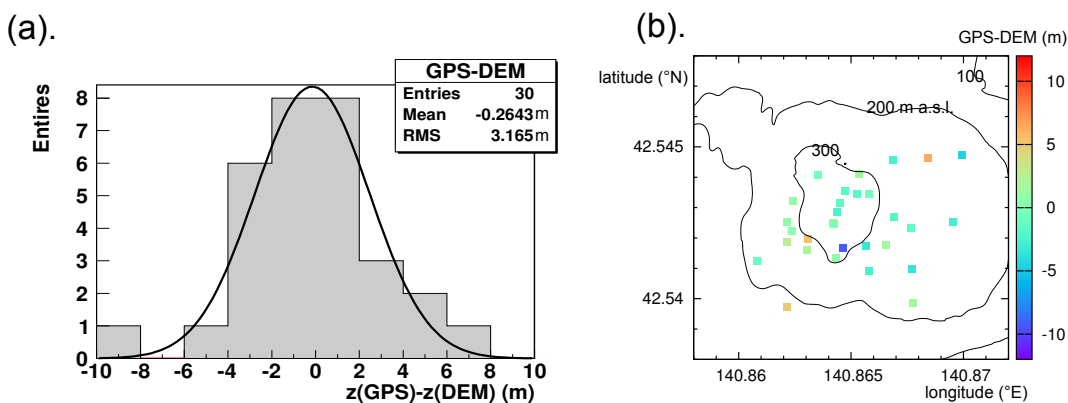


Figure 38: Comparison between GPS coordinates and digital elevation map (DEM) with (a) histogram representation and (b) spatial distribution.

C.3 Target Region

The target region, where we want to recover density, is defined as (42.539°N–42.548°N) (140.858°E – 140.872°E) (200 – 400 m.a.s.l.). This region is then divided into 2367 voxels having sides of 30 m and heights of 20 m. The model parameter ρ is represented as a vector having 2367 unknown values of voxel densities.

The free-air gravity anomaly is then decomposed into three components:

$$\Delta g^{\text{free-air}} = \Delta g^{\text{in}} + \Delta g^{\text{out}} + \Delta g^{\text{trend}}. \quad (33)$$

The first term, Δg^{in} , is the gravity effect of the masses within our target region. The second term, Δg^{out} , is the gravity effect of masses above the geoid but outside the target region, which was calculated by assuming a typical bulk density of the volcanic region $\rho^{\text{out}} = 2,100 \text{ kg/m}^3$. The third term, Δg^{trend} , is the regional trend arising from the deeper parts of the Earth. Since the Bouguer anomaly in Usu volcanic region 2 km(NS) \times 4 km(EW) ranges only within 52 – 54 mgal (Geological Survey of Japan, 2004), Δg^{trend} was assumed to be constant for all of the gravity stations, which are located within a sufficiently small area (600 m \times 600 m). Then, equation (18) was rewritten as follows:

$$\sum_j G_{ij} \rho_j = \Delta g_i^{\text{free-air}} - \Delta g_i^{\text{out}} - \Delta g_i^{\text{trend}}. \quad (34)$$

Δg^{trend} can be eliminated by subtracting the equation for the reference sta-

tion GIH-2 ($i = 1$):

$$(\Delta g_i^{\text{free-air}} - \Delta g_1^{\text{free-air}}) - (\Delta g_i^{\text{out}} - \Delta g_1^{\text{out}}) = \sum_j (G_{ij} - G_{1j}) \rho_j. \quad (35)$$

Following this equation, we rewrote the data vector and design matrix in equation (21).

C.4 Results

The *a priori* parameters are determined as follows: $\rho_0 = 1900 \text{ kg/m}^3$, $\sigma_\rho = 300 \text{ kg/m}^3$ and $l = 100 \text{ m}$. The initial density (ρ_0) is deduced from average of the density in 30 bins from the muography result. The initial error (σ_ρ) and the correlation length (l) are optimized so that resultant misfit χ^2 becomes nearly the number of data ($\nu_{\text{muon}} + \nu_{\text{grav}} = 30 + 29 = 59$) (Fig.39).

The inverted density profile is represented in Fig.40. The estimated model explains the observed muography and gravity data very well (Fig.41). Muography residuals $\chi_{\text{muon}}^2 = 21.3 (\nu_{\text{muon}} = 30)$ and gravity residuals $\chi_{\text{grav}}^2 = 14.0 (\nu_{\text{grav}} = 30 - 1 = 29)$ guarantee that our estimation is statistically reasonable. The estimation error is given by diagonal elements of the posterior covariance matrix \mathbf{C}'_ρ (Fig.43). The error is 200 kg/m^3 in general, whereas it is improved to approximately 150 kg/m^3 near the summit and the gravity stations. In the eastern part of the uplifted plateau, where only sparse data is available, the density error is no better than 300 kg/m^3 , which is originally given as the prior error. The resolution of this inversion is discussed in the next subsection.

The reconstructed density profile shows that the western part of the mountain, where the lava dome exists, has higher density ($> 2000 \text{ kg/m}^3$) than the eastern part of the mountain, where the uplifted plateau exists. The lava dome consists of a massive lava column with diameter of $\sim 300 \text{ m}$.

C.5 Resolution Study

The resolution of the joint inversion is confirmed by a checkerboard reconstruction test. The input density model ρ_{syn} , which we want to recover, is composed of alternating high-density ($\rho_{\text{high}} = 2,200 \text{ kg/m}^3$) and low-density ($\rho_{\text{low}} = 1,600 \text{ kg/m}^3$) voxels of $\Delta x = \Delta y = 200 \text{ m}$ in the horizontal and $\Delta z = 100 \text{ m}$ in vertical dimensions (Fig.44a). This 3D checkerboard pattern is superimposed on the topography of the mountain. This model enables us to make synthetic data \mathbf{d}_{syn} : density-lengths (X) of the 30 muon paths and gravity anomaly values Δg^{in} for the 30 stations. The Gaussian random noises then are added to \mathbf{d}_{syn} . In this test, the gravity from outside our target region was neglected.

The reconstructed pattern is shown in Fig.44b. Although the square shapes of the checkerboard are not fully reproduced because of the correlation assumption, the overall characteristics (position and amplitude of anomaly) are recovered very well. Thus the horizontal and vertical resolutions are assured to be better than $\Delta x = \Delta y = 200 \text{ m}$ and $\Delta z = 100 \text{ m}$, respectively.

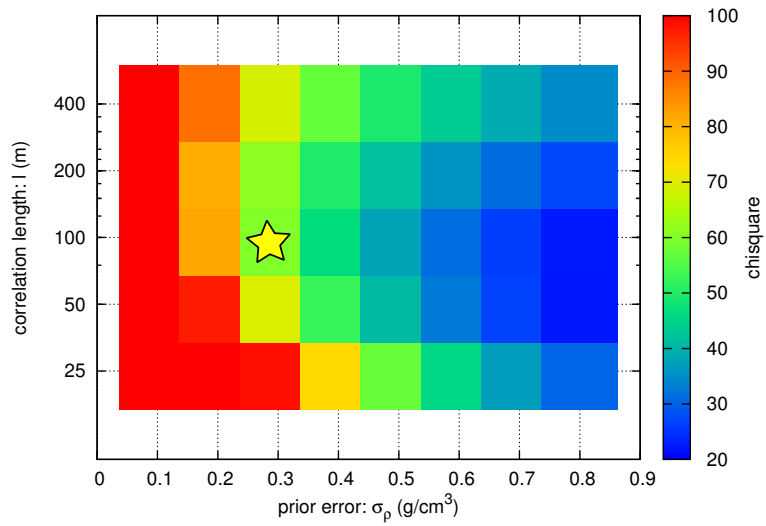


Figure 39: Resultant chisquare values for a various sets of prior density error and correlation length. The best *a priori* parameters are indicated by the star.

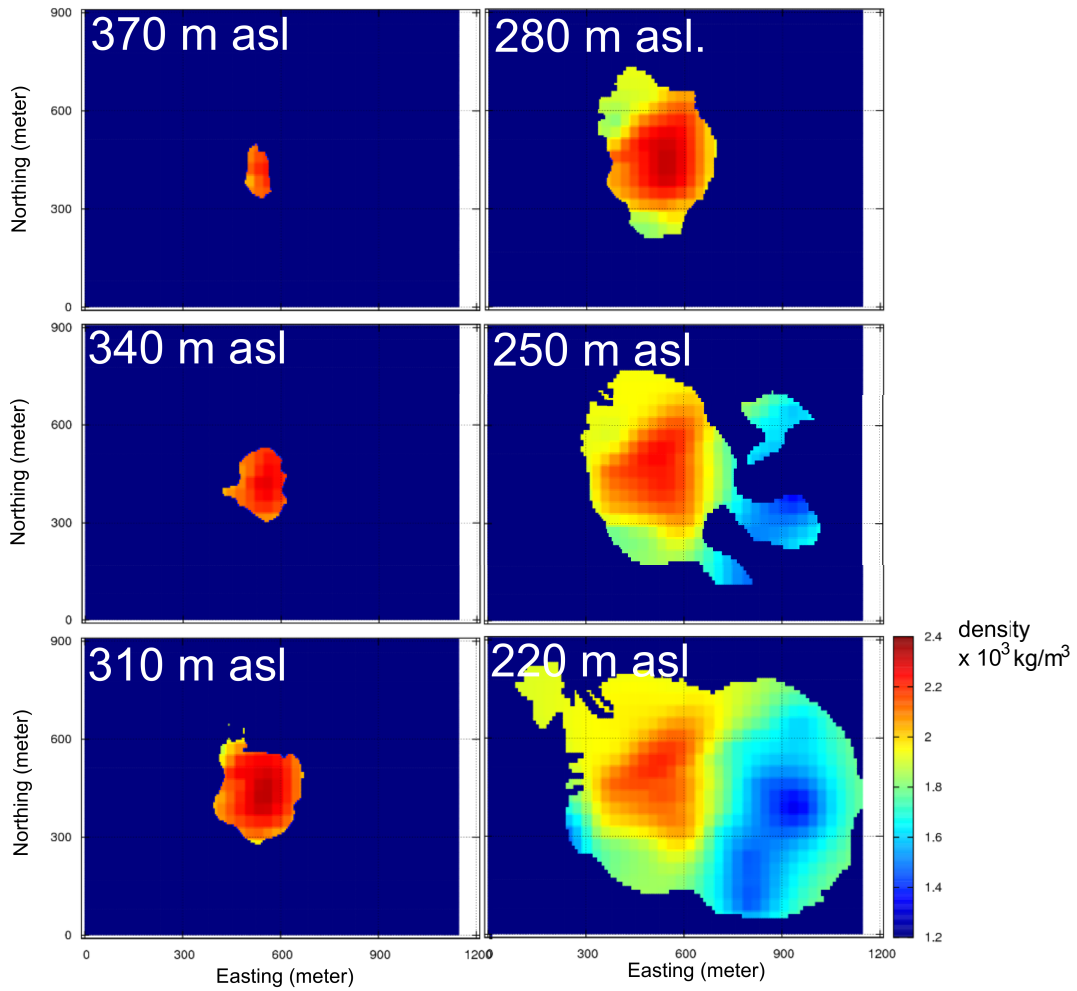


Figure 40: Cross-sectional density profile at altitudes of 370, 340, 310, 280, 250, 220 m asl, determined from the joint inversion of muography and gravity data. Comparison with a 3-D model derived from conventional muography result is given in Fig.26.

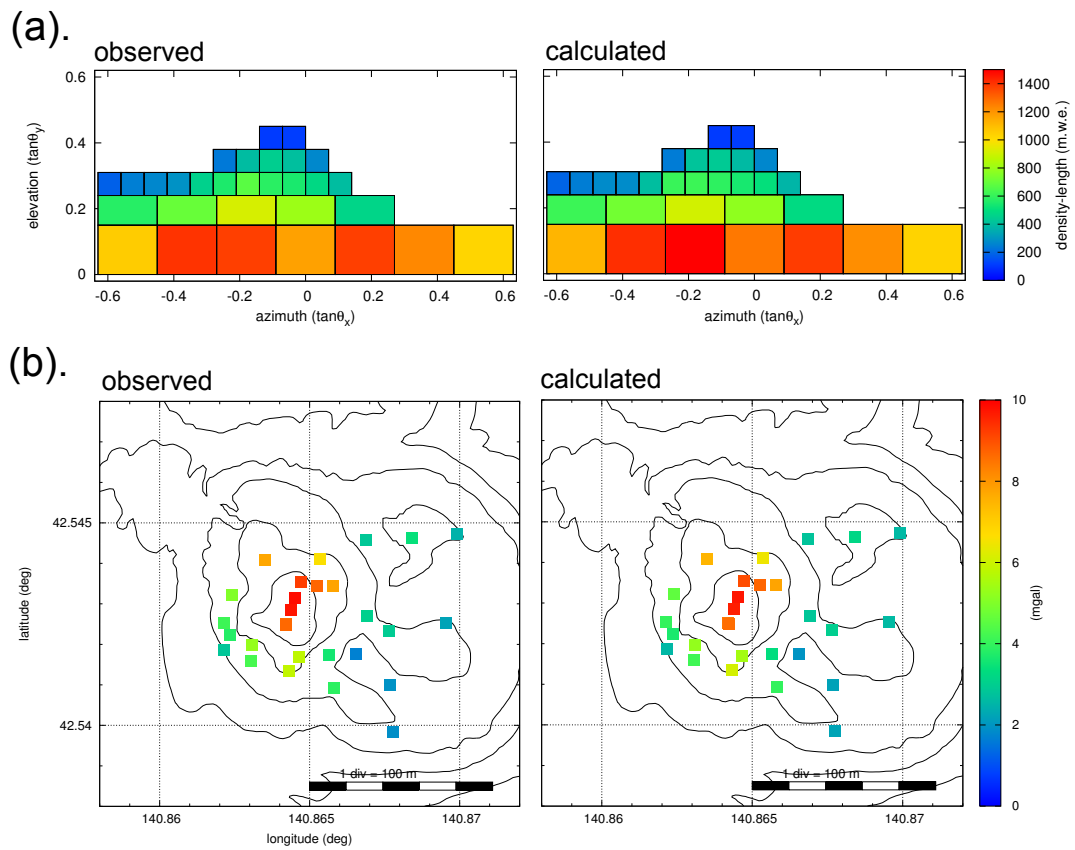


Figure 41: Comparison between observed and calculated data of (a) muography and (b) gravity.

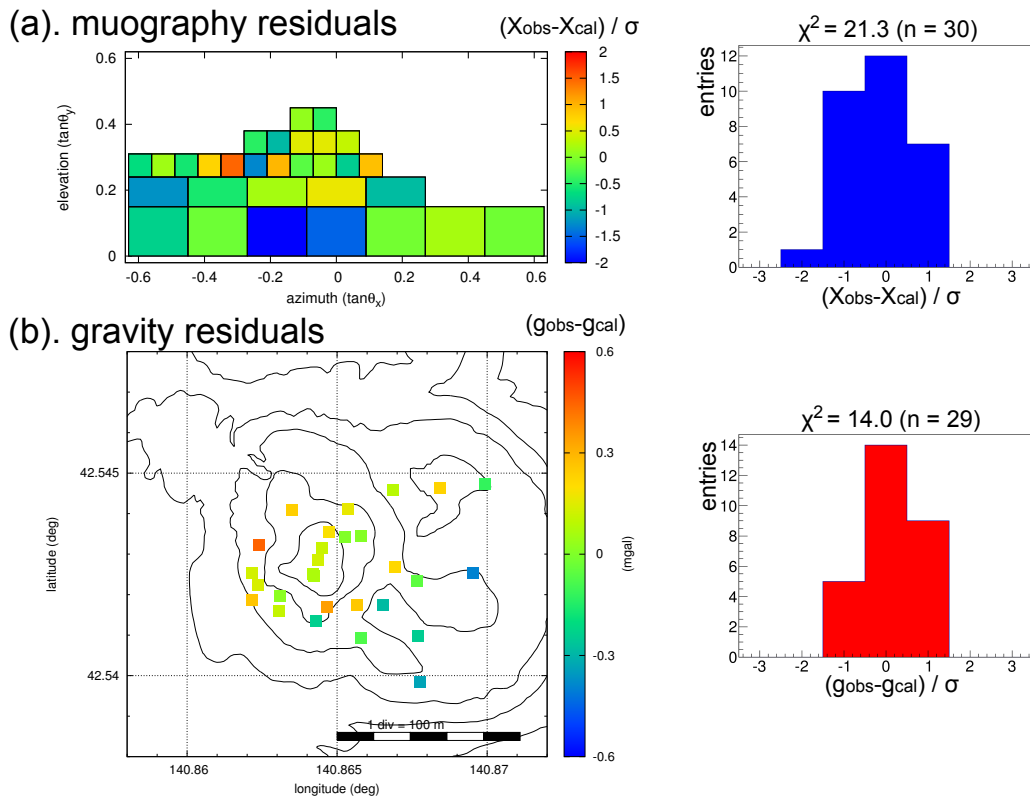


Figure 42: Residuals of (a) muography data and (b) gravity data.

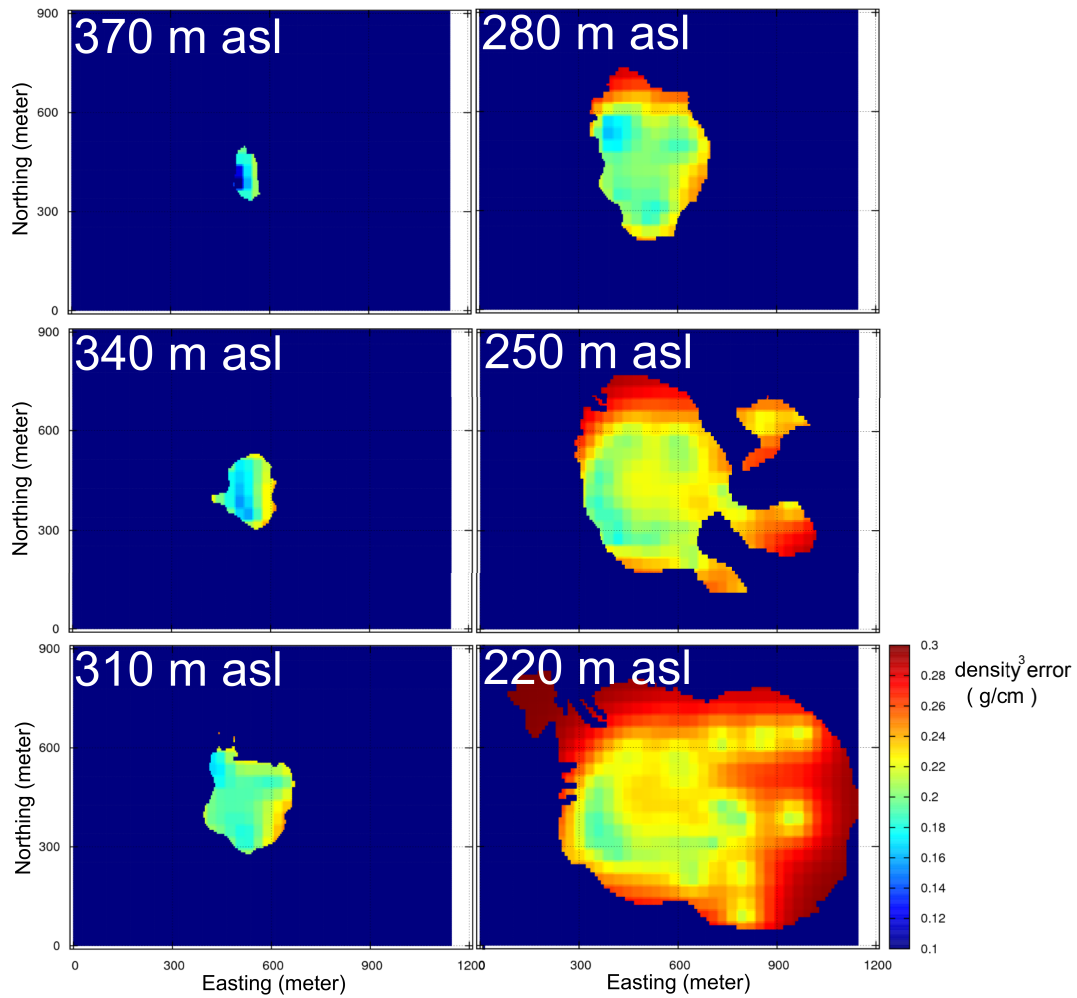


Figure 43: Density errors at altitudes of 370, 340, 310, 280, 250 and 220 m asl, estimated from diagonal elements of the posterior covariance matrix.

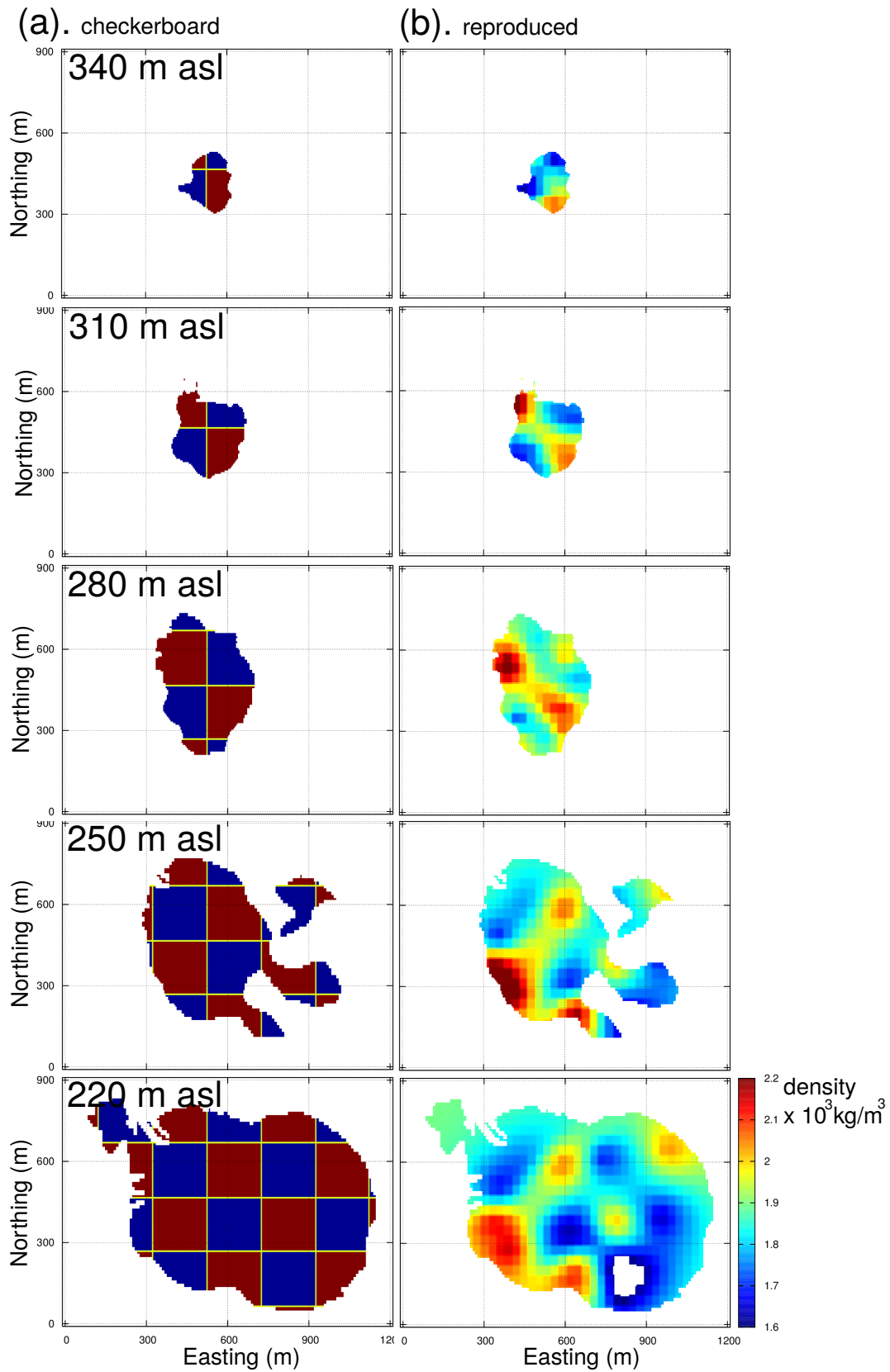


Figure 44: (a) Checkerboard density model superimposed on the shape of Showa-Shinzan. (b) Density model reproduced from the synthetic muography and gravity data.

Site	Latitude (deg min sec)			Longitude (deg min sec)			Altitude (m)	g (mgal)	$\Delta g^{\text{free-air}}$ (mgal)
GIH-2	42	32	23.07	140	51	43.75	189.66	980407.172	68.147
GIH-1-2	42	32	28.42	140	51	38.97	208.18	980403.525	70.082
GIH-1-1	42	32	30.70	140	51	43.77	250.79	980392.997	72.647
SSmG-C	42	32	33.08	140	51	43.73	271.65	980387.805	73.830
SSmG-D	42	32	35.57	140	51	44.62	276.92	980387.108	74.697
SSmG-E	42	32	38.72	140	51	48.64	313.53	980378.217	77.026
SSmG-F	42	32	38.80	140	51	55.26	302.95	980380.274	75.817
SSmG-G	42	32	36.42	140	51	56.81	329.34	980373.012	76.758
SSmG-H	42	32	36.35	140	51	54.91	343.14	980369.635	77.642
SSmG-I	42	32	36.74	140	51	52.97	362.43	980364.143	78.094
SSmG-J	42	32	35.36	140	51	52.24	376.77	980360.256	78.665
SSmG-K	42	32	34.30	140	51	51.77	384.48	980357.719	78.533
SSmG-L	42	32	33.01	140	51	51.12	397.84	980352.292	77.262
SSmG-L2	42	32	32.90	140	51	51.21	397.72	980352.437	77.372
GIH-1	42	32	32.03	140	51	44.49	270.87	980387.687	73.499
SSmG-R	42	32	29.76	140	51	46.97	275.48	980386.554	73.846
SSmG-Q	42	32	31.12	140	51	47.09	297.61	980380.665	74.751
SSmG-O	42	32	28.83	140	51	51.53	308.26	980377.597	75.028
SSmG-M	42	32	30.07	140	51	52.78	314.11	980375.772	74.975
SSmG-M2	42	32	30.26	140	51	56.37	273.91	980386.195	72.988
SSmG-Y1	42	32	30.31	140	51	59.56	243.01	980394.068	71.324
SSmG-Y2	42	32	33.69	140	52	0.92	254.10	980391.995	72.591
SSmG-Y3	42	32	40.50	140	52	0.73	245.61	980394.614	72.419
SSmG-Y4	42	32	40.69	140	52	6.33	256.34	980391.422	72.534
SSmG-Y5	42	32	41.03	140	52	11.71	247.23	980392.850	71.142
SSmG-Y6	42	32	27.33	140	51	56.91	270.84	980387.186	73.107
SSmG-Y7	42	32	23.44	140	52	3.95	245.60	980392.206	70.435
SSmG-Y8	42	32	27.55	140	52	3.69	243.18	980393.881	71.261
SSmG-Y9	42	32	32.40	140	52	3.58	251.54	980392.558	72.394
SSmG-Y10	42	32	33.13	140	52	10.32	249.03	980392.283	71.326

Table 7: Description of gravity data.

D Monte Carlo Simulation of Background Noise

This section is an appendix of § 3.3. In § 3.3, the particle fluxes measured by quartet and ECC detectors are compared with a Monte Carlo (MC) simulation. This chapter describes detail of the MC simulation.

D.1 Methods

The simulation was performed by combining two MC codes: COSMOS^{*5} and GEANT4 (Agostinelli et al., 2003). The former produce the energy spectrum of major cosmic particles (muons, electrons, gamma-rays, protons and neutrons) at an altitude of a detector by considering primary energy spectra, production of secondary cosmic rays and their transportation in the atmosphere. The latter constructs a virtual mountain and a detector, and injects particles following the reproduced energy spectra from a substantially large hemisphere enclosing the mountain and the detector.

D.2 COSMOS Simulation

COSMOS is a MC code for propagation of cosmic rays in the atmosphere. This code is widely used in the field of cosmic-ray physics. For instance, the Telescope Array experiment employs COSMOS to calculate longitudinal developments of ultra-high energy cosmic rays. The performance of COSMOS is confirmed by comparison with other MC codes and observations (Roh et

^{*5}<http://cosmos.n.kanagawa-u.ac.jp/>

al., 2013). In this simulation, the COSMOS version 7.641 was used.

D.2.1 Simulation Setup

The interaction models are as follows: PHITS (Niita et al., 2006) for $E < 2$ GeV; DPMJET-III (Roesler et al., 2001) for $2 \leq E < 100$ GeV; QGSJET-II-03 (Ostapchenko, 2006) for $100 \text{ GeV} \leq E$ ^{*6}.

Primary spectra of protons and helium are taken from BESS experiment (Sanuki et al., 2000). Protons and helium nuclei are injected at 400 km high in the atmosphere. The spherical shape of the Earth is considered. The particle development (secondary production, decay and etc...) are traced for particles with $E > 0.1$ GeV to save computation time and get better statistics. Particles passing through virtual spheres at 3000, 1500, 500, 300, 50 and 30m asl are restored. To be concrete, particle type, charge, kinetic energy, momentum are restored.

The computation was performed using SGI Atlix UV 1000 of Earthquake Research Institute, the University of Tokyo. The computation time was approximately 1.3×10^4 hours \times cores.

^{*6}There are no interaction models which can predict the hadronic interactions in the whole energy range. Therefore several models have to be introduced to simulator. PHITS (Particles and Heavy Ion Transport code System) is an aggregate of the several proven models. DPMJET-III and QGSJET-II are based on parton-based Gribov Regge Theory, which describes the hadronic interaction as a pomeron (purely theoretical particles) exchange between partons.

D.2.2 Results

Fig.45 represents the energy spectra derived from COSMOS simulation. The results are compared with pre-existing observations. The specification of the observations are tabulated in Table 8. In general, the MC results agree with the experimental data. Nevertheless, there are differences for electrons and protons. To be concrete, the MC electron flux exceeds the literature values at 1.4 GeV by 70%. The MC proton flux is lower than the literature values at 10 GeV by a factor of two. Thus, it is concluded that the systematic uncertainty in the spectrum calculated by this simulation is within a factor of two.

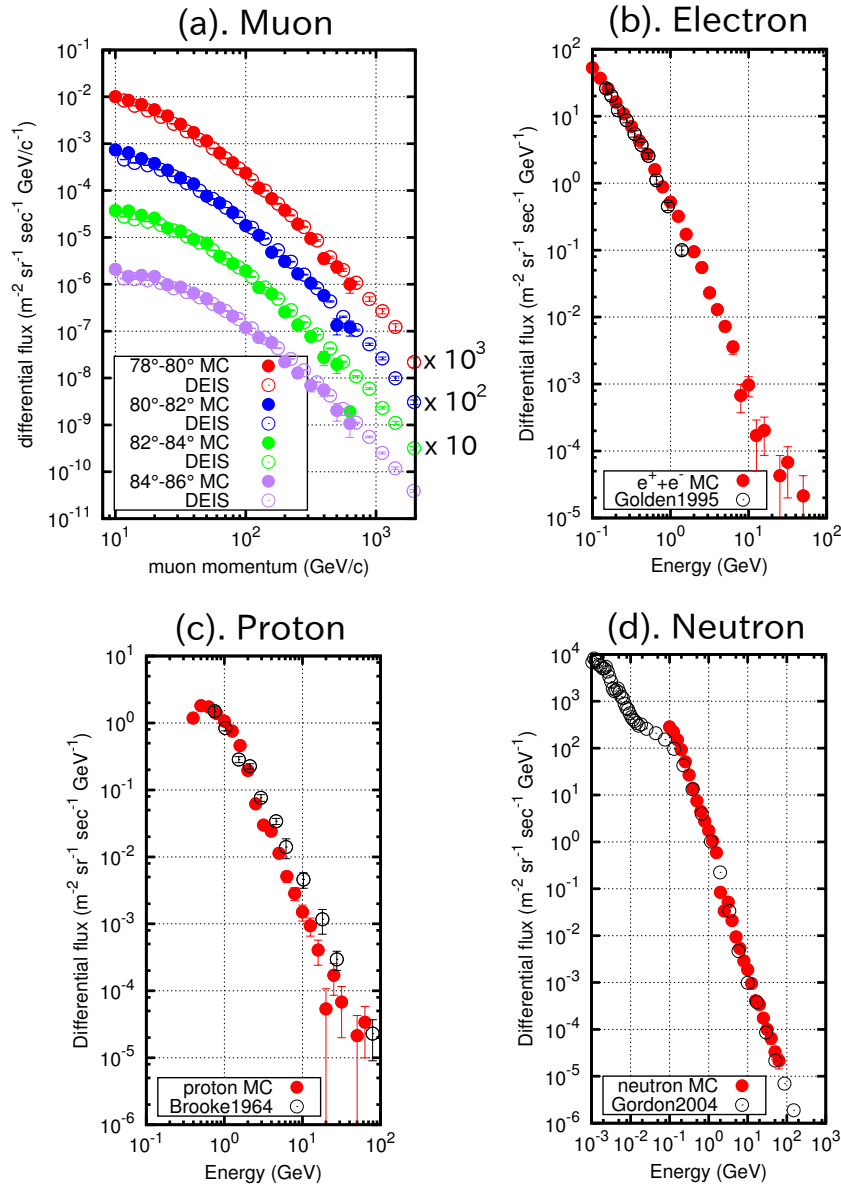


Figure 45: Energy spectra of (a) muons, (b) electrons, (c) protons and (d) neutrons calculated by COSMOS at nearly sea level. Solid circles denote the COSMOS results. Open circles denote the energy spectrum measured by prior works (see Table 8).

particle	paper	height (m)	long/lat	year	zenith angle	energy
muon	Allkofer et al. (1985)	-	-	-	$79^\circ - 90^\circ$	-
electron	Golden et al. (1995)	sea level	$53^\circ\text{N}, 106^\circ\text{W}$	1993	vertical	0.1 – 2 GeV
proton	Brooke and Wolfendale (1964)	sea level	$54^\circ\text{N}, 1^\circ\text{W}$	1960 – 62	vertical	subGeV - 100 GeV
neutron	Gordon et al. (2004)	167 m	$41^\circ\text{N}, 73^\circ\text{W}$	2002 – 03	omni-directional	MeV - 100 GeV

Table 8: Observation data compared with the results of COSMOS.

D.3 GEANT4 Simulation

GEANT4 is a toolkit for simulation the passage of particles through matter. In this study, a virtual mountain and a virtual detector are constructed in the computational space of GEANT4, and the cosmic particles are injected from a virtual hemisphere enclosing the mountain and the detector.

The configuration of the simulation is later herein.

Mountain

In this simulation, the rotational-symmetric shape of the mountain is realized by small prisms with horizontal dimension of $\Delta x = \Delta y = 10$ m. The mountain consists of quartz with density of 2.36 g/cm³. The size of the mountain is adjusted so that the rock thickness becomes nearly equals to our observation at Showa-Shinzan. The computational region is filled with air (1 atm). The dimensions of the computational region are given in Fig.28a.

Detector

The mountain is surrounded by a virtual detector with radius of 500 m and vertical dimension of 10 m. The total area of the detector is 3.1×10^4 m². The virtual detector records the information of particles passing through it.

Interaction Model

For electromagnetic interaction, the GEANT4 standard electromagnetic physics is used. For hadronic interaction, FTFP_BERT model is

employed.

Injection Method

The particles are injected from a surface of an oblate spheroid with long axial radius of $R = 600$ m and short axial radius of $R_z = 300$ m. The spheroid encloses the mountain and detector. The kinetic energy, direction of the injected particles are sampled based on the energy spectrum produced by COSMOS simulation.

From the virtual hemisphere, 2 billion muons were injected. 0.5 billion EM particles were injected (e^- 19%; e^+ 17%; γ 64%). 0.5 billion hadronic particles (proton 13%; neutron 87%) were injected. These quantity corresponds to the numbers of particles falling down onto the hemisphere in ~ 15 secs. The calculation was performed using SGI Atlix UV 1000 of Earthquake Research Institute, the University of Tokyo. The computation time was 2.5×10^4 hours \times cores.

D.4 Results

Fig.28b represents the angular distribution of particles which hit the virtual detector. These particles can be classified into four components: (i) signal muons; (ii) protons; (iii) muons and electrons produced from the hadronic interaction; (iv) electrons from electromagnetic showers. For quantitative discussion, two angular domains are defined: domain A (sky) [$0.45 \leq \cos \theta < 0.52$]; domain B (mountain) [$0 \leq \cos \theta < 0.18$]. Fig.29 represents the inte-

grated energy spectrum for each domain. From the number of the hits, the particle energy spectrum are calculated for the sky region (Fig.29a) and the mountain region (Fig.29b).

For the sky region, the dominant particle is cosmic-ray muons for all energy range. The next dominant particles are muons and electrons produced from hadronic interaction. The least dominant particles are protons. For the mountain region, however, the protons and hadronic-induced charged particles are dominant in the low energy region ($E < 0.5 \text{ GeV}$). At higher energy ($E > \sim 1 \text{ GeV}$), the penetrating muons becomes dominant.

Acknowledgements

I would like to express my deepest gratitude to the following people for their generous supports. This work would never be completed without them.

First of all, Dr. Shuhei Okubo guided and encouraged me in every phase of this research as a supervisor. Dr. Hiroyuki Tanaka planted me a seed of curiosity about this research topic. I have learned handling of nuclear emulsions from Dr. Seigo Miyamoto. He always provided me with opportunities for my new challenges. I have learned many things from Dr. Akimichi Taketa. His continuing encouragement and critical comments always strengthen me.

I have got enormous help on gravity survey and GPS processing from Dr. Yoshiyuki Tanaka. Dr. Kiwamu Nishida gave me advice on the inversion analysis method. Ms. Yoshiko Imoto helped me a lot for budget management.

I wish to thank Dr. Hiromitsu Oshima and Mr. Tokumitsu Maekawa (Hokkaido University) for their generous support on the field work at Usu volcanic region. I have learned many things from their sincere attitudes to field survey. Mr. Saburo Mimatsu (Mimatsu Masao Memorial Museum) allowed us to perform gravity survey on Mt. Showa-Shinzan. Beautification Escort Staff at Shikotsu-Toya National Park provided us with a site for the emulsion experiments.

I am grateful to Dr. Cristiano Bozza (Salerno University) for his continuing support on the use of the European Scanning System. I acknowledge

with gratitude the tremendous support given us in the use of the FEDRA framework by Dr. Valeri Tioukov (INFN, Napoli).

I wish to thank Dr. Mitsuhiro Nakamura, Dr. Kunihiro Morishima, Dr. Naotaka Naganawa (F-lab, Nagoya University) and their colleagues for their support in preparing and developing the emulsion films.

I have got kind introduction on the use of the COSMOS simulator from Dr. Katsuaki Kasahara (Waseda University). The Monte Carlo simulation was performed using EIC system, Earthquake Research Institute, the University of Tokyo.

During my PhD program, I have got financial supports from GCOE program From Earth to Earths, Leading Graduate Course for Frontiers of Mathematical Science and Physics (FMSP program), and JSPS Fellowship (DC2, 25-9317). My housing was supported by Incorporated Foundation, Mother Lake Shiga (湖国寮).

Finally, I wish to thank my parents for supporting me all the time.

References

- Agafonova, N. et al., “Momentum measurement by the multiple Coulomb scattering method in the OPERA lead-emulsion target,” *New J. Phys.*, 2012, *14*, 013026.
- and —, “Observation of tau neutrino appearance in the CNGS beam with the experiment,” *Progress of Theoretical and Experimental Physics*, 2014, *2014* (10).
- Agostinelli, S, J Allison, K. Amako, J. Apostolakis, H. Araujo, P. Arce, M. Asai, D. Axen, S. Banerjee, G. Barrand et al., “GEANT4- a simulation toolkit,” *Nucl. Instrum. Meth. A*, 2003, *506* (3), 250–303.
- Allkofer, O.C., G. Bella, W.D. Dau, H. Jokisch, G. Klemke, Y. Oren, and R. Uhr, “Cosmic ray muon spectra at sea-level up to 10 TeV,” *Nuclear Physics B*, 1985, *259* (1), 1–18.
- Alvarez, L. W., J. A. Anderson, F. E. Bedwei, J. Burkhard, A. Fakhry, A. Girgis, A. Goneid, F. Hassan, D. Iverson, G. Lynch, Z. Miligy, A. H. Moussa, M. Sharkawi, and L. Yazolino, “Search for Hidden Chambers in the Pyramids,” *Science*, 1970, *167* (3919), 832–839.
- Ambrosi, G., F. Ambrosino, R. Battiston, A. Bross, S. Callier, F. Cassese, G. Castellini, R. Ciaranfi, F. Cozzolino, R. D’Alessandro, C. de La Taille, G. Iacobucci, A. Marotta, V. Masone, M. Martini, R. Nishiyama, P. Noli, M. Orazi, L. Parascandolo, P. Parascandolo, G. Passeggio, R. Peluso, A. Pla-Dalmau, L. Raux, R. Rocco, P. Rubinov, G. Saracino, G. Scarpato, G. Sekhniadze, P. Strolin, H.K.M. Tanaka, M. Tanaka, P. Trattino, T. Uchida, and I. Yokoyamao, “The MU-RAY project: Volcano radiography with cosmic-ray muons,” *Nucl. Instrum. Meth. A*, 2011, *628* (1), 120 – 123.
- Arrabito, L., C. Bozza, S. Buontempo, L. Consiglio, M. Cozzi, N. D’Ambrosio, G. De Lellis, M. De Serio, F. Di Capua, D. Di Ferdinando, N. Di Marco, A. Ereditato, L. S. Esposito, R. A. Fini, G. Giacomelli, M. Giorgini, G. Grella, M. Ieva, J. Janicsko Csathy, F. Juget, I. Kreslo, I. Laktineh, K. Manai, G. Mandrioli, A. Marotta, P. Migliozi, P. Monacelli, U. Moser, M. T. Muciaccia, A. Pastore, L. Patrizzii, Y. Petukhov, C. Pistillo, M. Pozzato, G. Romano, G. Rosa, A. Russo, N. Savvinov, A. Schembri, L. Scotto Lavina, S. Simone, M. Sioli, C. Sirignano, G. Sirri, P. Strolin, V. Tioukov, and T. Waelchli, “Track reconstruction in the emulsion-lead target of the OPERA experiment using the ESS microscope,” *Journal of Instrumentation*, 2007, *2* (05), P05004.
- , E. Barbuto, C. Bozza, S. Buontempo, L. Consiglio, D. Coppola, M. Cozzi, J. Damet, N. D’Ambrosio, G. De Lellis et al., “Hardware performance of a scanning system for high speed analysis of nuclear emulsions,” *Nucl. Instrum. Meth. A*, 2006, *568* (2), 578–587.
- Barnaföldi, G. G., G. Hamar, H. G. Melegh, L. Oláh, G. Surányi, and D. Varga, “Portable cosmic muon telescope for environmental applications,” *Nucl. Instrum. Meth. A*, 2012, *689*, 60 – 69.
- Beringer, J et al., “Review of particle physics,” *Physical Review D*, 2012, *86* (1).
- Borozdin, K. N., G. E. Hogan, C. Morris, W. C. Priedhorsky, A. Saunders, L. J. Schultz, and M. E. Teasdale, “Surveillance: Radiographic imaging with cosmic-ray muons,” *Nature*, March 2003, *422* (6929), 277.

- Borriello, E., G. De Lellis, G. Mangano, A. Marotta, G. Miele, P. Migliozzi, C. Moura, S. Pastor, O. Pisanti, P. Strolin, and A. Zollo, "Simulations of neutrino and muon interaction in matter for geological structures radiography," *Eath Planets Space*, 2010, *62*, 187–193.
- Bozza, C., L. Consiglio, N. D'Ambrosio, G. De Lellis, C. De Serio, N. Di Marco, U. Kose, E. Medinaceli, S. Miyamoto, R. Nishiyama, F. Pupilli, S. M. Stellacci, C. Sirignano, H. K. M. Tanaka, and V. Tioukov, "Muon radiography by nuclear emulsions: data acquisition and processing," in "IAVCEI 2013 Scientific Assembly" 2013.
- Brooke, G. and A. W. Wolfendale, "The momentum spectrum of cosmic ray protons near sea level in the momentum range 0.6-150 GeV/ c," *Proceedings of the Physical Society*, 1964, *83* (5), 843.
- Carbone, D., D. Gibert, J. Marteau, M. Diament, L. Zuccarello, and E. Galichet, "An experiment of muon radiography at Mt Etna (Italy)," *Geophys. J. Int.*, 2014, *196* (2), 633–643.
- Cârloganu, C., V. Niess, S. Béné, E. Busato, P. Dupieux, F. Fehr, P. Gay, D. Miallier, B. Vulpescu, P. Boivin, C. Combaret, P. Labazuy, I. Laktineh, J.-F. Lénat, L. Mirabito, and A. Portal, "Towards a muon radiography of the Puy de Dôme," *Geosci. Instrum. Method. Data Syst.*, 2013, *2*, 55–60.
- Coutant, O., M. L. Bernard, F. Beauducel, F. Nicollin, M. P. Bouin, and S. Roussel, "Joint inversion of P-wave velocity and density, application to La Soufrière of Guadeloupe hydrothermal system," *Geophys. J. Int.*, 2012, *191* (2), 723–742.
- Dedenko, L.G., A.K. Managadze, T.M. Roganova, A.V. Bagulya, M.S. Vladimirov, S.G. Zemskova, N.S. Konovalova, N.G. Polukhina, N.I. Starkov, M.M. Chernyavskiy, and V.M. Grachev, "Prospects of the study of geological structures by muon radiography based on emulsion track detectors," *Bulletin of the Lebedev Physics Institute*, 2014, *41* (8), 235–241.
- Geological Survey of Japan, *Gravity CD-ROM of Japan (ver. 2)*, Geological Survey of Japan, AIST, 2004.
- Golden, R. L., S. A. Stephens, S. J. Stochaj, W. R. Webber, M. T. Brunetti, A. Codino, C. Grimani, M. Menichelli, I. Salvatori, M. P. De Pascale et al., "Measurement of the energy spectra of cosmic ray electron component and protons at ground level," *J. Geophys. Res.:Space Physics*, 1995, *100* (A12), 23515–23522.
- Gordon, M. S., P. Goldhagen, K. P. Rodbell, T. H. Zabel, H. H. K. Tang, J. M. Clem, and P. Bailey, "Measurement of the flux and energy spectrum of cosmic-ray induced neutrons on the ground," *Nuclear Science, IEEE Transactions on*, 2004, *51* (6), 3427–3434.
- Goto, Y. and A. Johmori, "Resistivity Structure of the Showa-Shinzan Dome at Usu Volcano, Hokkaido, Japan," *Bull. Volcanol. Soc. Japan*, 2014, *59*, 1–11.
- , Y. Ito, Y. Yokoyama, T. Matsui, and S. Mimatsu, "Internal structure of a subaerial dacite cryptodome at Usu volcano, Hokkaido, Japan," *Mem. Muroran Inst. Tech.*, 2004, *54*, 3–10.
- Grieder, P. K. F., *Cosmic Rays at Earth - Researcher's Reference Manual and Data Book*, Elsevier, 2001.

- Groom, D. E., N. V. Mokhov, and S. I. Striganov, “Muon Stopping Power and Range Tables 10 MeV-100 TeV,” *Atomic Data and Nuclear Data Tables*, 2001, 78 (2), 183–356.
- Heiskanen, W. A. and H. Moritz, *Physical Geodesy*, Springer-Verlag, 1967.
- Honda, M., T. Kajita, K. Kasahara, and S. Midorikawa, “Improvement of low energy atmospheric neutrino flux calculation using the JAM nuclear interaction model,” *Phys. Rev. D*, Jun 2011, 83, 123001.
- Jourde, K., D. Gibert, J. Marteau, J. de Bremond d’Ars, S. Gardien, C. Girerd, J.-C. Ianigro, and D. Carbone, “Experimental detection of upward going cosmic particles and consequences for correction of density radiography of volcanoes,” *Geophys. Res. Lett.*, 2013, 40 (24), 6334–6339.
- Lees, J. M. and J. C. VanDecar, “Seismic tomography constrained by bouguer gravity anomalies: Applications in western Washington,” *PAGEOPH*, 1991, 135 (1), 31–52.
- Lesparre, N., D. Gibert, J. Marteau, J. Komorowski, F. Nicollin, and O. Coutant, “Density muon radiography of La Soufriere of Guadeloupe volcano: comparison with geological, electrical resistivity and gravity data,” *Geophys. J. Int.*, 2012, 190 (2), 1008–1019.
- , —, —, Y. Déclais, D. Carbone, and E. Galichet, “Geophysical muon imaging: feasibility and limits,” *Geophys. J. Int.*, 2010, 183 (3), 1348–1361.
- Lipari, Paolo, “The east-west effect for atmospheric neutrinos,” *Astroparticle Physics*, 2000, 14 (3), 171 – 188.
- Mimatsu, M., *Diary of the Growth of Showa-Shinzan*, Mimatsu Masao Memorial Museum, 1962.
- Minakami, T., T. Ishikawa, and K. Yagi, “The 1944 Eruption of Volcano Usu in Hokkaido, Japan,” *Bulletin Volcanologique*, 1951, 11 (1), 45–157.
- Minato, S., “Bulk density estimates of buildings using cosmic rays,” *International Journal of Radiation Applications and Instrumentation. Part A. Applied Radiation and Isotopes*, 1986, 37 (9), 941 – 946.
- Miyauchi, H., H. Watanabe, T. Maekawa, A. Suzuki, H. Mori, and H. Okada, “Seismic observation on Showa-Shinzan using ground-fireworks,” *Geophys. Bull. Hokkaido Univ.*, 1987, 49, 75–83.
- Morishima, K., A. Nishio, Y. Kato, T. Nakano, and M. Nakamura, “Development of Nuclear Emulsion Detector for Cosmic-ray Muon Radiography and Its Applications,” in “Japan Geoscience Union Meeting 2014” 2014.
- and T. Nakano, “Development of a new automatic nuclear emulsion scanning system, S-UTS, with continuous 3D tomographic image read-out,” *JINST*, 2010, 5 (04), P04011.
- Morris, C. L., J. Bacon, Y. Ban, K. Borozdin, J. M. Fabritius, M. Izumi, H. Miyadera, S. Mizokami, Y. Otsuka, J. Perry, J. Ramsey, Y. Sano, T. Sugita, D. Yamada, N. Yoshida, and K. Yoshioka, “Analysis of muon radiography of the Toshiba nuclear critical assembly reactor,” *Appl. Phys. Lett.*, 2014, 104 (2), 024110.

- Nagamine, K., H. K. M. Tanaka, S. N. Nakamura, K. Ishida, M. Hashimoto, Shinotake A., M. Naito, and A. Hatanaka, "Probing the inner structure of blast furnaces by cosmic-ray muon radiography," *P. Jpn. Acad., Ser. B*, 2005, 81 (7), 257–260.
- , M. Iwasaki, K. Shimomura, and K. Ishida, "Method of probing inner-structure of geophysical substance with the horizontal cosmic-ray muons and possible application to volcanic eruption prediction," *Nucl. Instrum. Meth. A*, 1995, 356 (2??), 585–595.
- Nagy, D., "The prism method for terrain corrections using digital computers," *PA-GEOPH*, 1966, 63 (1), 31–39.
- Nakamura, S. and T. Mori, "On the mechanism of the formation of the Showa New Mountain of Usu volcano," *Sci. Rep., Tohoku Univ. Ser. 5*, 1949, 1, 45–49.
- Nakamura, T., PhD dissertation, Nagoya University 2005.
- , A. Ariga, T. Ban, T. Fukuda, T. Fukuda, T. Fujioka, T. Furukawa, K. Hamada, H. Hayashi, S. Hiramatsu et al., "The OPERA film: New nuclear emulsion for large-scale, high-precision experiments," *Nucl. Instrum. Meth. A*, 2006, 556 (1), 80–86.
- Nemoto, T., M. Hayakawa, K. Takahashi, and S. Oana, "Report on geological, geophysical and geochemical studies of Usu volcano (Showa-Shinzan)," *Rep. Geol. Surv. Jpn.*, 1957, 170, 1–149.
- Niita, K., T. Sato, H. Iwase, H. Nose, H. Nakashima, and L. Sihver, "PHITS: a particle and heavy ion transport code system," *Radiat. Meas.*, 2006, 41 (9??0), 1080–1090. Space Radiation Transport, Shielding, and Risk Assessment Models.
- Nishida, Y. and E. Miyajima, "Subsurface structure of Usu volcano, Japan as revealed by detailed magnetic survey," *J. Volcanol. Geoth. Res.*, 1984, 22 (3??), 271 – 285.
- Nishimura, J., M. Fujii, T. Kobayashi, H. Aizu, Y. Komori, and M. Kazuno, "Emulsion Chamber Observations of Primary Electrons," *Proceedings of the 21st International Cosmic Ray Conference*, 1980, 3, 213–216.
- Nishiyama, R., S. Miyamoto, and N. Naganawa, "Experimental study of source of background noise in muon radiography using emulsion film detectors," *Geosci. Instrum. Method. Data Syst.*, 2014, 3 (1), 29–39.
- , Y. Tanaka, S. Okubo, H. Oshima, H. K. M. Tanaka, and T. Maekawa, "Integrated processing of muon radiography and gravity anomaly data toward the realization of high-resolution 3-D density structural analysis of volcanoes: Case study of Showa-Shinzan lava dome, Usu, Japan," *J. Geophys. Res.,: Solid Earth*, 2014, 119 (1), 699–710.
- Niu, K., E. Mikumo, and Y. Maeda, "A Possible Decay in Flight of a New Type Particle," *Prog. Theor. Phys.*, 1971, 46, 1644–1646.
- Okubo, S. and H. K. M. Tanaka, "Imaging the density profile of a volcano interior with cosmic-ray muon radiography combined with classical gravimetry," *Meas. Sci. Technol.*, 2012, 23 (4), 042001.
- Ostapchenko, S., "QGSJET-II: towards reliable description of very high energy hadronic interactions," *Nuclear Physics B - Proceedings Supplements*, 2006, 151 (1), 143 – 146.

- Roesler, S., R. Engel, and J. Ranft, “The event generator DPMJET-III at cosmic ray energies.,” in “Proceedings of 27th ICRC” 2001.
- Roh, S., J. Kim, D. Ryu, H. Kang, K. Kasahara, E. Kido, and A. Taketa, “A comparison study of CORSIKA and COSMOS simulations for extensive air showers,” *Astropart. Phys.*, 2013, 44 (0), 1 – 8.
- Rokujo, H., S. Aoki, S. Takahashi, K. Kamada, S. Mizutani, R. Nakagawa, and K. Ozaki, “Multi-stage shifter for subsecond time resolution of emulsion gamma-ray telescopes,” *Nuclear Instruments and Methods in Physics Research Section A: Accelerators, Spectrometers, Detectors and Associated Equipment*, 2013, 701 (0), 127 – 132.
- Sanuki, T., M. Motoki, H. Matsumoto, E. S. Seo, J. Z. Wang, K. Abe, K. Anraku, Y. Asaoka, M. Fujikawa, M. Imori, T. Maeno, Y. Makida, N. Matsui, H. Matsunaga, J. Mitchell, T. Mitsui, A. Moiseev, J. Nishimura, M. Nozaki, S. Orito, J. Ormes, T. Saeki, M. Sasaki, Y. Shikaze, T. Sonoda, R. Streitmatter, J. Suzuki, K. Tanaka, I. Ueda, N. Yajima, T. Yamagami, A. Yamamoto, T. Yoshida, and K. Yoshimura, “Precise Measurement of Cosmic-Ray Proton and Helium Spectra with the BESS Spectrometer,” *The Astrophysical Journal*, 2000, 545 (2), 1135.
- Snyder, D. B. and W. J. Carr, “Interpretation of gravity data in a complex volcanotectonic setting, southwestern Nevada,” *J. Geophys. Res.: Solid Earth*, 1984, 89 (B12), 10193–10206.
- Sugita, T., J. Bacon, Y. Ban, K. Borozdin, M. Izumi, Y. Karino, N. Kume, H. Miyadera, S. Mizokami, C. L. Morris, K. Nakayama, Y. Otsuka, J. O. Perry, J. Ramsey, Y. Sano, D. Yamada, N. Yoshida, and K. Yoshioka, “Cosmic-ray muon radiography of UO₂ fuel assembly,” *J. Nucl. Sci. Technol.*, 2014, 51 (7-8), 1024–1031.
- Tanaka, H. K. M., H. Miyajima, T. Kusagaya, A. Taketa, T. Uchida, and M. Tanaka, “Cosmic muon imaging of hidden seismic fault zones: Rainwater permeation into the mechanical fractured zones in Itoigawa–Shizuoka Tectonic Line, Japan,” *Earth Planet. Sc. Lett.*, 2011, 306 (3), 156–162.
- , H. Taira, T. Uchida, M. Tanaka, M. Takeo, T. Ohminato, Y. Aoki, R. Nishiyama, D. Shoji, and H. Tsuiji, “Three-dimensional computational axial tomography scan of a volcano with cosmic ray muon radiography,” *J. Geophys. Res.: Solid Earth*, 2010, 115 (B12), B12332.
- , K. Nagamine, S. N. Nakamura, and K. Ishida, “Radiographic measurements of the internal structure of Mt. West Iwate with near-horizontal cosmic-ray muons and future developments,” *Nucl. Instrum. Meth. A*, 2005, 555 (1??), 164 – 172.
- , T. Kusagaya, and H. Shinohara, “Radiographic visualization of magma dynamics in an erupting volcano,” *Nat. Commun.*, 2014, 5.
- , T. Nakano, S. Takahashi, J. Yoshida, and K. Niwa, “Development of an emulsion imaging system for cosmic-ray muon radiography to explore the internal structure of a volcano, Mt. Asama,” *Nucl. Instrum. Meth. A*, 2007, 575 (3), 489–497.
- , —, —, —, H. Ohshima, T. Maekawa, H. Watanabe, and K. Niwa, “Imaging the conduit size of the dome with cosmic-ray muons: The structure beneath Showa-Shinzan Lava Dome, Japan,” *Geophys. Res. Lett.*, 2007, 34, L22311.

- , **T. Uchida, M. Tanaka, H. Shinohara, and H. Taira**, “Cosmic-ray muon imaging of magma in a conduit: Degassing process of Satsuma-Iwojima Volcano, Japan,” *Geophys. Res. Lett.*, 2009, *36* (1), L01304.
- Tanaka, H., K. Nagamine, N. Kawamura, S. N. Nakamura, K. Ishida, and K. Shimomura**, “Development of a two-fold segmented detection system for near horizontally cosmic-ray muons to probe the internal structure of a volcano,” *Nucl. Instrum. Meth. A*, 2003, *507* (3), 657 – 669.
- Tarantola, A. and A. Necessian**, “Three-dimensional inversion without blocks,” *Geophys. J. R. Astron. Soc.*, 1984, *76*, 299–306.
- and **B. Valette**, “Inverse Problems = Quest for information,” *J. Geophys.*, 1982, *50*, 159–170.
- Tioukov, V., I. Kreslo, Y. Petukhov, and G. Sirri**, “The FEDRA: framework for emulsion data reconstruction and analysis in the OPERA experiment,” *Nucl. Instrum. Meth. A*, 2006, *559* (1), 103–105.
- Toshito, T., A. Ariga, T. Ban, K. Hoshino, M. Komatsu, N. Naganawa, M. Nakamura, T. Nakamura, T. Nakano, and K. Niwa**, “ π/p separation at 1.2 GeV/c by an emulsion cloud chamber,” *Nucl. Instrum. Meth. A*, 2004, *516* (2), 436–439.
- Yoshimoto, M., T. Nakano, and R. Komatani**, “Nuclear Emulsion Readout System, HTS,” in “26th International Conference on Nuclear Tracks in Solids” 2014.
- Zidarov, D.**, *Inverse Gravimetric Problem in Geoprospecting and Geodesy*, Elsevier, New York, 1990.